B. M. Weckhuysen

DOI: 10.1002/anie.200900339

Heterogeneous Catalysts

Chemical Imaging of Spatial Heterogeneities in Catalytic Solids at Different Length and Time Scales

*Bert M. Weckhuysen**

Keywords:
heterogeneous catalysis · in situ spectroscopy · nanoparticles · single-molecule spectroscopy · zeolites

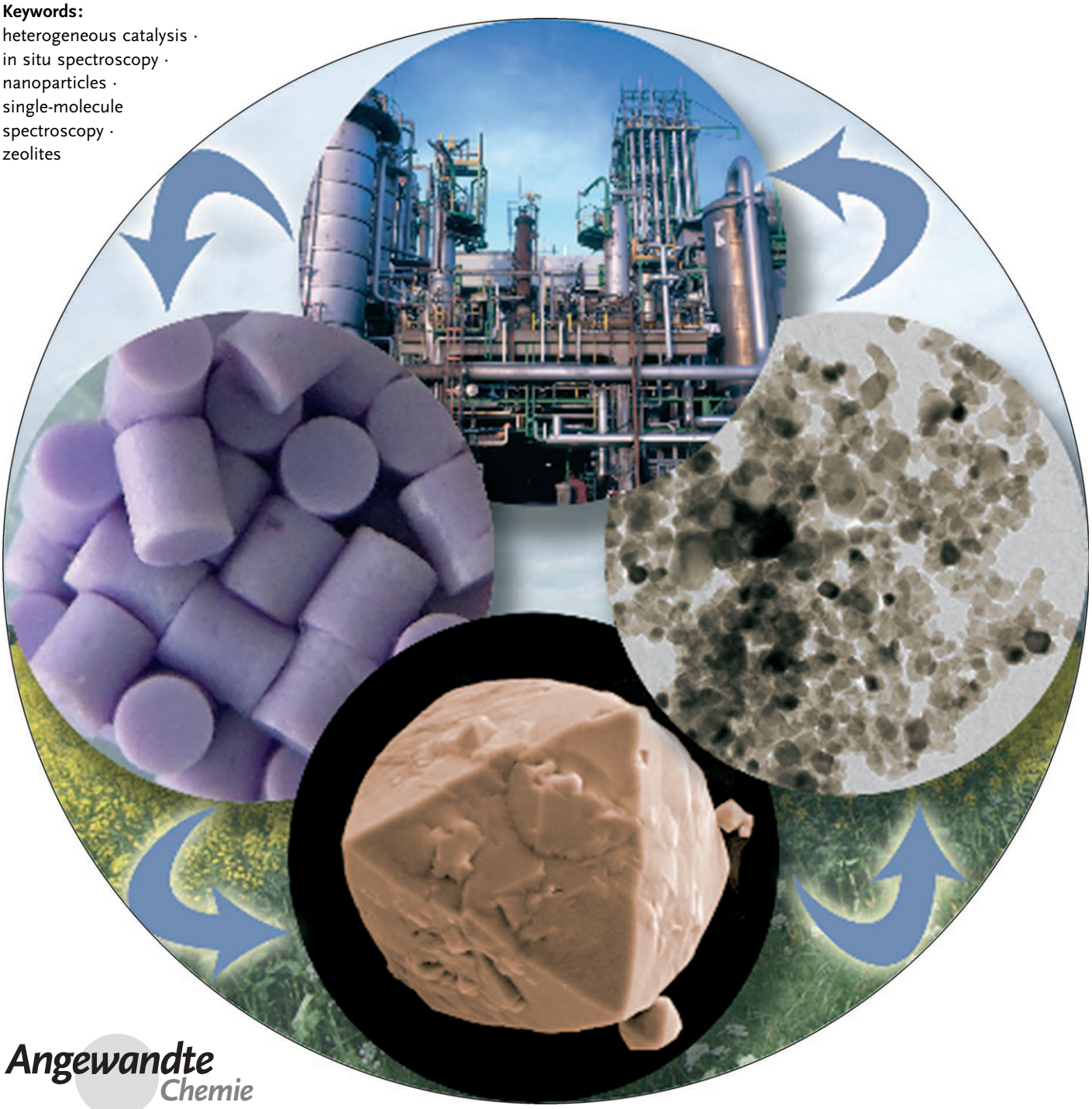

Knowledge of spatiotemporal gradients in heterogeneous catalysts is of paramount importance for the rational design of new and more sustainable catalytic processes. Heterogeneities resulting in space- and time-dependent phenomena occur at different length scales; that is, at the level of catalytic reactors (mm to m), catalyst bodies (μm to mm), catalyst grains (nm to μm), and active sites and metal (oxide) particles (Å to nm). This Review documents the recent advances in the development of space- and time-resolved spectroscopic methods for imaging spatial heterogeneities within catalytic processes at these four length scales. Particular emphasis will be on the use of magnetic resonance, optical, and synchrotron-based methods, their capabilities in providing spatial resolution (1D and 2D imaging) and depth profiling (3D imaging) as well as on their time-resolved application, potential for single-molecule and nanoparticle detection, and use under reaction conditions. The Review ends with future prospects on spectroscopic markers for catalytic activity, label-free spectroscopy, tomography at the nanoscale, and correlative microscopic approaches.

From the Contents

1. Introduction 4911
1.1. Spatial Heterogeneities in Catalytic Solids 4911
1.2. Scope 4913

2. Imaging Spatial Heterogeneities of Catalytic Solids at Different Length and Time Scales with Electromagnetic Radiation 4913
2.1. Spatial Heterogeneities at the Level of a Catalytic Reactor 4914
2.2. Spatial Heterogeneities at the Level of Millimeter-Sized Catalyst Bodies 4921
2.3. Spatial Heterogeneities at the Level of Micrometer-Sized Zeolite Crystals 4925
2.4. Spatial Heterogeneities at the Level of Catalyst Nanoparticles and Single Molecules 4932

3. Future Prospects 4937
3.1. Microscopy of Labeled Samples and Label-Free Microscopy 4937
3.2. Towards In Situ Optical Tomography at the Nanoscale 4938
3.3. Development of Correlative Microscopy Approaches 4939

1. Introduction

1.1. Spatial Heterogeneities in Catalytic Solids

Heterogeneous catalysts are the workhorses of chemical industry, and more than 80% of all chemicals have come into contact with at least one catalyst material during their manufacturing process.[1–6] Catalytic solids are very complex, as they possess many different potential active sites in their porous structures.[7] Determining the nature of these active sites and elucidating their reaction mechanisms are important intellectual challenges that are of paramount importance for the rational design of heterogeneous catalysts. Success in these endeavors offers the rewarding prospect of improved formulations of existing catalytic solids and the possibility to create more effective and selective catalysts from scratch.

Until recently, most characterization studies of catalytic solids focused on ensemble-averaged measurements, assuming that heterogeneous catalysts are spatially homogeneous objects when placed in a catalytic reactor. Point measurements (0D scans) of catalytic solids are then usually taken as a function of reaction time to study activation and deactivation phenomena. Such measurements allow the development of structure–performance relationships by relating different physicochemical properties to each other, such as activity, selectivity, porosity, adsorption, degree of reduction, and a multitude of spectroscopic signatures.[8–11] However, these macroscopically determined properties are not necessarily identical across the entire reactor bed or within a catalyst grain. Spatiotemporal phenomena are more the rule than the exception for heterogeneous catalysts, as the local environment strongly affects the above-mentioned macroscopic properties. All this leads to spatial heterogeneities or reaction fronts, which remain unnoticed when point measurements are performed.

An archetypal example of spatiotemporal variations in heterogeneous catalysis is the catalytic oxidation of CO with O_2 over platinum model catalysts as investigated by Ertl and co-workers.[12] Figure 1 shows a 2D photoemission electron microscopy (PEEM) image of the formation of spiral waves in catalytic CO oxidation on a Pt(110) surface. Dark areas are essentially oxygen-covered, while the lighter patches are CO-covered. The spiral waves develop and propagate with front speeds of a few micrometers per second, and the cores of the spirals are often formed at a region on the Pt surface with enhanced defect density. This effect is also responsible for the fact that the wavelengths of the spiral waves vary to some degree. As the reaction mechanism of CO oxidation is known in great detail and all its parameters of influence have been determined, it has been possible to simulate the process of spiral wave development, which nicely matches the experimental findings.

[*] Prof. Dr. B. M. Weckhuysen
Inorganic Chemistry and Catalysis group
Debye Institute for Nanomaterials Science, Utrecht University
Sorbonnelaan 16, 3584 CA Utrecht (The Netherlands)
E-mail: b.m.weckhuysen@uu.nl

Supporting information for this article is available on the WWW under http://dx.doi.org/10.1002/anie.200900339.

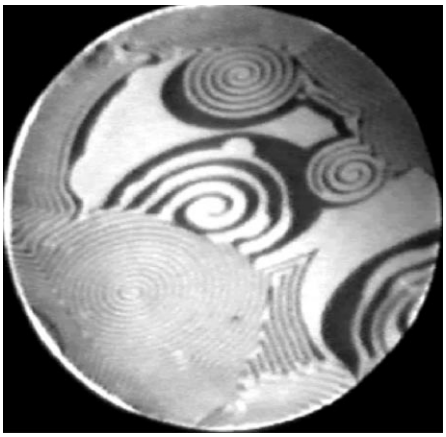

Figure 1. 2D Photoemission electron microscopy (PEEM) image from a Pt(110) surface during catalytic CO oxidation ($p_{CO} = 4.3 \times 10^{-4}$, $p_{O_2} = 4 \times 10^{-5}$ mbar, $T = 175\,°C$). The diameter of the picture is 500 μm. Reproduced from reference [12].

Spatiotemporal effects are, however, not limited to model surface-science studies, but are generally expected for open systems far from equilibrium, as is the case for all heterogeneous catalytic processes. In realistic heterogeneous catalytic systems they occur at four different length scales, as schematically illustrated in Figure 2. To better visualize these different length scales, Movie S1 is available as Supporting Information, showing how a propane molecule travels through an industrial dehydrogenation plant until it is finally converted into propene and hydrogen.[13] The first level of interest is the reactor, in which a suitable catalyst material is carefully packed. A catalytic reactor is usually on the order of centimeters to meters in length if a full-scale commercial installation is considered. The catalyst performance, however, is not the same over the entire catalyst-bed volume. When considering a fixed-bed reactor, as is the case for the propane dehydrogenation plant, spatiotemporal gradients in the concentrations of propane, propene, hydrogen, and by-products (e.g. ethane and methane) are observed. In other words, the concentrations of these molecules vary along both the axial and radial directions of the catalyst bed as a function of reaction time. Moreover, temperature gradients may also arise from the endothermicity of the dehydrogenation process. As a result, catalyst reduction and deactivation phenomena may be quite different along the catalyst bed, significantly affecting catalyst regeneration procedures.

To avoid pressure drops in gas-phase reactors, catalyst bodies of millimeter dimensions are used. They often have particular shapes, and reactant molecules must penetrate through these catalyst bodies to be converted. In some cases, the catalytically active phase has been specifically positioned on the outer layers of the catalyst body, leading to a particular spatial distribution of the active phase (i.e. an egg-shell distribution). The third level at which spatial heterogeneities may occur constitutes, for example, porous catalyst crystals or grains of micrometer or sub-micrometer dimensions. Diffu-

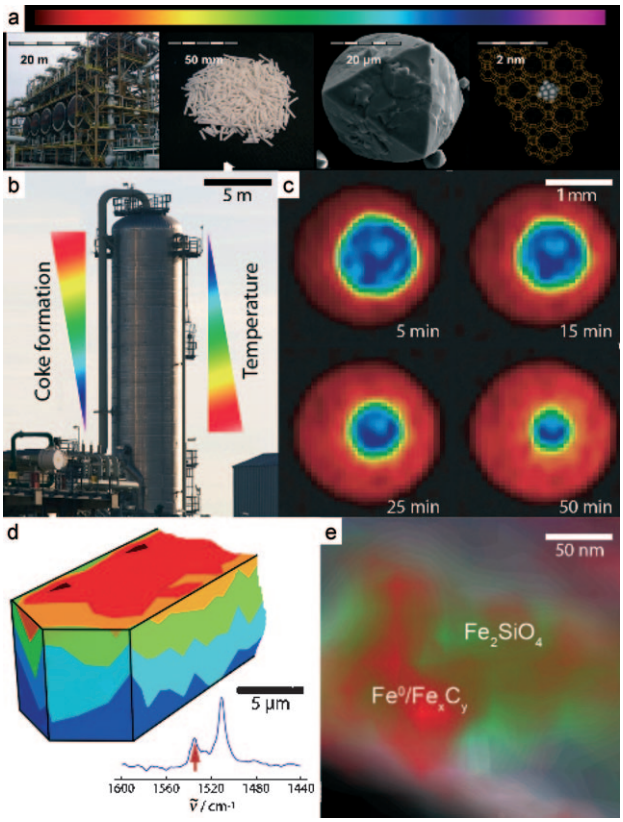

Figure 2. Selected examples of spatial heterogeneities occurring in heterogeneous catalysis at different length scales: a) Selected frames from Movie S1 in the Supporting Information showing how a propane molecule travels through an industrial dehydrogenation plant until it is finally converted into propene and hydrogen. b) Coke and temperature profiles over an industrial reactor spanning several meters. c) Spatial gradients of the amount of transition-metal ion across an individual Al_2O_3 catalyst body spanning several millimeters. d) Spatial gradients of a reaction product across an individual zeolite crystal spanning several micrometers. e) Spatial gradients of metal, metal oxide, and metal carbide within an individual catalyst grain spanning several nanometers.

Bert Weckhuysen, born in 1968 in Aarschot, Belgium, received his master degree from Leuven University (Belgium) in 1991. After finishing his PhD studies under the supervision of Prof. Schoonheydt in 1995, he worked as a postdoctoral fellow with Prof. Wachs at Lehigh University (USA) and with Prof. Lunsford at Texas A&M University (USA). From 1995 until 2000 he was a research fellow of the Belgian National Science Foundation. Since 2000, Weckhuysen has been full professor inorganic chemistry and catalysis at Utrecht University. He received several research awards, including the 2002 VICI award from the Netherlands Organization for Scientific Research (NWO), the 2006 Gold Medal from the Royal Netherlands Society of Chemistry (KNCV), the 2007 DECHEMA Award from The Max Buchner Research Foundation (Germany), and the 2009 Netherlands Catalysis and Chemistry Award from the KNCV Catalysis Section and the Netherlands Organization of Catalysis Industries. He is scientific director of the Dutch Research School for Catalysis (NIOK) and an elected member of the Young Academy of the Royal Dutch Academy of Sciences (KNAW), the Netherlands Academy of Technology and Innovation (NATI), and the Royal Holland Society of Sciences (KHMW).

sion of reactants and reaction products within these porous networks, which contain a wide distribution of macro-, meso-, and micropores, will strongly influence the overall performance of a catalytic process. Short- and long-range cracks, transport barriers, and dead ends in the pore structure may lead to different diffusion pathways and related concentration gradients, directly influencing catalyst performance and even making some areas of the catalyst grain completely inaccessible for catalytic action. In other words, catalyst bodies and grains may be inefficiently used when transport phenomena become rate-limiting.

Finally, the catalyst grains contain active sites with dimensions of nanometers or Ångströms. This is the fourth important length scale at which spatial heterogeneities may occur. Although the active site can be spatially isolated, such as for Brønsted acid groups in zeolites, in most cases the activity of this site is still distinct from another site spatially positioned only a little further in the catalyst grain. This phenomenon can be due to local changes in chemical composition or to different reactant accessibility induced by shape-selectivity effects. Furthermore, the number of active sites can differ from surface to surface. In the case of supported metal nanoparticles, for example, the reactivity and selectivity can be tailored by controlling the shape, as shape determines the number of atoms located at the edges and corners.[14] In general, high-index planes have a greater density of unsaturated atomic steps, edges, and kinks, which can serve as active sites for the breaking and making of chemical bonds.[15] Furthermore, these supported metal nanoparticles may coexist in a wide variety of sizes and shapes, each possessing its own catalytic activity. The same heterogeneity may result when an alloying element is introduced to the metal nanoparticle, as the alloy can be uniform or have, for example, an egg-shell distribution.

1.2. Scope

It is no wonder that the complexity described above complicates the development of useful structure–performance relationships in the field of heterogeneous catalysis, as the measured macroscopic properties, such as activity and selectivity, are the result of a complex interplay between different physicochemical gradients across the four important length scales. Therefore, mastering the overall performance of a catalytic process in terms of activity, selectivity, and stability requires full control of the spatiotemporal phenomena taking place from the meter scale down to the level of a few nanometers or even smaller. Evidently, this is an enormous task, but fortunately both academic and industrial researchers have built up a lot of (often empirical) knowledge and technical skill to tackle the related challenges to construct robust and efficient catalytic processes.

This Review will show the tremendous progress we have seen in the last decade in the field of spectroscopy for imaging spatial heterogeneities in catalytic solids, preferably applied under in situ conditions, leading to new physicochemical insights at the four length scales of importance in heterogeneous catalysis. This will be done by highlighting space- and time-resolved spectroscopy research on molecular transport, catalyst preparation, and reactivity and deactivation phenomena. Special emphasis will be placed on combining microscopy and spectroscopy, including 1D (x scanning), 2D (x-y scanning), 3D (x-y-z scanning or tomography), and 4D (time-resolved x-y-z scanning) imaging, as well as by discussing recent studies on the emerging fields of single-molecule and single-nanoparticle detection. The Review will end with an outlook on expected future developments in this exciting field of research.

2. Imaging Spatial Heterogeneities of Catalytic Solids at Different Length and Time Scales with Electromagnetic Radiation

Three criteria are important for proper chemical imaging of heterogeneous catalysts: spatial resolution, time resolution, and chemical information density. Each characterization technique has its own advantages and disadvantages regarding these criteria. Table 1 gives an overview of the different characterization methods based on electromagnetic radiation available for the imaging of catalytic solids. Techniques that have already been applied in the field of heterogeneous catalysis are written in italics. The methods span the whole spectrum of electromagnetic radiation, from radio- (NMR microscopy) and microwaves (EPR microscopy) through infrared light (IR microscopy), visible and ultraviolet light (UV/Vis microscopy and different forms of Raman and fluorescent microscopy), to X-rays (e.g. STXM (scanning transmission X-ray microscopy) and TEDDI (tomographic energy-dispersive diffraction imaging)). A distinction must be made between far-field (FF) methods, which make use of a lens positioned at least a wavelength away from the object of interest, and near-field (NF) methods. Examples of the latter are scanning near-field infrared microscopy (SNIM) and scanning near-field optical microscopy (SNOM), which overcome the diffraction limits of light. All techniques rely on the absorption, scattering, fluorescence, or diffraction of light, and their abbreviations are explained in the footnotes of Table 1. To give an impression of their strengths for chemical imaging, Table 1 also includes the currently achieved spatial resolution in the x, y, and z directions. However, spatial resolution in microscopy is almost always limited by sensitivity, and the ultimate resolutions reported have often been obtained for unique samples that give very large signal-to-noise (S/N) ratios. In other words, for most routine samples the practical spatial resolution is somewhat lower than indicated in Table 1.

Illustrative examples on the use of space- and time-resolved in situ spectroscopy are highlighted below. These case studies will cover reactions catalyzed by acids and bases as well as by redox, electrochemical, and photochemical processes involving heterogeneous catalysts applied in the gas or liquid phase. Note that this Review is not meant to be exhaustive but merely intends to give a general overview of the exciting developments we have seen especially in the last five years. Furthermore, different high-throughput screening techniques, which often use space-resolved methods, will not

Table 1: Overview of the different characterization methods based on electromagnetic radiation available for the imaging of catalytic solids; those indicated in italics have already been used in the field.

Light source	X-rays		UV/Vis[b]		Infrared light	Microwaves	Radiowaves
Methods	*X-ray microscopy*	*Raman microscopy*	*Fluorescence microscopy*	*UV/Vis microscopy*	*IR microscopy*	*ESR microscopy*	*NMR microscopy*
currently reported far-field lateral resolution	15 nm	500 nm–3 μm	200–300 nm	1–3 μm	3–5 μm	3 μm	3 μm
extension to the nanoscale possible	yes, e.g. *STXM*[a]	not yet reported	yes, e.g. STED,[d] FPALM,[e] STORM[f]	not yet reported	not yet reported	under development	not yet reported[i]
currently reported near-field lateral resolution and related technique	under development	TERS[c] (15 nm)	SNOM[g] (30 nm)	not yet reported	SNIM[h] (30 nm)		
potential for 3D imaging and axial resolution	yes, 10 nm	*confocal Raman* (500 nm)	*confocal fluorescence spectroscopy* (500 nm); STED (20 nm) STORM (30 nm)	not yet reported	yes	yes, 3 μm	yes, 3 μm

[a] Scanning transmission X-ray microscopy. [b] A promising method to circumvent the resolution barrier of conventional diffraction is to make use of superlenses, which may bring the spatial resolution towards 10 nm; see reference [110]. [c] Tip-enhanced Raman spectroscopy. [d] Stimulated emission depletion microscopy. [e] Fluorescence photoactivated localization microscopy. [f] Stochastic optical reconstruction microscopy. [g] Scanning near-field optical microscopy. [h] Scanning near-field infrared microscopy. [i] After submission of this manuscript, a report appeared revealing the use of magnetic resonance imaging (MRI) with a resolution of less than 10 nm on a Tobacco Mosaic virus particle; see reference [111].

be covered; reference is made to articles based on IR and fluorescence microscopy.[16]

2.1. Spatial Heterogeneities at the Level of a Catalytic Reactor

2.1.1. Visualizing the Spatial Variation of Esterification, Etherification, and Hydrogenation Reactions within Fixed- and Trickle-Bed Reactors with Magnetic Resonance Imaging

Yuen et al. studied the spatial variation of a chemical conversion process within a fixed-bed reactor making use of in situ MRI.[17] To this end, they studied the liquid-phase esterification reaction of methanol and acetic acid as catalyzed by an Amberlyst ion-exchange resin. This liquid-phase reaction can be monitored in a reactor by following the ^{1}H chemical shift of the hydroxy resonance associated with the fluid in the interparticle space of the catalytic bed. In this manner, it is possible to measure the extent of reaction non-invasively. Figure 3a shows a 2D slice through a ^{1}H 3D MRI image of the fixed-bed catalyst particles (black). Three slice sections 4.5 mm apart were selected, and volume-selective ^{1}H NMR spectra were recorded and evaluated for each of these slices. When the experiment was performed under flowing conditions, distinct spatial variations occurred within these three slice sections. These variations are evidenced by the volume-selective spectroscopy results shown in Figure 3b for slice III, in which ten volumes were selected and investigated. It can be seen in Figure 3c that the peak at around 7 ppm in the NMR spectrum, which arises from the ^{1}H resonance associated with the OH group of the liquid in the interparticle space, displays different chemical shifts. This finding implies significant variation in the extent of catalytic conversion within slice III. More specifically, the fractional variation in the conversion levels reached a value of 22%. The authors applied the same approach for slices I and II in the catalytic reactor, leading to the results summarized in Figure 3d–f. It was found that the conversion increases in the direction of the reactant flow, as expected, but that significant heterogeneity in conversion exists within each transverse section through the catalyst bed.

Koptyug et al. employed magnetic resonance spectroscopic imaging to study the behavior of a gas–liquid–solid model catalytic reactor operating at elevated temperatures with Pd/Al_2O_3 as catalyst material and the hydrogenation of α-methylstyrene (AMS) to cumene as probe reaction.[18] The experimental setup for these MRI experiments is illustrated in Figure 4a. The model reactor, which can be placed directly inside the MRI probe, consists of a system to supply H_2 and liquid AMS. The research group performed a 3D MRI experiment with two spatial and one spectral coordinate. Such an experiment yields a 2D map of the liquid distribution within an axial slice through the bed, with an NMR spectrum for each image pixel acquired in the same experimental run. A 2D subset of the entire 3D dataset is shown in Figure 4b. It has one spatial (vertical) and one spectral coordinate (horizontal). The integral projection of this dataset on the vertical axis (Figure 4c) reflects the distribution of the liquid phase along the axial bar shown in Figure 4b, while any horizontal cross-section is an NMR spectrum of the liquid at the corresponding location within that bar (e.g. Figure 4d–f). For reference, the ^{1}H NMR spectra of pure liquid AMS and cumene are included in Figure 4g,h. Despite substantial line broadening in the spectra of liquids permeating porous solids, the two spectra are still distinctly different. The essential features are 1) the presence of the broad peak at about 5.2 ppm in Figure 4g and its absence in Figure 4h, 2) the different separation of the outermost peaks in the spectra, and 3) the inverted ratio of their relative intensities. These spectral differences can clearly be observed in Figure 4d–f, thus indicating that AMS predominates in the upper part of the catalytic reactor; almost pure cumene is present near the

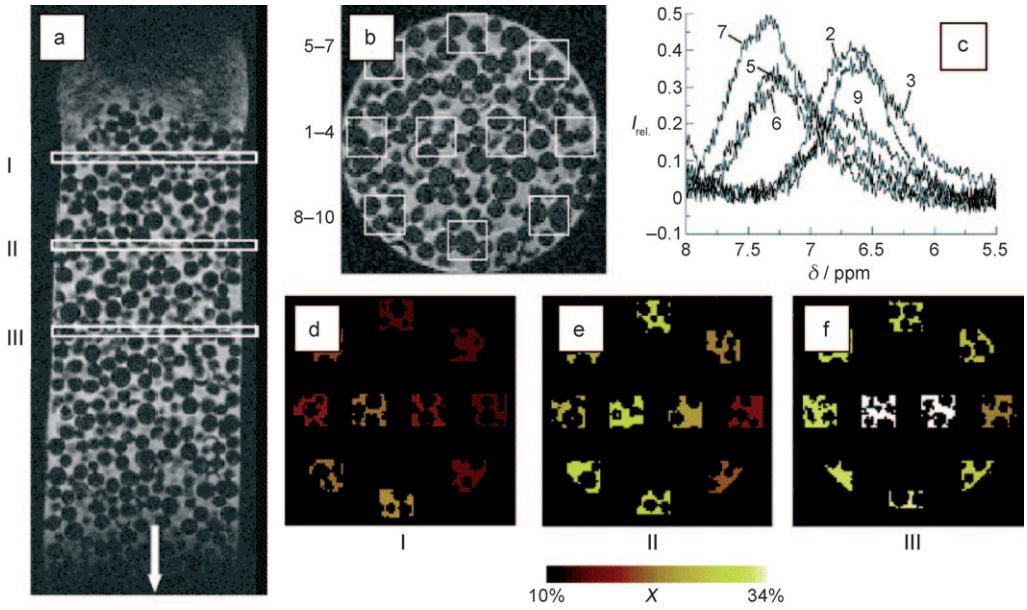

Figure 3. Illustration of the use of in situ MRI to observe in a fixed-bed reactor spatial gradients of the liquid-phase esterification reaction of methanol and acetic acid over an Amberlyst-15 ion-exchange resin: a) A 2D slice through a ^{1}H 3D RARE MRI image (RARE = rapid acquisition relaxation enhanced) of the fixed-bed reactor filled with catalyst particles, which appear black. Three slice sections for which volume-selective ^{1}H NMR spectra were recorded are indicated along with the direction of the flow of reactants. b) The location of 10 selected volumes within slice III. c) The volume-selective ^{1}H NMR spectra for the different selected volumes in (b). d–f) Measurement of catalytic conversion within slices I, II, and III through the same bed. Reproduced from reference [17], copyright Elsevier Science B.V., 2002.

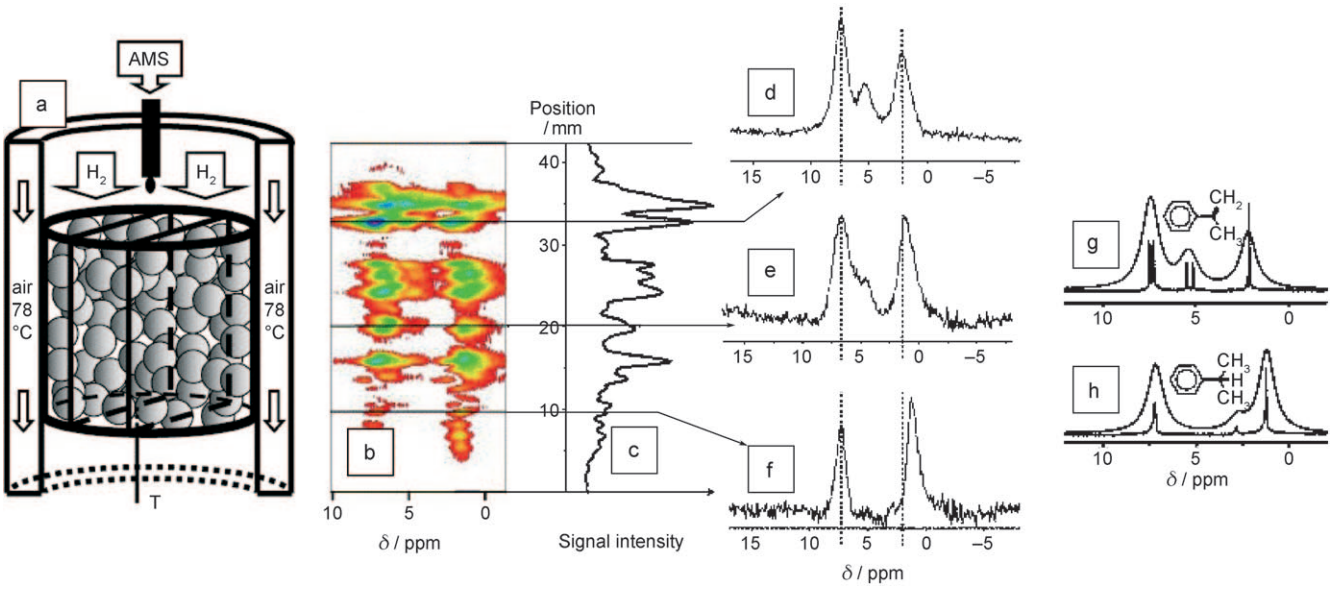

Figure 4. a) Schematic representation of the fixed-bed reactor for measuring in situ MRI for the hydrogenation of α-methylstyrene (AMS) to cumene over a Pd/Al_2O_3 catalyst. The catalyst material is placed in a glass cell. Liquid reactant (AMS) is supplied through a capillary to the top of the reactor, while a stream of hydrogen is supplied to the reactor and the temperature of the reactor volume is controlled by passing warm air through the double-walled glass cylinder surrounding the reaction volume. A thermocouple (T) is implanted into the lower part of the reactor through the supporting mesh. b) A mixed spatial–spectral ^{1}H 2D MRI map, which corresponds to the axial bar marked in (a). c) The distribution of the liquid phase along the axial bar obtained as an integral projection of (b) on its vertical axis. d–f) ^{1}H NMR spectra of the liquid phase at different heights along the bar obtained as horizontal cross-sections of the map in (b). The location of these cross-sections are indicated by the horizontal lines in (b) and (c). The two vertical dotted lines are drawn to show the differences in the relative positions of the outermost peaks in the spectra. g,h) ^{1}H NMR spectra of AMS and cumene, respectively, obtained experimentally in solution (lower traces); the upper traces are obtained by numerically broadening the individual NMR lines in the solution spectra from a few Hz to 300 Hz to simulate the influence of the porous matrix on the spectral line width. Reproduced from reference [18], copyright Elsevier Science B.V., 2004.

outlet of the catalytic reactor, while a mixture of the two liquids is observed in the middle. In other words, an increase of the product/reactant ratio from top to bottom of the catalytic reactor could be observed by MRI.

Two approaches are typically used when studying hydrocarbon reactions with in situ MRI: either the ^{1}H or the ^{13}C nucleus can be monitored. As illustrated by the two examples above, whenever possible the observation of the ^{1}H nucleus is the method of choice owing to its 99.9% natural abundance and the related high MRI sensitivity. However, the disadvantage of ^{1}H MRI is that the ^{1}H nucleus has a relatively narrow chemical-shift range. Furthermore, there is 1) a large number of ^{1}H resonances present in a typical spectrum and 2) broadening of these resonances as a result of decreased spin–spin relaxation times arising from the large solid–liquid interface within a given sample. These detractors make the spectral assignment and the quantification of peak areas rather difficult, leading to complications in the use of ^{1}H MRI for studying catalytic reactions. For observation of the ^{13}C nucleus, spectral assignment is easier, because ^{13}C has a much wider chemical-shift range than ^{1}H, thereby reducing the number of overlapping peaks. Unfortunately, the natural abundance of ^{13}C is only 1.07%, and its MRI sensitivity is much lower than that of ^{1}H. Molecules of interest could be enriched with ^{13}C, but such methods are very expensive for in situ MRI experiments under flow conditions.

To circumvent this problem, Akpa et al. developed an MRI method based on the natural abundance of ^{13}C, referred as ^{13}C distortionless enhancement by polarization transfer (DEPT) MRI.[19] This approach has been used to monitor the competitive etherification and hydration reactions of 2-methyl-2-butene (2M2B) over an ion-exchange resin in a fixed-bed reactor. The etherification and hydration reaction products are *tert*-amyl methyl ether (TAME) and *tert*-amyl alcohol (TAOH). Figure 5a–c shows how the double phase-encoded ^{13}C DEPT-MRI pulse sequence achieves both spatial and spectral resolution within the reactor. Figure 5a illustrates a ^{1}H 2D spin-echo image through the reactor, which is overlaid with a grid showing the location of the two orthogonal phase-encoded planes (z and x). The intersection of the white lines marks the center of each volume from which the data have been taken. The corresponding real-space volume elements are given in Figure 5b. The individual volume elements have been separated but actually represent a continuous array, leading to the corresponding high-quality ^{13}C NMR spectra shown in Figure 5c. It is important to note that the decreasing signal intensity towards the walls of the bed arises from the smaller volumes from which the data are sampled. Figure 5d shows the spatially resolved ^{13}C DEPT-NMR spectra recorded for the competitive etherification and hydration reactions of 2M2B to TAME and TAOH. The spectra were obtained for the different heights within the catalytic reactor as indicated in Figure 5a. The average conversion and selectivity from these spectra acquired from columns 1–5 at each axial location are summarized in Figure 5e. Over a 1.5 cm height of the catalytic bed, it was found that the conversion increased by about 30%, while the selectivity lies in the range of 75–80%. At any given axial position, both conversion and selectivity also vary across the transverse plane. In particular, it was found that the relatively low conversions in columns 1 and 5 are consistent with the faster flow rates and hence with reduced feed–catalyst contact time observed near the reactor wall.

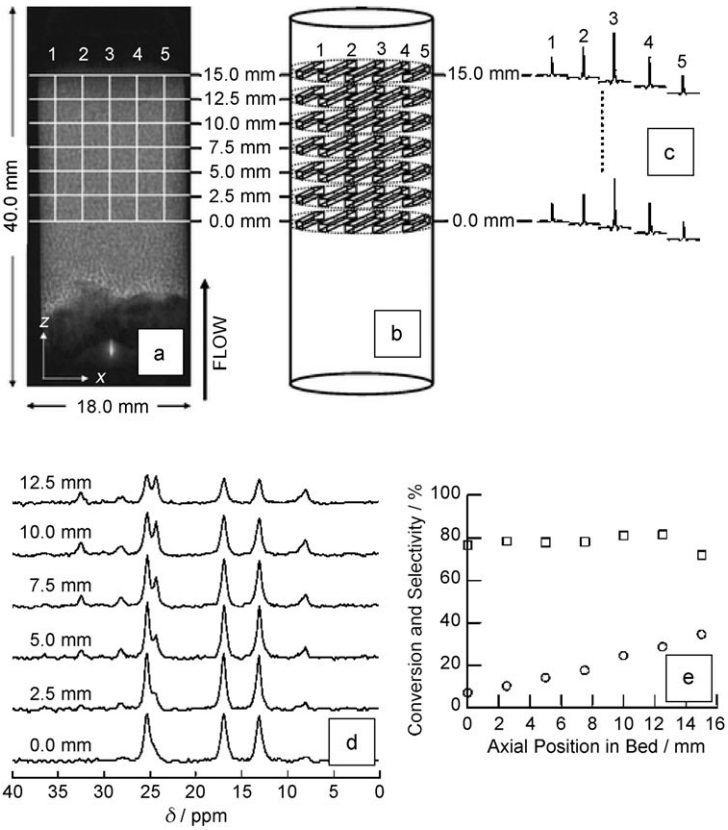

Figure 5. Schematic illustration of how the double phase-encoded ^{13}C DEPT-MRI pulse sequence achieves both spatial and spectral resolution within a catalytic reactor for the competitive etherification and hydration reactions of 2-methyl-2-butene (2M2B) over an Amberlyst-15 ion-exchange resin. a) A 2D ^{1}H spin–echo image taken through the reactor and overlaid with a grid showing the location of the two orthogonal phase-encoded planes. b) The corresponding real-space volume elements. c) The ^{13}C NMR spectra associated with these volume elements. d) Spatially resolved ^{13}C DEPT-MRI spectra recorded for the conversion of 2M2B to *tert*-amyl methyl ether (TAME) and *tert*-amyl alcohol (TAOH). The spectra are recorded at different heights within the bed. e) Conversion (○) and selectivity to TAME (□) as a function of the axial position in the catalytic bed. Reproduced from reference [19], copyright Royal Society of Chemistry, 2005.

Making use of the same spatially resolved ^{13}C DEPT-MRI method, Sederman et al. successfully investigated 1-octene hydrogenation over a 1 wt% Pd/Al_2O_3 catalyst in a trickle-bed reactor.[20] Figure 6a,b shows 2D maps of ^{13}C DEPT-MRI spectra spatially resolved along the length of the catalytic reactor. Any horizontal cut through the 2D maps recovers a ^{13}C 1D DEPT-NMR spectrum, as shown in Figure 6d,e. The two solid horizontal white lines indicate the limits of the catalyst packing within the bed. Above and below the white

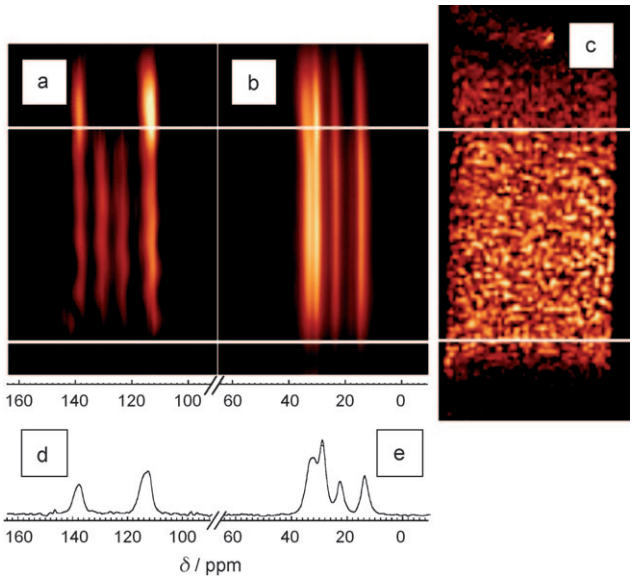

Figure 6. 2D map of ^{13}C DEPT-MRI spectra recorded along the length of a trickle reactor bed for 1-octene isomerization and hydrogenation over a 1 wt% Pd/Al_2O_3 catalyst. Separate acquisitions were made for the a) olefinic and b) aliphatic regions of the ^{13}C DEPT-MRI spectra. c) 2D ^{1}H MRI image of the spatial distribution of liquid within the catalyst bed. Higher liquid contents are identified by lighter colors. The white horizontal lines indicate the limits of the catalyst packing, separating the catalyst from the pure Al_2O_3. d, e) Corresponding ^{13}C DEPT-MRI spectra measured at the interface between the 1 wt% Pd/Al_2O_3 catalyst and Al_2O_3 corresponding to the 2D maps in (a) and (b), respectively. Reproduced from reference [20], copyright Springer, 2005.

lines, the reactor is packed with pure alumina support. Since the reactor was operated under H_2-poor conditions, significant conversion into the product octane was neither expected nor observed. Figure 6c shows a ^{1}H 2D image of liquid distribution within the catalyst bed. ^{1}H signals from all liquid species present were recorded, and higher liquid content corresponds to lighter color. Qualitative interpretation of the data confirms that above the Pd/Al_2O_3 catalyst material, only 1-octene exists within the bed, as identified by peaks occurring at around $\delta = 114$ and 139 ppm. As soon as the 1-octene feed reaches the catalyst material, additional peaks in the spectrum are observed at around $\delta = 124$ and 131 ppm, indicating the formation of predominantly 2-octene isomers. The total integrated intensity of the spectral features in the olefinic region decreases, thus confirming that some hydrogenation to octane has occurred along the length of the bed. More detailed analysis of the individual spectra shows 1) a loss of spectral intensity at around $\delta = 34$ ppm, consistent with loss of 1-octene, 2) the appearance of a peak at $\delta = 18$ ppm confirming the formation of *trans*-2-octene, and 3) that relatively little 3- and 4-octenes are formed, as no spectral intensity is detected at around $\delta = 129$ ppm.

A final example of the application of in situ MRI to study catalytic reactions in reactors involves the use of para-hydrogen (para-H_2). Gas-phase MRI suffers from low sensitivity, which makes it difficult to image void spaces in porous materials. This limitation has led to the use of hyperpolarized gases, such as ^{129}Xe, ^{3}He, and ^{83}Kr, but hyperpolarized noble gases and polarization instruments are generally expensive. Another method for producing hyperpolarized fluids is by using para-H_2, which has zero total nuclear angular momentum ($I = 0$) and is therefore not detectable in an NMR experiment. This para-H_2 is cheap, as it can be easily obtained by passing hydrogen gas over an iron-containing catalyst at the temperature of liquid N_2 (−196 °C) Bouchard et al. used the signal enhancement by para-H_2 to image a catalytic gas-phase reaction. More specifically, they investigated the hydrogenation of propene to propane by a silica-supported Wilkinson catalyst ($[RhCl(PPh_3)_2PPh_2(CH_2)_2]$-$SiO_2$).[21,22] The protons derived from para-H_2 in the formed propane preserve their nuclear spin singlet state. The reactant–product mixture is adiabatically transferred to the high field of the NMR magnet, leading to specific population differences according to an experimental scheme referred to as ALTADENA (adiabatic longitudinal transport and dissociation engenders net alignment). The resulting NMR signal is enhanced compared to what is achievable with thermal population of spin states. It was found that a strong enhancement could be observed using para-H_2 when comparing the 2D images of a propene gas-phase flow in a porous medium from the unpolarized propene and the ALTADENA-polarized propane peaks.

2.1.2. *Probing Rh/Al_2O_3 and $Rh/Pt/Al_2O_3$ Catalysts During the Partial Oxidation of Methane with Spatially Resolved X-ray Absorption Spectroscopy*

The catalytic partial oxidation of methane over supported noble metal particles such as rhodium and platinum is regarded as one of the most promising processes for the production of hydrogen. Grunwaldt et al. observed a strong spatial dependence of the Rh oxidation state in a microreactor filled with Rh/Al_2O_3 catalyst material during the partial oxidation of methane to CO, H_2, CO_2, and H_2O. 2D mapping of Rh species in the catalytic reactor was possible using XANES spectroscopy (XANES = X-ray absorption near-edge structure) with a CCD X-ray camera in a reaction cell fitted with a gas supply and coupled to online mass spectrometry.[23] Figure 7a illustrates the experimental approach. The method was used to determine the distribution of oxidized and reduced Rh species as a function of position in the reactor, reaction time, reaction temperature, and space velocity. Figure 7b–g depicts the 2D X-ray transmission images of the catalyst taken at different energies. At each energy, metal particles can be identified by their specific X-ray absorption. Below the energy of the Rh K edge (23220 eV, Figure 7b), the X-ray absorption is much smaller than above the edge (23230, 23235, and 23240 eV, Figure 7d–f). Moreover, the absorption is similar over the whole catalyst bed below the Rh K edge, whereas above the Rh K edge, in particular at 23235 and 23240 eV, the X-ray absorption is higher on the left side of the reactor, near the gas inlet. The higher X-ray absorption (corresponding to the brighter spots on the left) can be explained by the presence of more oxidized Rh on the left side, as oxidized Rh species are much stronger white-light absorbers. For each position in the reactor area, the X-ray absorption spectrum is reconstructed by compar-

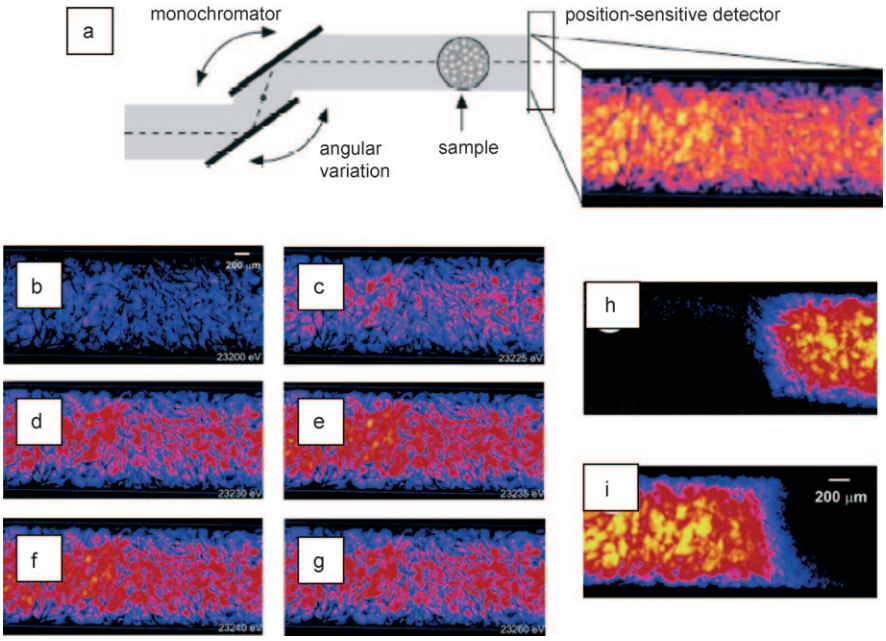

Figure 7. a) Side view of the experimental setup for spatially resolved X-ray absorption spectroscopy of a catalytic reactor for measuring a Rh/Al_2O_3 catalyst during the partial oxidation of methane. The full-field imaging makes use of a position-sensitive detector and a conventional step-scanning monochromator. b–g) Flat- and dark-field-corrected 2D X-ray transmission images of the Rh/Al_2O_3 catalyst inside the spectroscopic cell at different energies at 283 °C. h, i) 2D plots of the amount of reduced (h) and oxidized (i) Rh species obtained from the data shown in (b)–(g). Reproduced from reference [23], copyright American Chemical Society, 2006.

ison with the spectra of different Rh species and fitting by least-squares methods. In this way, it has been possible to create 2D maps of the Rh oxidation-state distribution in the catalytic reactor. An example of such a 2D map is shown in Figure 7h,i. On the right side, mainly Rh^0 is found (Figure 7h), while on the left side Rh^{3+} is detected (Figure 7i). There is a sharp (ca. 100–200 μm) cone-shaped gradient of reduced Rh species.

In subsequent studies, Hannemann et al. and Grunwaldt et al. showed that the position of the Rh^{3+}/Rh^0 front is a function of the space velocity and the reaction temperature.[24,25] It was found that the Rh^{3+}/Rh^0 front moved towards the reactor outlet (overall more Rh^{3+} in the reactor) with increasing space velocity. As expected, these changes in space velocity were reflected in the catalytic performance, and the yield of H_2 and CO decreased. Alternatively, an increase in temperature shifts the Rh^{3+}/Rh^0 front towards the reactor inlet (overall less Rh^{3+} in the reactor). These spatial reactor gradients can be related to the reaction mechanism. Below the ignition temperature of the partial methane oxidation reaction, Rh is mainly in its oxidized state. Above the ignition temperature, the amount of H_2 and CO produced is correlated to the position of the Rh^{3+}/Rh^0 front in the reactor. The front shifts towards the reactor inlet when the selectivity for H_2 and CO increases. Both a catalytic combustion and reforming mechanism and a direct particle oxidation mechanism to H_2O and CO_2 have been reported. As long as Rh remains in the oxidized state, methane is totally combusted. The appearance of H_2 and CO in the gas outlet coincides with the formation of Rh^0 species in the downstream part of the reactor, which promotes the catalytic combustion and reforming.

2.1.3. *Imaging Pt–Ba/CeO_2 NO_x Storage and Reduction, Cr/Al_2O_3 Alkane Dehydrogenation, and Pt-Based Electrocatalysts with Infrared, Raman, and UV/Vis Spectroscopy*

Urakawa et al. investigated a Pt–Ba/CeO_2 NO_x storage–reduction (NSR) catalyst by a combination of diffuse reflectance infrared Fourier transform (DRIFT) and Raman spectroscopy.[26] The combined approach is based on a switch between DRIFT and Raman spectroscopy within a single setup. The plug flow cell design, schematically illustrated in Figure 8a, allows fast exchange of gaseous atmosphere between lean (oxidative atmosphere) and rich (reductive atmosphere) periods. The spectral detection perpendicular to the axial direction of the catalyst bed allows gradient profiling and identification of chemical species along the bed. During the lean periods, NO is oxidized to NO_2 over platinum and stored on barium oxide in the form of nitrates, whereas during rich periods the stored NO_x is released and reduced to N_2 over platinum; concomitantly the barium oxide is regenerated for NO_x storage. Figure 8b shows the NO_x concentrations during an NSR cycle. During the first 30 s of the lean period, nearly complete storage of NO_x was observed. Afterwards the storage rate dropped but still showed approximately 90% storage of the incoming gaseous NO_x. Very little NO_2 was observed in the off-gas during the lean period, indicating that all NO_2 formed over the platinum sites was captured by the barium oxide or CeO_2 surface. After switching to rich conditions, the NO concentration decreased rapidly. The 2D maps of the DRIFT and Raman spectra during an NSR cycle at three reactor locations are given in Figure 8c–e and Figure 8f–h, respectively. Remarkable spectral differences were observed along the catalyst bed. The formation of nitrites and nitrates was significantly delayed and the band intensities decreased considerably on moving from the front to the back position. In the DRIFT spectra (Figure 8c–e), the most striking difference during the lean period, besides the band intensities, is the formation of nitrites. These species were observed immediately at the front position but were delayed by 70 and 120 s at the middle and back positions, respectively. On the other hand, nitrates were formed from the beginning of the lean period, independent of the bed position. The temporal profiles of surface nitrate bands at 1028 and 1570 cm^{-1} were similar to that at 1260 cm^{-1}. The chemical changes that occur during the NSR cycle are likely accompanied by gradual structural reordering, that is, changes in the crystallinity of the solid during nitrate penetration from the surface into the bulk of the barium oxide. Furthermore,

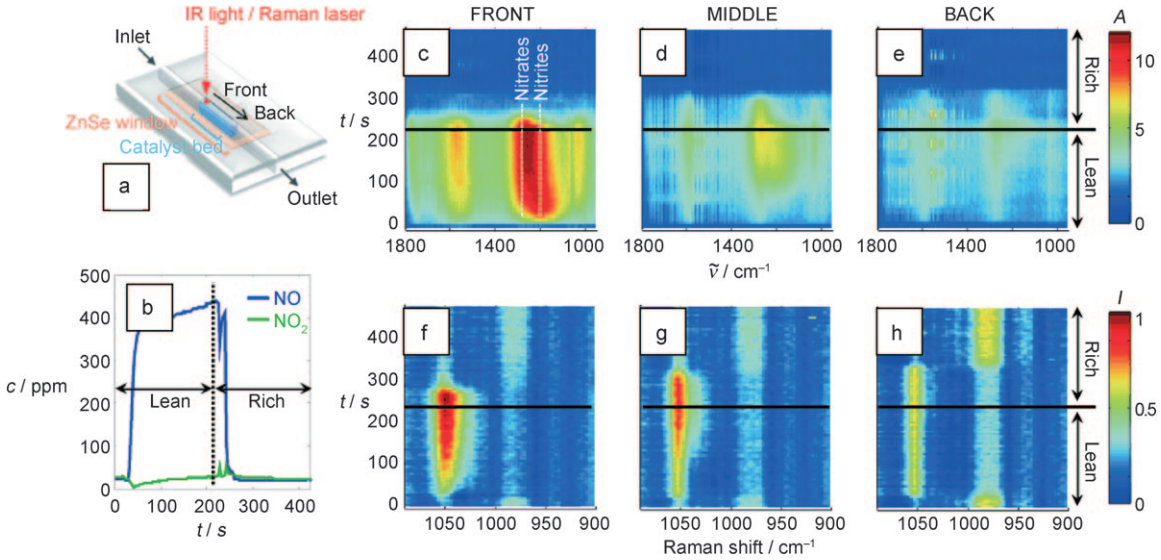

Figure 8. a) Schematic illustration of the in situ IR/Raman spectroscopy reaction cell for space- and time-resolved experiments. b) NO_x concentration as a function of time for lean and rich reaction conditions. c–e) 2D plots of the time-resolved DRIFT spectra during NSR at the front, middle, and back of the catalyst bed. f–h) 2D plots of the time-resolved Raman spectra during NSR at the front, middle, and back of the catalyst bed. Reproduced from reference [26].

during the rich period, a remarkable difference in the reduction behavior of nitrites and nitrates was detected. Nitrites were first reduced or desorbed from the surface and then the reduction of nitrates followed, as clearly indicated by a significant delay of the corresponding signals at the middle and back positions of the catalytic reactor. The large amount of NO released from the catalyst at the beginning of the rich period is likely related to the disappearance of surface nitrites, thus suggesting decomposition of the nitrites and consequent release of NO into the gas phase. Moreover, the Raman spectra shown in Figure 8 f–h clearly indicate the difference in the amount of formed bulk $Ba(NO_3)_2$. At the front position, the amount increased drastically. However, the increase was considerably less prominent towards the back position. A similar tendency is also evident in the DRIFT spectra, which show much less intense surface nitrite and nitrate bands towards the back position. Remarkably, 90% of the NO_x remained stored at the end of the lean period, but the majority of the NO_x was stored at the front of the catalyst bed (by barium oxide).

Nijhuis et al. investigated a Cr/Al_2O_3 propane dehydrogenation catalyst during successive dehydrogenation–regeneration cycles using a combination of UV/Vis diffuse reflectance spectroscopy and Raman spectroscopy.[27] The experimental setup is shown in Figure 9a. A reactor tube with optical-grade quartz windows was placed vertically in the center of a long tubular oven block that has a horizontal hole directed at the catalyst bed for 1D Raman measurements on one side and a vertical slit in the furnace for 1D UV/Vis measurements at different bed heights on the opposite side. Figure 9b shows the catalytic performance during a 4 h dehydrogenation cycle. There is a clear trend in the catalytic conversion over time. The conversion increases during the first 2 h and then slowly decreases. The high initial propane conversion is caused by the combustion of some propane as it reduces the catalyst. This effect also explains the lower initial selectivity. Except for water and carbon dioxide from propane combustion, the only coproducts that are observed in a significant amount are ethene and methane. The remainder of the 20% unselectively converted propane must therefore end up as coke. More direct evidence on the amount and type of coke formation could be obtained with UV/Vis and Raman spectroscopy in the reactor bed (Figure 9c–e). Figure 9c shows the UV/Vis/NIR absorbance measured at 1000 nm, where no specific absorption bands are present, at four different bed heights. This absorbance was used to monitor the darkening of the sample during propane dehydrogenation. For Raman spectroscopy, the intensities of the two main coke bands at 1577 and 1320 cm^{-1} in the middle of the reactor bed are shown (Figure 9d). The different coke formation rates at the different bed heights in Figure 9c clearly show that coke is primarily produced at the end of the reactor bed, indicating that it is formed primarily in a secondary reaction from the product propene. Figure 9d shows that initially the coke band at 1320 cm^{-1} is more intense. As the experiment proceeds, this band becomes less intense compared to that at 1577 cm^{-1}. This relative shift is consistent with the gradual growth of a graphitic-type coke layer on the catalyst over time. Combining the information from Figure 9b,c, it is apparent that during the first 2 h of dehydrogenation coke forms slowly on the catalyst, while at the same time the catalytic activity increases. Considering that the catalyst was already reduced and that the catalyst is not reduced further than Cr^{3+}, the most probable explanation for the activity increase is that coke formation is beneficial for catalytic activity. After 2 h of reaction, the visible amount of coke on the catalyst increases, while at the same time the conversion begins to drop. It should be noted that although after 2 h the rate at which the UV/Vis absorbance of the sample increases becomes higher, this does not necessarily

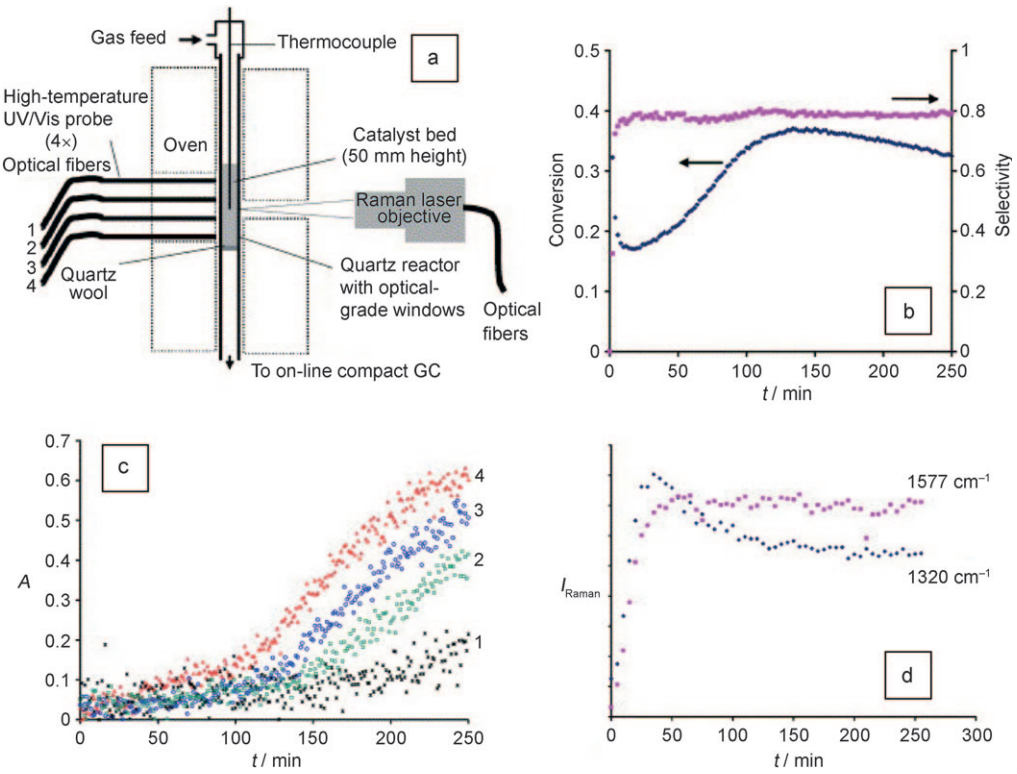

Figure 9. a) Schematic illustration of the in situ UV/Vis/NIR / Raman setup for measuring space- and time-resolved spectra of a Cr/Al_2O_3 propane dehydrogenation catalyst in a fixed-bed reactor. b) Selectivity and conversion during a single propane dehydrogenation cycle at 550 °C. c) UV/Vis/NIR trends of catalyst absorbance at 1000 nm as a function of reaction time showing the coke formation at different bed heights in the reactor bed (1 = top, 4 = bottom; see (a)). d) Raman intensities of bands of two predominant coke species as a function of reaction time. Reproduced from reference [27], copyright Elsevier Science B.V., 2004.

mean that the actual coke formation rate also increases. As the selectivity of the dehydrogenation reaction does not change, the data imply that neither more propane nor more propene is converted into coke. The increase in absorbance can be best explained by the coke patches increasing in size and starting to connect and cover the entire catalyst surface, effectively blocking the scattering and reflection of light. At the same time, as coke starts to cover the chromium oxide, the catalyst becomes less accessible, and its activity drops. Since this front of complete coke coverage of the catalyst starts at the exit of the reactor and then moves slowly forward towards the entrance, the overall conversion drops slowly.

A final example originates from Morschl et al., who imaged catalytic reactions at the Pt/electrolyte interface in an electrochemical cell using attenuated total reflection infrared spectroscopy (ATR-IR) in combination with a focal plane array detector.[28] This method allows collection of in situ microscopic images of the catalyst material and its adsorbates. More specifically, the authors investigated the electrooxidation of CO over polycrystalline platinum. Figure 10 shows 2D plots of the integrated CO peak intensities versus space for different preset currents. Red indicates a high CO coverage, whereas blue indicates a low one. For applied currents up to 1.3 mA, the CO peak intensities exhibit only slight deviations from those of the surface with maximum CO coverage. Thus, this region of the electrode is still completely covered by CO. When the applied current is further gradually increased to

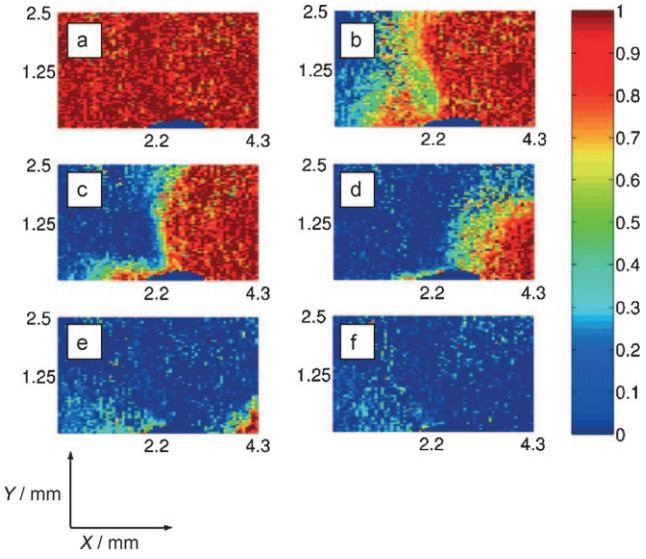

Figure 10. 2D plots of the integrated CO peak intensities versus space for different preset currents for polycrystalline Pt at the Pt/electrolyte interface during the electrooxidation of CO as measured with ATR-IR spectroscopy in combination with a focal plane array detector: a) 0.3, b) 1.4, c) 1.5, d) 1.7, e) 1.75, and f) 1.8 mA. Red colors indicate a high CO coverage; blue colors indicate low CO coverage. Reproduced from reference [28], copyright American Chemical Society, 2008.

1.8 mA, the probed area shows two different regions: one in which the integrated intensity is still unchanged from the completely covered surface and one in which no CO peaks are detected (the region is almost free of CO). The higher the set current, the larger the region that is practically free of adsorbed CO. These regions can be correlated to activity: an inactive, CO-covered region and an active, CO-depleted region.

2.2. Spatial Heterogeneities at the Level of Millimeter-Sized Catalyst Bodies

2.2.1. Tuning the Formation and Disintegration of Keggin-Type Co–Mo Complexes Inside Al_2O_3-Based Catalyst Bodies During Impregnation by a Combination of Raman and UV/Vis Microscopy

By making use of a combination of Raman and UV/Vis microscopy Bergwerff et al. monitored the disintegration and formation of $[H_2PMo_{11}CoO_{40}]^{5-}$ complexes inside the pores of Al_2O_3 catalyst bodies.[29] The experimental approach (Figure 11) consists of taking one or more catalyst bodies

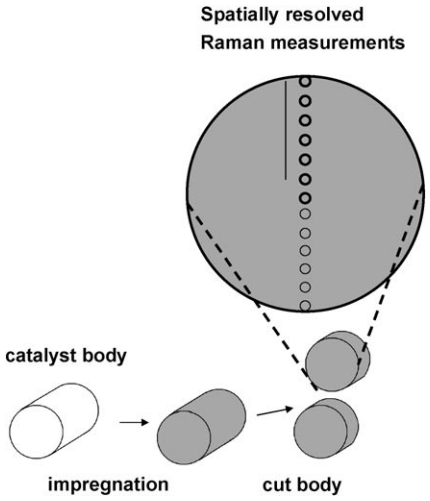

Figure 11. Layout of spatially resolved measurements on catalyst bodies. An individual pellet is bisected or sliced after impregnation, drying, or calcination. 1D spectra are then measured with Raman, IR, or UV/Vis microscopy. The slicing is performed at specific times *x* during the impregnation process. Reproduced from reference [29].

from the synthesis vessel at different times during catalyst impregnation. This step is followed by cleavage of the catalyst bodies perpendicular to their *z* (long) axis. Cross-section scans yield 1D plots of spectra at different positions inside the individual bisected catalyst bodies. The recording of such linescans with Raman spectroscopy was initially proposed by Mang et al.[30] and fully exploited by Bergwerff et al.[31] The method was later extended by Van de Water et al.[32] and Espinosa Alonso et al.[33] for recording 1D linescans with UV/Vis and IR microscopy.

When the experimental approach in Figure 11 was applied to the impregnation of an aqueous $[H_2PMo_{11}CoO_{40}]^{5-}$ solution onto Al_2O_3 catalyst bodies, Raman and UV/Vis spectra were obtained at different positions inside the extrudates after 15 and 180 min of impregnation.[29] The space- and time-resolved Raman and UV/Vis spectra are shown in Figure 12. At 15 min after the start of impregnation, the presence of the

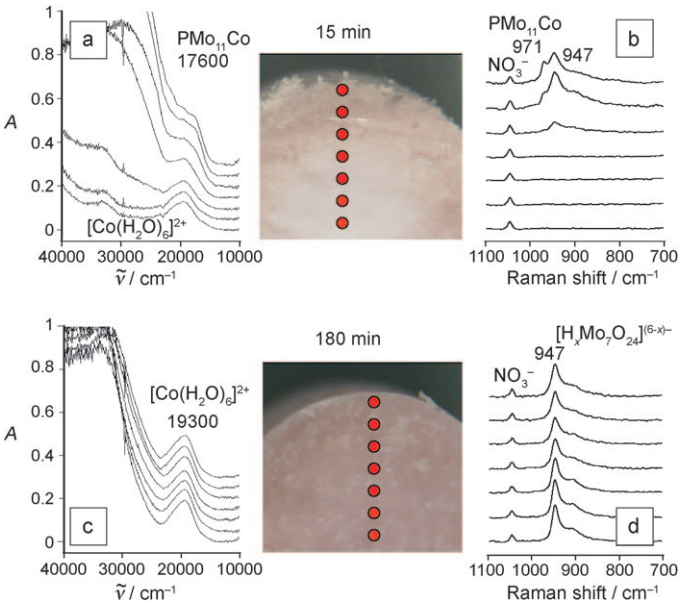

Figure 12. Space- and time-resolved UV/Vis (a, c) and Raman (b, d) spectra recorded for a bisected Al_2O_3 catalyst body after 15 (a, b) and 180 (c, d) min of impregnation with an aqueous solution containing $[H_2PMo_{11}CoO_{40}]^{5-}$. The images show the catalyst bodies, and the red dots indicate the positions at which spectra were recorded. Reproduced from reference [29].

$[H_2PMo_{11}CoO_{40}]^{5-}$ complex inside the Al_2O_3 pores, as evidenced by the characteristic Raman band at 971 cm^{-1}, is observed only in the outer shell of the bodies (Figure 12b). Closer to the center of the alumina bodies, Mo is present as a $[H_xMo_7O_{24}]^{(6-x)-}$ species, as can be concluded from the position of the main Mo–O stretching vibration at 947 cm^{-1}. However, near the core of the catalyst body, the absence of any Mo–O vibration peak indicates that no Mo^{6+} complexes are present. These Raman microscopy observations are in full agreement with those from UV/Vis microscopy recorded at the same points of the bisected pellet 15 min after the start of impregnation (Figure 12a). Indeed, a clear shoulder is observed at 17600 cm^{-1}, and the onset of the $O \rightarrow Mo^{6+}$ charge-transfer absorption band is shifted into the visible region of the spectrum. This finding confirms the presence of the $[H_2PMo_{11}CoO_{40}]^{5-}$ complex in the outer shell of the support bodies after 15 min. In contrast, closer to the core of the pellets all Co^{2+} seems to be present as $[Co(H_2O)_6]^{2+}$, and the $O \rightarrow Mo^{6+}$ charge-transfer absorption band is absent, thus confirming the Mo concentration gradient observed in the Raman microscopy measurements. At 180 min after the start of impregnation, a homogeneous distribution of the $[H_xMo_7O_{24}]^{(6-x)-}$ complex is observed throughout the catalyst bodies. The intensity of the 947 cm^{-1} Raman peak relative to that of the NO_3^- internal standard is identical for all positions inside the Al_2O_3 bodies (Figure 12d). This result is in line with

the observation of the $O \rightarrow Mo^{6+}$ charge-transfer absorption band at all positions along the cross-section (Figure 12c). A homogeneous distribution of the $[Co(H_2O)_6]^{2+}$ ion is also obtained, as the intensity of the Co^{2+} d–d transition at 19300 cm^{-1} is the same for all positions along the cross-section of the catalyst bodies.

The observations described above can be rationalized as follows. Phosphate is known to react with the Al_2O_3 surface in acidic environments to form a surface $AlPO_4$ phase. In this way, phosphate is withdrawn from the solution inside the Al_2O_3 pores. Hence a decreasing phosphate gradient can be expected towards the center of the catalyst body. As the impregnation solution containing $[H_2PMo_{11}CoO_{40}]^{5-}$ complexes penetrates the alumina pellets, reaction of phosphate with the Al_2O_3 surface results in a lower phosphate concentration in the solution inside the pores of the support body. As a consequence, $[H_xMo_7O_{24}]^{(6-x)-}$ and $[Co(H_2O)_6]^{2+}$ are formed. These species make their way toward the core of the bodies, each at its own rate. Experimental evidence for the surface reaction between Al_2O_3 and phosphate was found by Lysova et al.[34] using ^{31}P MRI to monitor the dynamics of the impregnation of an Al_2O_3 catalyst body in the presence of a H_3PO_4 solution. Comparison of the ^1H images of water and the ^{31}P images of phosphate revealed the strong interaction (and therefore slow transport) of the latter with the Al_2O_3 support. The 2D ^{31}P MRI images demonstrate the distribution of phosphate in the alumina pellets (Figure 13). The images in Figure 13a,b reflect the spatial distribution of the phosphate in solution only. It is expected that phosphate adsorbed on the walls of the alumina pores does not contribute significantly to the observed images. The correlation of the spatial distributions of dissolved and adsorbed phosphate has been established as well. To do so, the impregnation process was interrupted about 100 min after its initiation. The selected pellet was dried and a 2D ^{31}P MRI image of the phosphate in the solid phase was measured. The result (Figure 13c) indicates an egg-shell distribution of phosphate. In another experiment, the impregnation process was carried out to completion. The pellet was dried and imaged 18.5 h after starting the process. As can be seen from Figure 13d, the liquid-phase and solid-phase distributions of phosphate do correlate with those during impregnation (Figure 13b), thus validating the applicability of MRI for dynamic impregnation studies. This study shows that the amount of free phosphate is a crucial factor in the formation of specific Co–Mo complexes within the pores of the alumina catalyst bodies. With this knowledge in mind, it was possible to form $[H_2PMo_{11}CoO_{40}]^{5-}$ complexes inside Al_2O_3 catalyst bodies by increasing the amount of free phosphate in the initial impregnation solution.[29] In this manner, the reaction of free phosphate with the support results in a lower phosphate concentration inside the pores, thereby creating optimal conditions for the formation of the $[H_2PMo_{11}CoO_{40}]^{5-}$ complex.

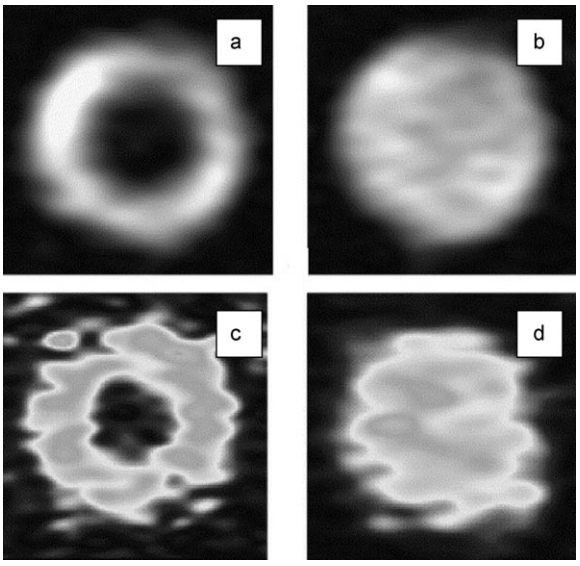

Figure 13. 2D ^{31}P MRI images demonstrating the distribution of phosphate in Al_2O_3 catalyst bodies. a,b) Distribution of phosphate in the liquid phase during the impregnation of the catalyst body with an aqueous solution of H_3PO_4 approximately 100 min (a) and 18.5 h (b) after starting the impregnation process. c,d) Distribution of phosphate in the solid phase after terminating the impregnation after approximately 100 min (c) and 18.5 h (d) and drying the catalyst bodies. Lighter shades of gray correspond to higher signal intensity. Reproduced from reference [18], copyright Elsevier, 2007.

2.2.2. *Altering the Macrodistribution and Speciation of Co Complexes within Al_2O_3-Containing Catalyst Bodies during Impregnation, Drying, and Calcination as Evidenced by a Combination of Magnetic Resonance Imaging and UV/Vis Microscopy*

Impregnation solutions used in industrial catalyst preparation processes usually contain metal precursor salts and organic complexing agents such as citrate. As a consequence, different metal chelate complexes can be formed in the impregnation solution as a function of pH value and metal-ion concentration. Since it is known that pH value gradients may occur inside catalyst bodies after impregnation, different interactions between the metal complexes and the support surface are expected. These differences may lead to different transport rates of these compounds through the support bodies. Bergwerff et al. have shown how the transport phenomena and related macrodistribution of different types of Co^{2+} complexes inside Co/Al_2O_3 catalyst bodies can be visualized by a combination of MRI and UV/Vis microscopy.[35,36] While UV/Vis microscopy provided molecular information on the Co^{2+} complexes after bisecting catalyst bodies at specific times during impregnation, the macrodistribution of Co^{2+} complexes inside the catalyst bodies can be determined by MRI. Indeed, MRI can be used indirectly to image paramagnetic species, such as Co^{2+} complexes, as their unpaired electrons induce a decrease in the relaxation time of the ^1H nuclei. Using a specific pulse sequence it is possible to distinguish between perturbed and unperturbed ^1H nuclei of the impregnated solution occluded in the catalyst-body pores. In other words, the proportion of paramagnetic nuclei can be monitored in space and time within a catalyst body by monitoring the quenching of the ^1H MRI signal.[35–37]

The proof of principle is illustrated in Figure 14 for the impregnation of an Al_2O_3 catalyst body with a 0.2 M $Co(NO_3)_2$ solution. Figure 14a shows a set of 2D ^1H images of an Al_2O_3

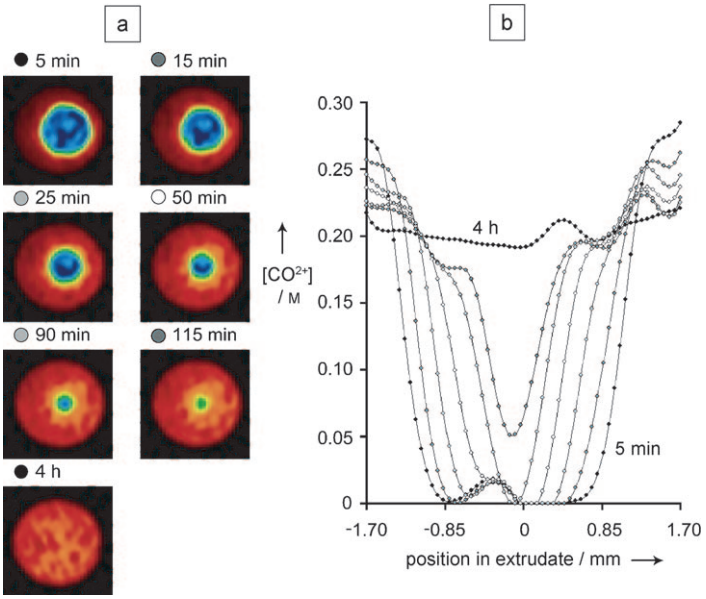

Figure 14. a) 2D ^{1}H MRI images of an Al_2O_3 catalyst body at different times after impregnation with a 0.2 M $Co(NO_3)_2$ solution. Blue: high ^{1}H NMR signal intensity (low Co^{2+} concentration); red: low ^{1}H NMR signal intensity (high Co^{2+} concentration). b) Quantitative Co^{2+}-ion distribution plots along the position in the catalyst body, derived from the 2D ^{1}H MRI images. Reproduced from reference [35].

catalyst body at different times after impregnation, while Figure 14b shows a quantitative Co^{2+}-ion distribution plot derived from the 2D images. It can be concluded that the transport of Co^{2+} ions after pore-volume impregnation takes place in two distinct steps. In a first step, Co^{2+} complexes are transported into the catalyst body as they travel with the capillary flow of the water solvent. Adsorption of Co^{2+} complexes on the Al_2O_3 surface takes place as coordinating water molecules are exchanged for support oxygen atoms, and a Co^{2+} concentration gradient is instantly established after impregnation. Since impregnation was carried out without excess solution, the total amount of Co^{2+} inside the catalyst body remained constant as a function of time after impregnation. Therefore, the Co^{2+} concentration near the outer surface of the catalyst body was initially higher than 0.2 M. The concentration gradient over the catalyst body resulted in diffusion of Co^{2+} complexes towards the center. The Co^{2+} front travels into the catalyst body, and after 4 h a homogeneous distribution of the metal complexes and an average Co^{2+} concentration of 0.2 M were observed.

In a subsequent characterization study, the influence of citrate on the mobility and chemical nature of Co^{2+} complexes within Al_2O_3 catalyst bodies was investigated. As an example, the impregnation with an aqueous cobalt citrate solution at pH 5 for a cobalt/citrate ratio of 1:1 will be discussed. Figure 15a shows the 2D ^{1}H MRI image obtained from the catalyst bodies after 15 h of impregnation. A sharp ring of low ^{1}H NMR signal intensity near the external surface of the catalyst bodies is formed immediately after impregnation. Since the red regions of the MRI image correspond to a high concentration of Co^{2+} complexes (blue regions indicate low Co^{2+} concentrations), the 2D MRI image clearly shows a sharp egg-shell distribution of Co^{2+} complexes. UV/Vis spectra recorded on the corresponding bisected catalyst body show an absorption band located at around 530 nm, which is due to Co^{2+} d–d transitions. This band is only clearly observed in the spectrum recorded near the external surface of the catalyst body, thus confirming the sharp egg-shell profile for this catalyst body. By systematic variation of the cobalt/citrate ratio and pH value of the impregnation solution, the macrodistribution of Co^{2+} complexes in the impregnated catalyst bodies could be varied from egg shell through egg white and egg yolk to uniform.

Another illustrative characterization study illustrating the power of spatially resolved methods uses UV/Vis microscopy to reveal the differences in macrodistribution and speciation of Co^{2+} ions within Al_2O_3 catalyst bodies after impregnation, drying, and calcination when Co^{2+}-containing aqueous and ethanol solutions are used for impregnation.[38] Van de Water et al. found that Co^{2+} ions tend to migrate more slowly towards the center of the catalyst body in an ethanol impregnation solution than in aqueous solution. UV/Vis spectra of the dried samples confirmed that there are still very few Co^{2+} ions in the center of the catalyst body for the ethanol-impregnated sample. More interestingly, however, the spectral changes observed for this sample and the complex spectra could be explained in terms of the formation of Co–Al hydrotalcite-like compounds, which are known to be formed by Co^{2+}-assisted alumina dissolution. By comparison, the UV/Vis spectra of the calcined sample impregnated in aqueous solution showed strong absorption bands indicative of the formation of supported Co_3O_4 nanoparticles. It could be deduced that the Co_3O_4 nanoparticles are rather homogeneously distributed

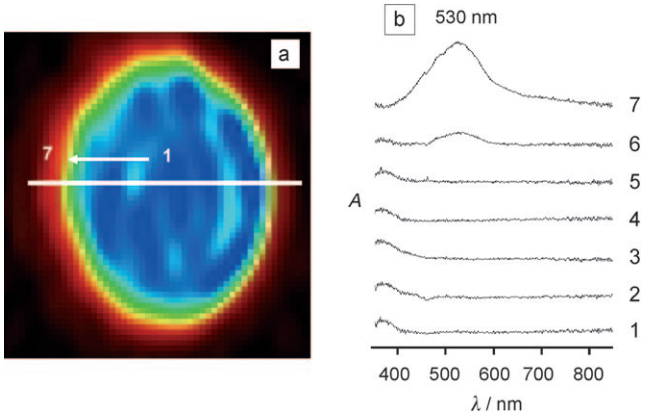

Figure 15. a) 2D ^{1}H MRI image of an Al_2O_3 catalyst body after 15 h of impregnation with a 0.2 M $Co(NO_3)_2$ solution containing 0.2 M citrate at pH 5. Blue: high ^{1}H NMR signal (low Co^{2+} concentration); red: low ^{1}H NMR signal (high Co^{2+} concentration). b) Corresponding 1D UV/Vis spectra recorded on the bisected Al_2O_3 catalyst body. The locations of the 1D measurement spots are indicated in the 2D ^{1}H MRI image. Reproduced from reference [36].

over the whole catalyst body, as no major differences between edge and center were detected. In contrast, the UV/Vis spectra of the ethanol-impregnated catalyst body after calcination were much more complex, and different regions were identified. The edge of the cross-section of the bisected catalyst body contained predominantly Co_3O_4, whereas in other places $CoAl_2O_4$ was formed. The latter phase evolved from the calcination of the Co–Al hydrotalcite compounds in places where no oxidation of Co^{2+} occurred during drying.

2.2.3. *Revealing the Formation of Anderson-Type Aluminum Polymolybdate and MoO_3 Crystallites during the Preparation of Mo/Al_2O_3 Catalyst Bodies by a Combination of Raman Microscopy and Tomographic Energy-Dispersive Diffraction Imaging*

Bergwerff et al. investigated the impregnation, drying, and calcination of an Al_2O_3 catalyst body with a molybdenum species.[39] Figure 16a shows a typical set of 1D Raman spectra recorded on bisected 19 wt% Mo/Al_2O_3 catalyst bodies after impregnation with an ammonium heptamolybdate (AHM) solution at pH 6. Raman bands at 895 and 940 cm^{-1} are observed at almost all positions inside the catalyst bodies. The presence of these two bands demonstrates the coexistence of MoO_4^{2-} and $Mo_7O_{24}^{6-}$ anions inside the Al_2O_3 pores. Interestingly, the Raman spectrum recorded on the outer Al_2O_3 surface exhibits intense bands at around 947, 899, 572, 355, and 218 cm^{-1}, indicating the presence of $[Al(OH)_6Mo_6O_{18}]^{3-}$ anions. After drying of the catalyst material, a white layer could be seen at the edges of the catalyst body, which was also visible in the corresponding scanning electron microscopy (SEM) image of a bisected catalyst body (Figure 16b). The Raman spectra of this bisected catalyst body (Figure 16c) indicates that the crust on the outside of the dried catalyst bodies consisted of $(NH_4)_3[Al(OH)_6Mo_6O_{18}]$, as evidenced by the intense Raman bands at 947, 899, 563, and 355 cm^{-1}. Similar Raman bands can also be observed in the lighter-color ring observed by SEM. In contrast, $Mo_7O_{24}^{6-}$ complexes were present in the bulk of the sample, as indicated by the 940 cm^{-1} Raman band. The $[Al(OH)_6Mo_6O_{18}]^{3-}$ crust is formed by ligand-promoted dissolution of the Al_2O_3 support, which results in the complexation of Al^{3+} ions by the oxomolybdate complexes under acidic conditions. The high Mo concentration at the outside of the catalyst bodies after impregnation allows a chain reaction to occur. Al^{3+} ions are generated by dissolution of the Al_2O_3 support and consumed in the formation of $[Al(OH)_6Mo_6O_{18}]^{3-}$. The low solubility of this compound leads to the precipitation of $(NH_4)_3[Al(OH)_6Mo_6O_{18}]$. The Al^{3+} concentration in the solution is thus kept low, and increasing amounts of Al_2O_3 are dissolved as a layer of $(NH_4)_3[Al(OH)_6Mo_6O_{18}]$ is formed. Inside the pores of the Al_2O_3 toward the inside of the catalyst body, the pH of the solution increases owing to the buffering action of the support, and MoO_4^{2-} complexes rather than Al^{3+} ions are formed. This species is transformed into $Mo_7O_{24}^{6-}$ during drying.

The egg-shell distribution in Mo/Al_2O_3 catalyst bodies can be confirmed with TEDDI, a technique which has been explored by Beale et al. for the spatially resolved characterization of catalyst bodies.[40] TEDDI is a noninvasive method to probe individual volume elements within catalyst bodies using a hard white X-ray beam (Figure 17a). The TEDDI detector signal contains both the diffraction pattern and a fluorescence peak from the defined volume element in the catalyst body, as illustrated in Figure 17b for the calcination of an individual Mo/Al_2O_3 catalyst body. By scanning over the whole y–z area of the catalyst body, 2D maps can be obtained from the $Mo_{K\alpha1,2}$ fluorescence as well as from the (311) γ-Al_2O_3 and (210) MoO_3 diffraction peaks. As an example, Figure 17c,d shows a specific y–z $Mo_{K\alpha1,2}$ 2D fluorescence map and a y–z MoO_3 2D diffraction map, respectively. From the latter image it can be seen that during calcination crystalline MoO_3 is formed from the $(NH_4)_3[Al(OH)_6Mo_6O_{18}]$ complexes and that these MoO_3 crystallites adopt an egg-shell distribution within the catalyst body. At the top and the bottom of the sample there are some brighter parts of the Mo

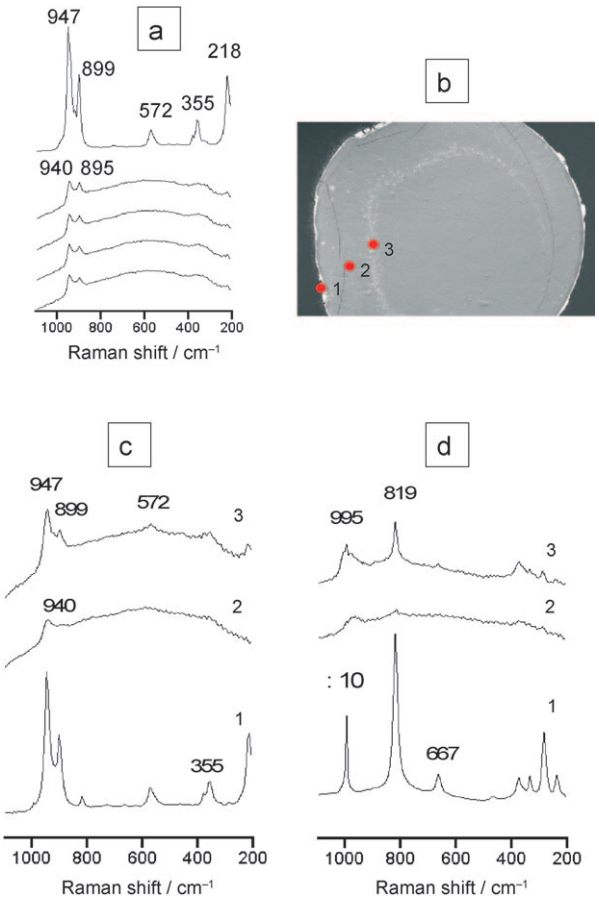

Figure 16. a) 1D Raman spectra of a bisected Al_2O_3 catalyst body impregnated with an aqueous solution containing 1.8 M ammonium heptamolybdate (AHM) at pH 6 after 1 h of impregnation. b) SEM image of a bisected Al_2O_3 catalyst body prepared in the same manner as for (a). c) 1D Raman spectra recorded at different positions of a bisected Al_2O_3 catalyst body impregnated with an aqueous solution containing 1.8 M AHM at pH 6 but now measured after drying at 120 °C. Measurement positions are similar to the points labeled 1–3 in (b). d) 1D Raman spectra of same sample as in (c) but now measured after calcination at 500 °C. Measurement positions are similar to the points labeled 1–3 in (b). Reproduced from reference [39], copyright Elsevier Science B.V., 2006.

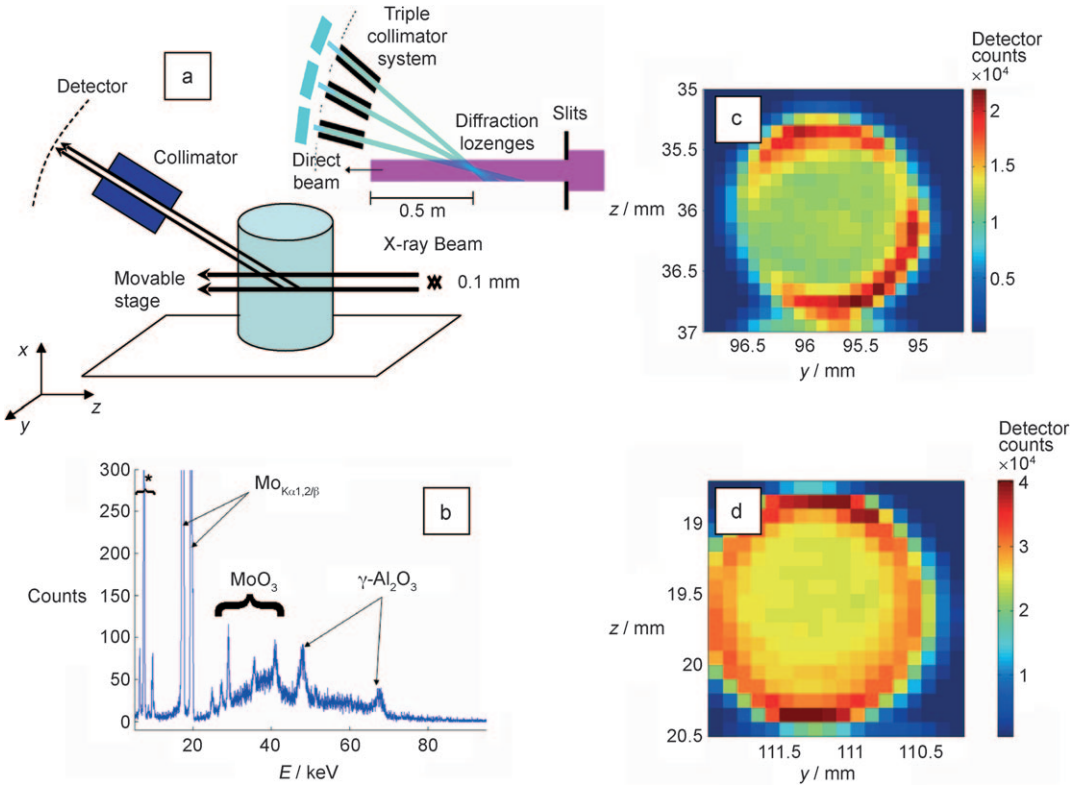

Figure 17. a) Layout of the experimental procedure used for measuring time- and space-resolved fluorescence and diffraction patterns from a specific volume within a catalyst body using tomographic energy-dispersive diffraction imaging (TEDDI). b) Detector signal from a Mo/Al_2O_3 catalyst body after calcination at 500 °C. c) Typical *y*–*z* map of the $Mo_{K\alpha1,2}$ fluorescence signals from a Mo/Al_2O_3 catalyst body after drying at 120 °C. d) Typical *y*–*z* diffraction map (based on the (210) reflection of MoO_3 crystals) from the Mo/Al_2O_3 catalyst body after calcination at 500 °C. Reproduced from reference [40].

corona, which are due to the shorter path length for the escaping fluorescence signal from the sample. This egg-shell distribution is confirmed by the 1D Raman spectra shown in Figure 16d. The Raman spectra originating from the edges of the catalyst bodies reveal the presence of bands at around 995, 819, 667, 378, 337, 290, and 242 cm^{-1}, which can be assigned to MoO_3. In other areas of the catalyst bodies amorphous MoO_x was detected.

2.3. Spatial Heterogeneities at the Level of Micrometer-Sized Zeolite Crystals

2.3.1. Insight into Diffusion Phenomena, Surface and Internal Transport Resistance, and Pore Architecture within Zeolites by Monitoring the Concentration of Molecules with Interference and Confocal Fluorescence Microscopy

Knowledge of the transport of molecules through zeolite materials and the relationship between pore structure and reactivity at the subcrystal level are important for the further development and application of such materials as heterogeneous catalysts. Different macroscopic techniques have been used to determine the uptake and release of guest molecules within zeolites. Unfortunately, they do not provide any information on the temporal evolution of internal concentration profiles. A powerful method, explored Kärger and coworkers,[41–44] to reveal space- and time-resolved details, is interference microscopy. This technique is based on the principle that the optical density of an individual zeolite crystallite depends on the concentration and nature of the guest molecules. As a consequence, the phase shift between two light beams, one of which passes through the zeolite crystal and the other through the surrounding atmosphere, is a measure of the average guest concentration along the direction of the light beam through the crystal. The principle of interference microscopy is schematically depicted in Figure 18a–c. Concentration profiles at different times can then be obtained by analyzing the interference patterns of the two beams. Figure 18e–g shows the application of interference microscopy to the adsorption and desorption of methanol on a ferrierite crystal (Figure 18d).[41] Almost immediately after the start of the adsorption experiment, a concentration profile associated with the roof-like part of the ferrierite crystal is established. During desorption of methanol this part of the profile disappears rapidly. Furthermore, the concentration gradients, which indicate the direction of mass transport into the crystal, are observed exclusively in the *y* direction of the central part of the crystal. These observations can be explained by the particular features of the channels that run along the *z* direction of the crystal. These channels are formed by 10-rings. As the channels that run along the *y* direction of the ferrierite crystal are composed of smaller 8-rings, intracrystalline mass transfer is expected to proceed much faster in the *z* direction. Thus, the roof-like part

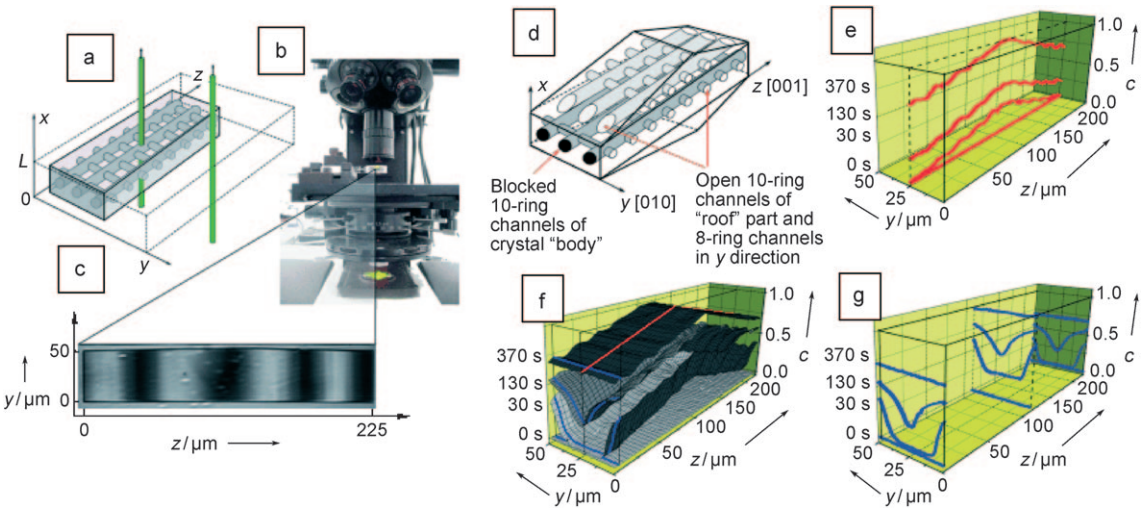

Figure 18. Principle of interference microscopy applied to the adsorption of methanol as guest molecule onto a ferrierite crystal: a) Two light beams, one passing through the crystal and one through the surrounding atmosphere. b) Interference microscope. c) Interference pattern arising from the two beams passing through media with different optical properties. d) Shape and pore structure of the ferrierite crystal. e) Concentration profiles of methanol in the *z* direction at $y = 25$ μm; f) 2D concentration profiles of methanol in the *y* and *z* directions. g) Concentration profiles of methanol in the *y* direction at the center of the crystal ($z = 120$ μm) and at two locations near the edges. Reproduced from reference [41].

of the crystal is occupied by methanol molecules immediately after the start of the adsorption experiment and is emptied immediately after the start of the desorption experiment. Another interesting feature of the concentration profiles of Figure 18 is that there are no concentration gradients in the *z* direction in the central parallelepiped part of the ferrierite crystal. Apparently, the channels along the *z* direction are blocked in this part of the crystal, whereas they are wide open in the roof-like part of the crystal. As a consequence, any mass transfer in the central part of the crystal can only occur in the *y* direction along the 8-ring channels. This pore blocking pattern means that mass transfer in the main part of the crystal occurs only in the *y* direction, even through the molecular mobility is much larger in the *z* direction because of the larger pore system. In other words, direct evidence is obtained for transport resistance on the external surface of ferrierite crystals, leading to distinct guest-molecule profiles in the inner part of the porous solid.

The same approach was used by Tzoulaki et al. to investigate the adsorption and desorption of isobutane in coffin-shaped MFI-zeolite-type crystals.[42] Figure 19 shows transient concentration profiles observed during isobutane uptake and release. Figure 19a illustrates the distribution of the isobutane concentration within the crystal after 10 s of isobutane adsorption, while Figure 19b presents profiles of the concentration

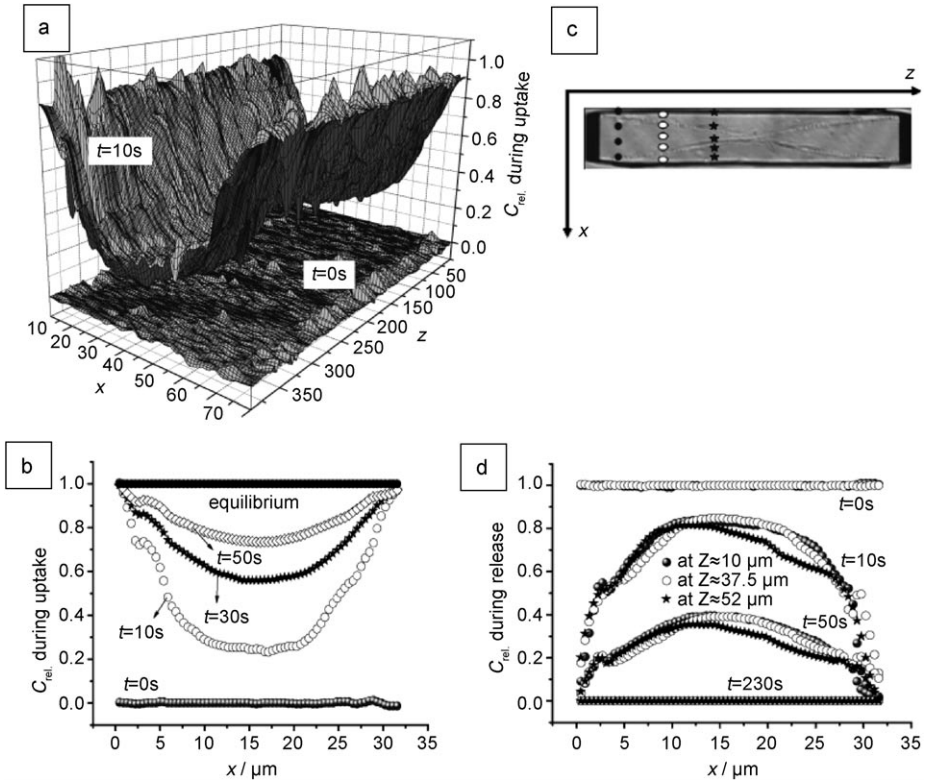

Figure 19. Time-dependent concentration profiles of isobutane as a guest molecule on a silicalite-1 crystal: a) 2D concentration profile 10 s after the onset of isobutane adsorption. b) Evolution of the concentration profile of isobutane along the *x* axis at $z = 10$ μm during uptake. c) Silicalite-1 crystal indicating the positions *z* of the concentration profiles in (d). d) Evolution of the concentration profiles of isobutane along the *x* axis during release at different *z* values. Reproduced from reference [42].

integrals along the crystal x direction. Finally, Figure 19d provides a comparison of the profiles during desorption along the x axis during release at different z values. It is clear that the isobutane uptake is essentially independent of the z position in the zeolite crystal. More importantly, in both the adsorption and desorption experiments, the boundary concentrations are found to assume the equilibrium values instantaneously. This result is different from that obtained for ferrierite and indicates that there is no additional transport resistance or surface barrier on the outer crystal surface. In the case of MFI-type crystallites, the observed surface diffusion barriers are probably amorphous silica layers on the external surface of the crystals. Therefore, prior to calcination and use, the crystallites were exposed to a dilute NaOH solution. During this alkaline treatment, thin amorphous silica layers easily dissolve, yielding seemingly surface-barrier-free crystallites. However, the work of Kortunov et al. illustrated that surface barriers could exist in MFI-type crystals.[43] By comparing the adsorption and desorption behavior of isobutane for two different ZSM-5 crystals, only one of which was etched, crystal surface defects were found to either increase or decrease the rate of adsorption and desorption. The former effect could be associated with adsorption and desorption through cracks in the crystal surface, while the latter is due to blockage or structural change of the external crystal surface, leading to surface transport barriers. Furthermore, MFI-type crystals may contain intracrystalline diffusion barriers as well as external surface barriers. Indeed, for isobutane adsorption and desorption experiments complemented with Monte Carlo simulations, Geier et al. have been able to demonstrate that the internal intergrowth sections of MFI-type crystals do not act as molecular highways to the outer crystal surface.[44] Instead, the measured and simulated time-dependent isobutane profiles provided strong evidence for the adsorption and desorption of isobutane through the outer crystal surface, while the internal surfaces serve only as mild surface barriers, retarding the transport of isobutane.

Further evidence for the compartmentalization of coffin-shaped ZSM-5 crystals and their related internal surface barriers was obtained by Roeffaers et al. using confocal fluorescence microscopy.[45,46] The liquid-phase acid-catalyzed self-condensation of furfuryl alcohol in dioxane was used as a reporter reaction for imaging the catalytic activity of ZSM-5 crystals (Scheme 1). This reaction requires not only diffusion but also the availability of Brønsted acid sites. Two furfuryl alcohol molecules initially produce a colorless bis-(furfuryl)methyl group. This molecule easily transfers a hydride ion to a primary carbenium ion formed from another molecule of furfuryl alcohol. Visible absorption then arises from the resonance-stabilized bis(furyl) carbenium ion (compound **A**, Scheme 1) or its conjugated analogue (compound **B**, Scheme 1) formed by proton loss. Excitation with visible light leads to fluorescence of compounds **A** and **B** and their related structures. The degree of oligomerization and conjugation may increase, thus shifting the absorption and emission wavelengths of the formed chromophores towards the red. Using confocal fluorescence microscopy, it was possible to locate in 3D the emissive reaction products formed within the zeolite crystals. Some results are shown in Figure 20a–c, which clearly indicates that product formation is space- and time-dependent. For a ZSM-5 crystal lying on the (010) face, the optical path runs along the (100) face, and the accumulated fluorescence on this face causes a bright rim after 10 min of reaction (Figure 20a). The spatial resolution of confocal fluorescence microscopy is sufficiently high to monitor in detail the fluorescence intensity at any point in the ZSM-5 crystal. By depth profiling through the crystal or measuring line scans at different positions parallel to the (100) plane, it is possible to detect the relative intensity of the fluorescent reaction products. Clearly, a rim of fluorescent molecules is formed in the ZSM-5 crystals. After 16 h, the fluorescence also spreads along the long axis of the crystal into the crystal edges, as illustrated by the longitudinal scans in Figure 20b. It seems that any zone in the crystal can be reached by the furfuryl alcohol molecules. Interestingly, after 50 days of catalytic reaction, a reversed situation is observed, and the tip segments emit the most intense fluorescence. It has been argued that at such long reaction times the microporous zeolite catalysts tend to be deactivated by pore plugging. Clearly, the desorption of product molecules from the edge segments is slow and gives rise to extensive consecutive reactions, such as oligomerization. This result is in line with internal intergrowth interface boundaries, which function as diffusion barriers that retard fast product diffusion.

The hydrothermal synthesis of zeolites usually requires the use of template molecules to ensure their long-range order structure; it is possible to remove these molecules by calcination. The thermal decomposition of template molecules leads to the formation of light-absorbing and light-emitting species. The latter, most probably conjugated aromatic compounds formed from the decomposition of charged amines, can be visualized in space and time using confocal fluorescence microscopy. As the accessibility of the porous network in the subunits varies owing to the presence of internal transport barriers for molecular diffusion, the individual building blocks of large zeolite crystals can be

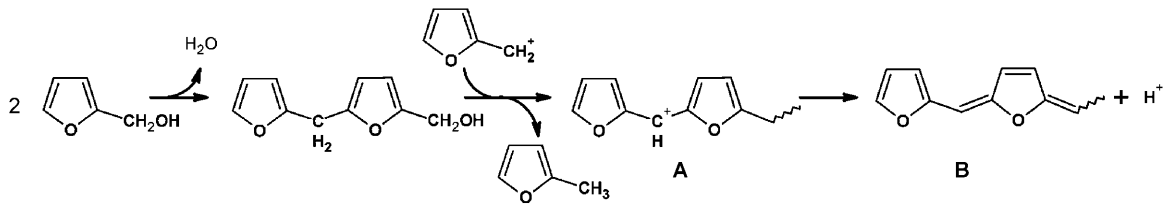

Scheme 1. Acid-catalyzed self-condensation reaction of furfuryl alcohol.

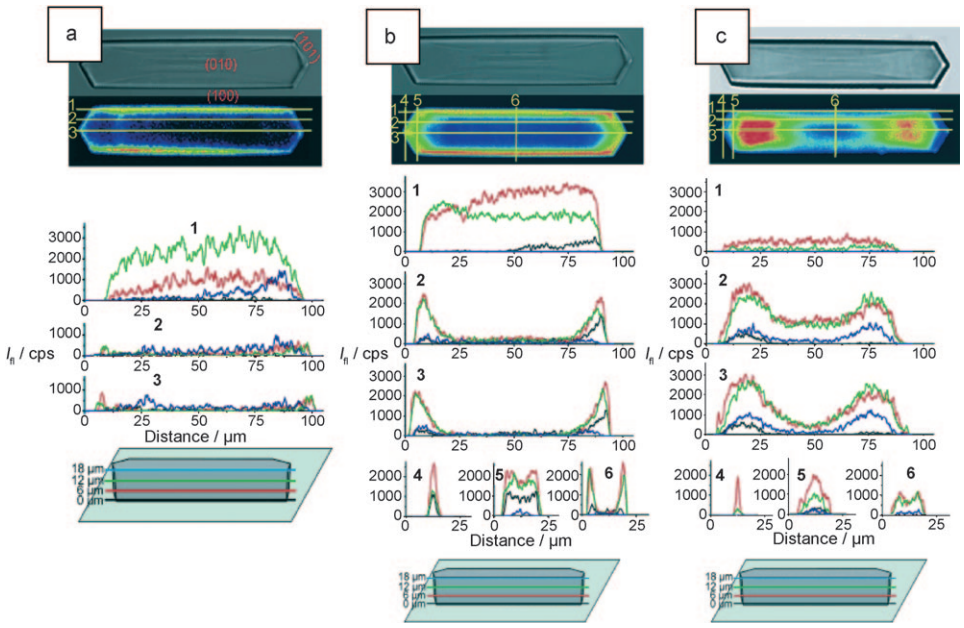

Figure 20. Confocal fluorescence imaging of the condensation of furfuryl alcohol catalyzed by an individual H-ZSM-5 zeolite crystal after a) 10 min, b) 16 h, and c) 50 days of reaction, together with the corresponding optical transmission images (grayscale) for different cross-sections and depth profiles throughout the H-ZSM-5 crystal. Reproduced from reference [45].

visualized by monitoring the template removal process in time. This approach was developed by Karwacki et al. and used to reveal the intergrowth structure and related diffusion boundaries for the structure types CHA (SAPO-34), AFI (SAPO-5 and CrAPO-5), and MFI (ZSM-5).[47] For ZSM-5 crystals a gradual hour-glass pattern could be revealed by performing depth scanning through the zeolite crystal; different subunits could also be discerned, the number and shape of which depended on the morphology of the zeolite crystal.

Seebacher et al. used 4-(4-diethylaminostyryl)-1-methylpyridinium iodide and oxazine-1 (Scheme 2) as probe molecules for studying penetration into the porous networks of large ZSM-5 and $AlPO_4$-5 molecular sieves.[48] Before calcination of the molecular sieves and after immersion into the dye solution, no fluorescence could be detected within the solids by confocal fluorescence microscopy. This result is no surprise, as the dye molecules are too big to enter the micropore systems of these two molecular sieves. Instead, for the calcined materials both dyes can diffuse into the inner part of the crystals. In all cases, a rather complex and inhomogeneous band structure of fluorescence along the crystal length could be observed, which was explained by the authors in terms of the formation of internal defects in the zeolite structure. The same 4-(4-diethylaminostyryl)-1-methylpyridinium iodide molecule was used by Roeffaers et al. to study a series of large ZSM-5 crystals to gain detailed insight into the intergrowth structures of these zeolites.[49] The adsorption of this probe molecule has been linked to the visualization of straight pores within the ZSM-5 structure, and for properly treated crystals it is argued that there are no mesopores intruding into the crystallites. As shown by Seebacher et al.,[48] mesopores could host these 4-(4-diethylaminostyryl)-1-methylpyridinium iodide molecules.

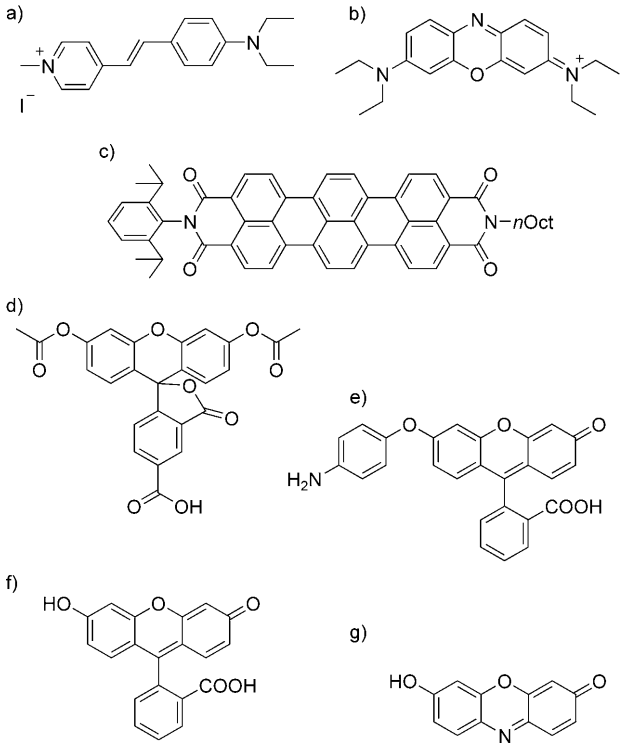

Scheme 2. Molecular structures of a) 4-(4-diethylaminostyryl)-1-methylpyridinium iodide, b) oxazine-1, c) terrylene diimide, d) 5-carboxyfluorescein diacetate, e) aminophenyl fluorescein, f) fluorescein, and g) resorufin.

2.3.2. *Pore Alignment, Shape Selectivity, and Reactivity Patterns within Zeolite Crystals as Probed with a Combination of UV/Vis, Fluorescence, and Infrared Microscopy*

Kox et al.[50] and Stavitski et al.[51,52] investigated large coffin-shaped ZSM-5 crystals utilizing a combination of three in situ microscopic techniques: UV/Vis, fluorescence, and IR. Acid-catalyzed styrene oligomerization was chosen as a probe reaction for assessing the Brønsted acidity in a space- and time-resolved manner (Scheme 3). The cationic intermediates in the styrene oligomerization reaction, which exhibit strong optical, vibrational, and fluorescence spectra upon photoexcitation, can act as reporter molecules for catalytic activity. H-ZSM-5 crystals exposed to 4-methoxystyrene were heated in the in situ cell, and microscopy images as well as optical spectra were recorded. The crystals turn purple upon heating; however, closer examination reveals that the edges and the main body of the crystal exhibit different colors (Figure 21 a).

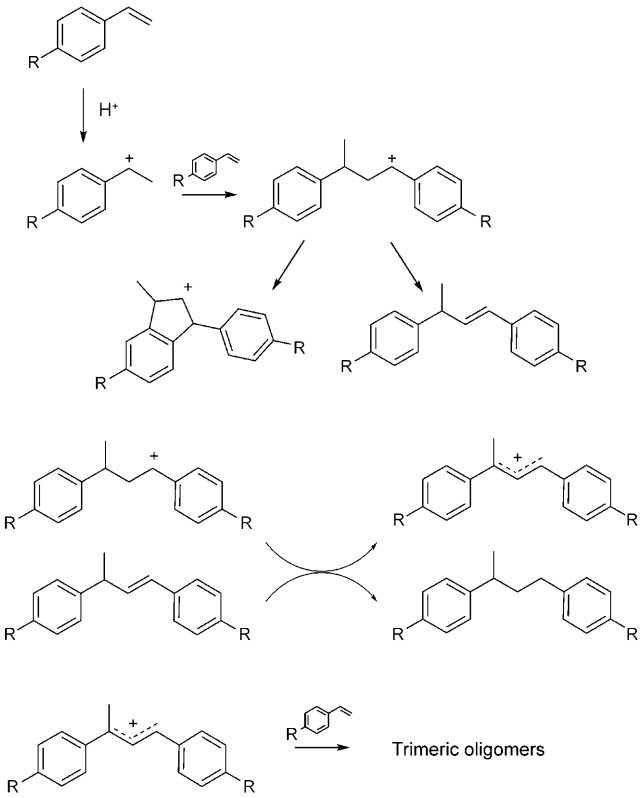

Scheme 3. Acid-catalyzed oligomerization of styrene.

As is apparent from the optical spectra in Figure 21b, two bands at approximately 590 and 635 nm are present in both parts of the crystal with different intensity ratios. In accordance with the reaction pathway in Scheme 3, the absorption band at 590 nm is due to a dimeric allylic carbocation, while the band at 635 nm can be assigned to a trimeric carbocation. It is evident that different parts of the crystal vary in their catalytic behavior. To better understand the nonuniform catalytic properties of the H-ZSM-5 crystal, deeper insight into its microscopic structure is required. H-ZSM-5 has the MFI crystalline structure with a pore system consisting of intersecting elliptical 5.3×5.1 Å^2 straight pores and 5.6×5.3 Å^2 zigzag pores. Large MFI crystals consist of different intergrown single-crystalline subunits, which are rotated by 90° about the common crystallographic [001] axis (Figure 21c,d). Further experimental evidence for this intergrowth structure could be obtained using a combination of electron back-scatter diffraction (EBSD) and focused ion-beam (FIB) milling experiments.[53] As the oligomerization reaction is likely to occur within the zeolite channels, the carbocations would be expected to be entrapped and aligned within the pores. Such an alignment may be revealed using optical absorption measurements with polarized light, as the photoactive molecules absorb light polarized parallel to their dipole moment vector. Microphotographs taken with unpolarized and polarized light (Figure 21a,e) show that the body of the crystal (an upper surface of the smaller subunit) remains translucent when the polarization is parallel to the crystal long axis but is strongly colored when the polarizer is directed otherwise. This finding directly implies that in this region the carbocations are aligned with the straight channels. At the edges of the crystal, the absorbance does not change dramatically upon rotation of the polarizer (Figure 21e), thus indicating that the preferred molecule orientation is collinear with the incident light. The intergrowth structure suggests that at the edge regions straight pores, which accommodate the intermediate molecules, are opened directly to the outer surface, while in the main body they run parallel to the surface and are accessible through the sections of zigzag pores. On the basis of this information it can be concluded that at the crystal edges the carbocation dimer is trapped within the straight pore near the surface, thus blocking further access of monomers and suppressing the formation of higher oligomers. In the crystal body, even after the dimer has been formed in the straight channel, more monomer molecules can diffuse through the sections of the adjacent zigzag pores.

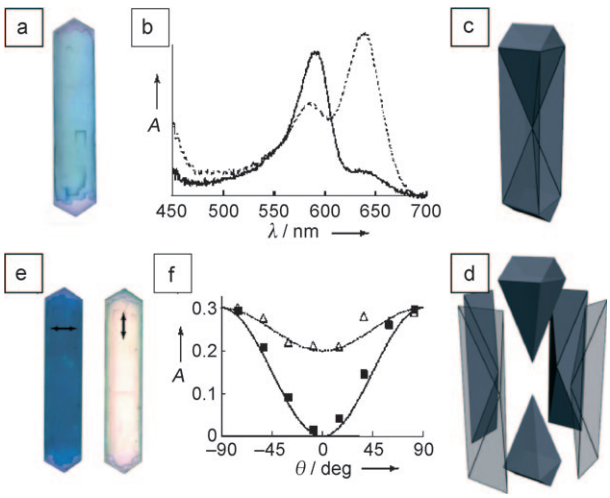

Figure 21. a) Optical microphotograph of a H-ZSM-5 crystal after addition of 4-methoxystyrene, showing the different colors of the body (blue) and the edges (purple). b) Spatially resolved optical absorption spectra measured along the long axis of the crystal after reaction at the edges (solid line) and the center (dotted line); c,d) Three-dimensional model of the intergrowth structure of an individual H-ZSM-5 crystal. e) Microphotographs of H-ZSM-5 exposed to 4-methoxystyrene and measured with polarized light (polarization is indicated by arrows). f) Angular dependence of the optical absorption at 590 nm in the body (squares) and at the edges (triangles) of the crystal. Reproduced from reference [50].

In an extension of the studies of the H-ZSM-5/4-methoxystyrene system, the factors influencing catalytic activity and selectivity were investigated using styrene derivatives bearing different substituent groups.[51] To this end, a series of large H-ZSM-5 crystals was loaded with different styrene derivatives. After reaction, the zeolite crystals exhibited colors ranging from yellow-brown through blue to pink-purple (Figure 22a). In all cases that led to catalytic reactivity, a nonuniform coloration was observed. Two factors account for the observed differences. Firstly, very bulky heavily substituted styrene molecules are not able to diffuse into the pores of the zeolite, resulting in translucent zeolite crystals. Secondly, the stability of the initial styrene carbocation determines the reactivity within the pore channels. In the case of 4-chlorostyrene, the position of the electron-withdrawing

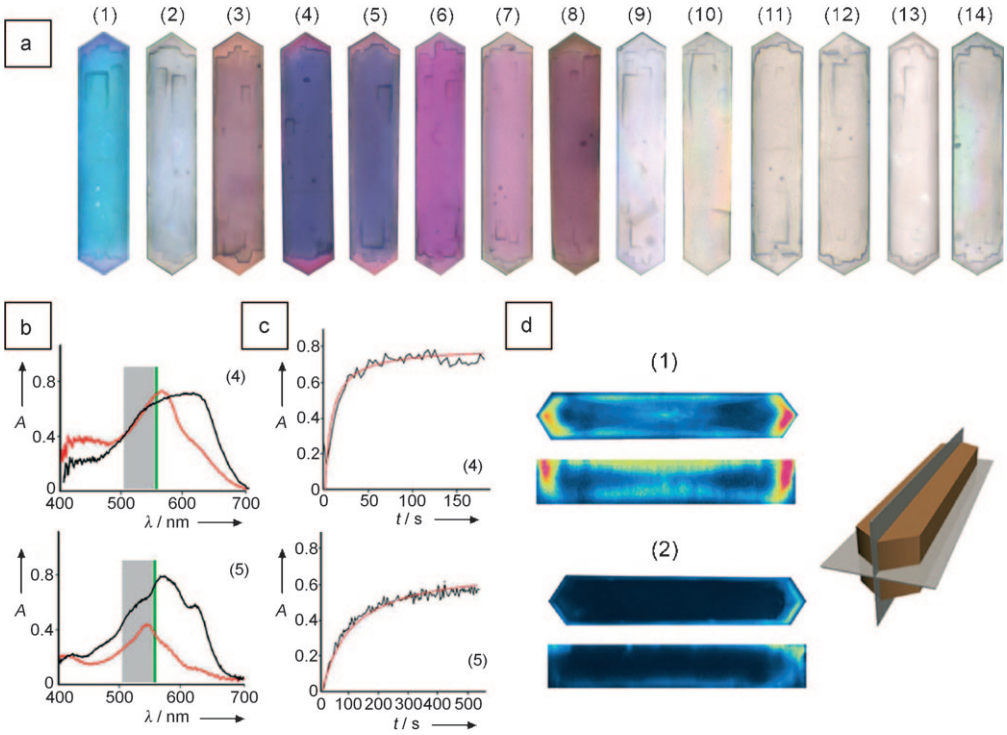

Figure 22. a) Optical microphotographs of the H-ZSM-5 crystals after styrene oligomerization with 14 different styrene derivatives (1: 4-methoxystyrene; 2: 4-ethoxystyrene; 3: 4-methylstyrene; 4: 4-bromostyrene; 5: 4-chlorostyrene; 6: 4-fluorostyrene; 7: β-methoxystyrene; 8: *trans*-β-methylstyrene; 9: 3-chlorostyrene; 10: 2,3,4,5,6-pentafluorostyrene; 11: α-methylstyrene; 12: 3-trifluoromethylstyrene; 13: 3,4-dichlorostyrene; 14: 2,6-dichlorostyrene). b) Optical absorption spectra of the H-ZSM-5 crystals after reaction with 4-bromostyrene (4) and 4-chlorostyrene (5) at 100 °C taken at the main body (black) and edges (red) of the crystal. The gray areas indicate the excitation wavelength range used in the fluorescence microscopy experiments (510–560 nm). The green bar indicates the laser wavelength in the confocal fluorescence measurements (561 nm). c) Time evolution of the optical absorption band assigned to the dimeric carbocation for 4-bromostyrene (4) and 4-chlorostyrene (5). d) Confocal microscopic images of H-ZSM-5 zeolite crystals measured in the spectroscopic cell after oligomerization of 4-methoxystyrene (1) and 4-ethoxystyrene (2). Two cross-sections are shown, as indicated in the corresponding 3D model. Reproduced from reference [51].

halogen atom on the aromatic ring destabilizes the carbocation. In contrast, when the chlorine atom is placed at the *meta*-position, it destabilizes the initial styrene carbocation, and no reactivity is detected for 3-chlorostyrene. The nonuniform coloration arising from the intensity variations of different absorption bands is illustrated in Figure 22b. For all styrene molecules investigated, one absorption band (assigned to the dimeric carbocations) dominates the edge spectra, while in the center other bands at longer wavelength appear, attributed to species undergoing further oligomerization. To gain more insight into the oligomerization kinetics for each of the styrene compounds, Stavitski et al. performed time-resolved experiments.[51] From these data, reaction rate constants for the different reactive styrene compounds were obtained by fitting kinetic profiles with a second-order rate equation (Figure 22c). These reaction rate constants have been rationalized in terms of the stabilization of the initial styrene carbocation. The diffusion properties of the styrene molecules also influence the catalytic activity, as can be seen from the comparison of the reactivity of 4-methoxystyrene and 4-ethoxystyrene. The 3D volume reconstructions of the confocal fluorescence measurements for 4-methoxystyrene and 4-ethoxystyrene (Figure 22d) show that in the former case the oligomerization reaction occurs in nearly the entire volume of the crystal, while in the latter only a thin near-surface layer of the zeolite crystal is affected. Clearly, internal surface boundaries can be observed.

UV/Vis and fluorescence microscopy methods have been very powerful in the spatially resolved visualization of catalytic activity within zeolite crystals. However, extra measures are required to unambiguously unravel the chemical nature of the species formed during reaction. This could be accomplished with IR microscopy using synchrotron radiation.[52] H-ZSM-5 crystals were exposed to 4-fluorostyrene; corresponding IR spectra from a region in the center of the crystal are given in Figure 23a. Two sharp features, at 1534 cm^{-1} (with a shoulder at 1521 cm^{-1}) and 1510 cm^{-1}, are visible in the spectrum. The broad bands (1600–1700 and 1000–1300 cm^{-1}) are attributed to the harmonics of the zeolite framework. By comparing the IR spectrum with that of 4-fluorostyrene (Figure 23a), the band at 1510 cm^{-1} is found to coincide with that of the reactant. When the spectra are recorded in situ during the reaction (Figure 23b) at 100 °C, the intensity of the 4-fluorostyrene band decreases, while the band near 1534 cm^{-1} and corresponding to oligomeric styrene species increases in intensity. As the synchrotron IR radiation is intrinsically polarized, polarization experiments can be performed. Figure 23c shows IR spectra recorded with light polarized parallel and perpendicular to the long crystal axis. The intensity of the 1534 cm^{-1} band depends upon IR light

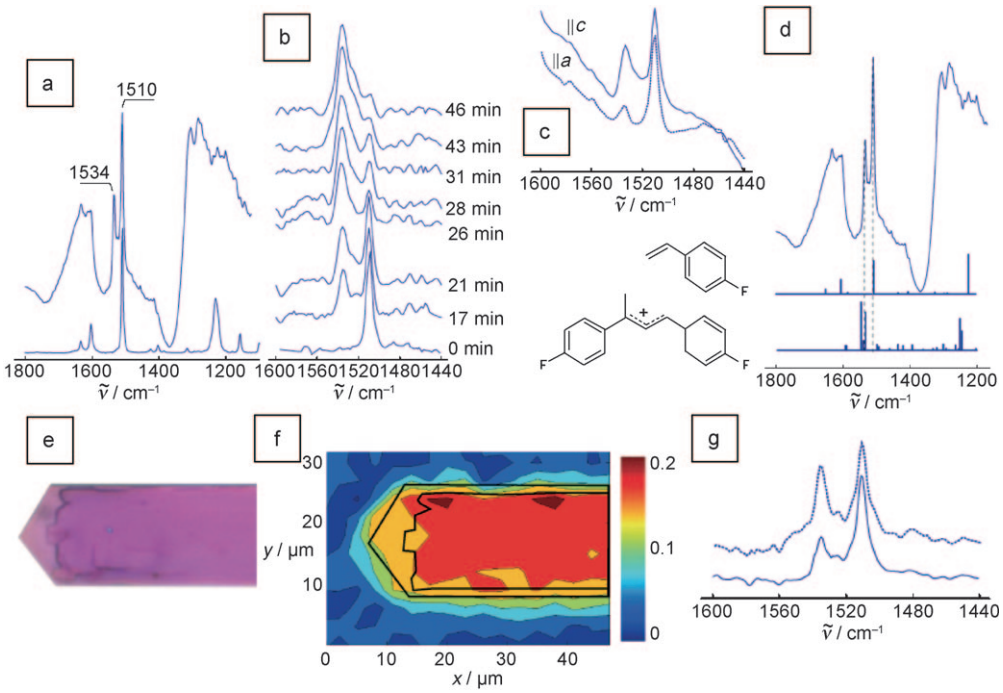

Figure 23. a) IR spectra of an individual H-ZSM-5 crystal in contact with 4-fluorostyrene (top) and of liquid 4-fluorostyrene (bottom). b) IR spectra (1440–1600 cm^{-1}) recorded during the 4-fluorostyrene oligomerization reaction as a function of reaction time. The spectra are background-corrected. c) IR spectra taken with light polarized parallel to the long (|| *c*) and short (|| *a*) crystal axes. d) Experimental and calculated spectra for 4-fluorostyrene and the related dimeric reaction product. e) A fragment of the optical microphotograph of the ZSM-5 crystal after reaction with 4-fluorostyrene. f) 2D intensity map of the IR band at 1534 cm^{-1} across the H-ZSM-5 crystal. g) IR spectra recorded at the edge (solid line) and in the body (dotted line) of the crystal, demonstrating differences in the intensity ratios of the bands. Reproduced from reference [52].

polarization. The less significant intensity changes of the band at 1510 cm^{-1} can be explained by the smaller molecular dimensions of the styrene monomer, which allow for less strict molecular alignment in the pores. To confirm the assignment of the IR band at 1534 cm^{-1}, geometry optimizations and vibrational frequency calculations for the reagent and possible products were performed within the framework of density functional theory (DFT). The calculated vibrational spectrum of the 1,3-bis(4-fluorophenyl)-2-buten-1-ylium cation showed excellent agreement with experiment. Furthermore, the distribution of this reaction product could be mapped over the crystal by scanning the individual crystal under the IR microscope (Figure 23 f).

Kox et al.[54] extended this combined in situ microscopic approach to investigate the effect of mesoporosity in H-ZSM-5 zeolite crystals on their catalytic performance. Two samples were investigated: one contained pristine H-ZSM-5 crystals (Figure 24 a, denoted microporous), whereas the other had undergone an alkaline treatment, resulting in selective removal of silicon from the framework and formation of mesopores (Figure 24 b, denoted mesoporous). Confocal fluorescence measurements during the template removal process, as discussed above, allow visualization of the intergrowth structure of these boat-shaped ZSM-5 crystals and show three main building blocks (Figure 24 c–e). Comparison of the results for the parent and alkaline-treated zeolite crystals after addition of 4-methoxy- or 4-fluorostyrene and heat treatment at 100 °C show that microporous crystals are most colored in the upper lid, whereas the mesoporous crystals color predominantly at the outer parts of the crystal (Figure 24 f, g). In the mesoporous crystals, the localized attack of the base removes the upper part of the zeolite crystal and therefore facilitates mass transport inside the zeolite volume. In the microporous crystals, the upper part imposes a diffusion barrier, making diffusion of reactant molecules inside the zeolite more difficult. As in the case of coffin-shaped ZSM-5 crystals, optical absorption spectra of the microporous crystals show the presence of two absorption bands, at 595 and 650 nm for 4-methoxystyrene and at 560 and 600 nm for 4-chlorostyrene, which can be attributed to dimeric and trimeric species, respectively. The longer-wavelength absorption band in the microporous crystals vanishes completely when the oligomerization is carried out over the mesoporous zeolite, therefore showing that the formation of trimeric or higher carbocations is limited (Figure 24 h, i). In the microporous crystals, dimeric product molecules, formed on Brønsted acid sites in the micropores, may encounter other acid sites, leading to trimeric or higher oligomers. Furthermore, the influence of different styrene compounds with distinct reactivity on the fluorescence behavior was examined in a space-resolved manner, showing inhomogeneous Brønsted acidity. Confocal fluorescence images recorded after oligomerization with different styrene compounds show clear differences in the fluorescence patterns (Figure 24 j). The observed differences in coloration were rationalized by assuming that a gradient in Brønsted acidity is present owing to distinct Si/Al ratios in different parts of the crystals as a consequence of the desilication treatment. As a

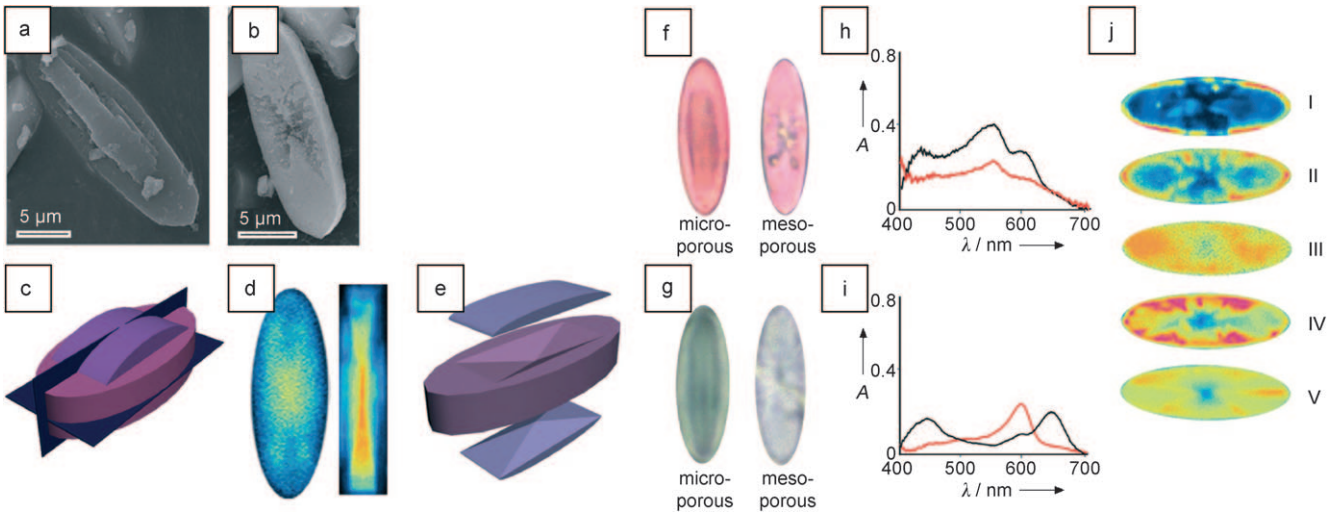

Figure 24. a, b) SEM images of the microporous (a) and mesoporous (b) H-ZSM-5 crystals. c) Model of microporous H-ZSM-5 crystals. d) Confocal fluorescence microphotographs taken from horizontal and vertical cross-sections as indicated in (c). e) Exploded representation of the individual building blocks of the H-ZSM-5 crystals. f, g) Microphotographs of the micro- and mesoporous crystals after oligomerization with 4-chlorostyrene (f) and 4-methoxystyrene (g). h, i) Optical absorption spectra for the microporous (black) and mesoporous (red) H-ZSM-5 crystals after oligomerization with 4-chlorostyrene (h) and 4-methoxystyrene (i). j) Confocal fluorescence images of horizontal cross-sections of the mesoporous crystals after oligomerization of 4-fluoro- (I), 4-chloro- (II), 4-ethoxy- (III), 4-bromo- (IV), and 4-methoxystyrene (V). Reproduced from reference [54].

result, very reactive styrene compounds such as 4-methoxystyrene and 4-bromostyrene show more evenly distributed fluorescence patterns, as they will react on both strong and weak Brønsted acid sites. On the contrary, styrene compounds such as 4-chloro- and 4-fluorostyrene, with more electronegative substituents, will only react on very strong Brønsted acid sites.

In a related study, Mores et al. used a combination of UV/Vis and fluorescence microscopy to study the formation of coke and its precursors in individual H-ZSM-5 and H-SAPO-34 crystals in a space- and time-resolved manner.[55] For this purpose, they used the methanol-to-olefin (MTO) process as a probe reaction. In H-ZSM-5, coke is initially formed at the crystal edge, and the coloration of the crystal intensifies with reaction temperature. Temporal profiles of the UV/Vis bands attributed to coke or its precursors reveal two distinct coke systems: methylated aromatic systems and graphitic coke compounds. The latter are responsible for blocking of the pore openings. Confocal fluorescence microscopy confirmed the preferred accumulation of coke at the crystal edges, whereas with time on stream a coke front composed of methylated aromatic systems moved towards the center of the H-ZSM-5 crystal. The internal intergrowth boundaries in H-ZSM-5 clearly hindered the facile transport of these more bulky aromatic compounds. In the case of H-SAPO-34, fast formation of methyl-substituted aromatic compounds at the corners and edges of the crystal is observed. Confocal fluorescence experiments confirmed the formation of fluorescent coke compounds starting at the corners of the H-SAPO-34 crystal; the majority of these species remain located at the edges of the crystal, thereby slowing down further coke formation in the crystal center.

2.4. Spatial Heterogeneities at the Level of Catalyst Nanoparticles and Single Molecules

2.4.1. Tracking the Diffusion Pattern of Single Molecules with Fluorescence Microscopy to Reveal Information on the Porosity and Accessibility of a Catalyst Material

Zurner et al.[56] and Jung et al.[57] studied in great detail the diffusion of single fluorescent dye molecules within a thin mesoporous hexagonal silica film by a combination of high-resolution transmission electron microscopy and fluorescence microscopy using the highly fluorescent terrylene diimide (TDI) dye molecule (Scheme 2). By careful overlaying of the fluorescence and electron microscopic images, the porous structure of the mesoporous silica film can be directly correlated with the diffusion dynamics of the TDI dye molecule. This method gave the first direct evidence that the molecular diffusion pathway through a porous material correlates with the pore orientation of the two-dimensional hexagonal mesoporous material. To enable this analysis, a special cell and an advanced synthesis procedure, including the addition of polystyrene beads and gold colloids to the mesoporous film, were developed.

Figure 25a shows a fluorescence image in which single TDI dye molecules appear with a characteristic fluorescence intensity profile. From the striped patterns it is possible to compute both the position of the dye molecule and the orientation of its transition dipole moment. It was concluded that the transition dipole moments of all TDI dye molecules have the same orientation over the whole image, which is indicative of domains of highly structured mesoporous material. Moreover, a sequence of consecutive images showed that the molecules remain immobile when the mesoporous film material was present in air (at 40% relative

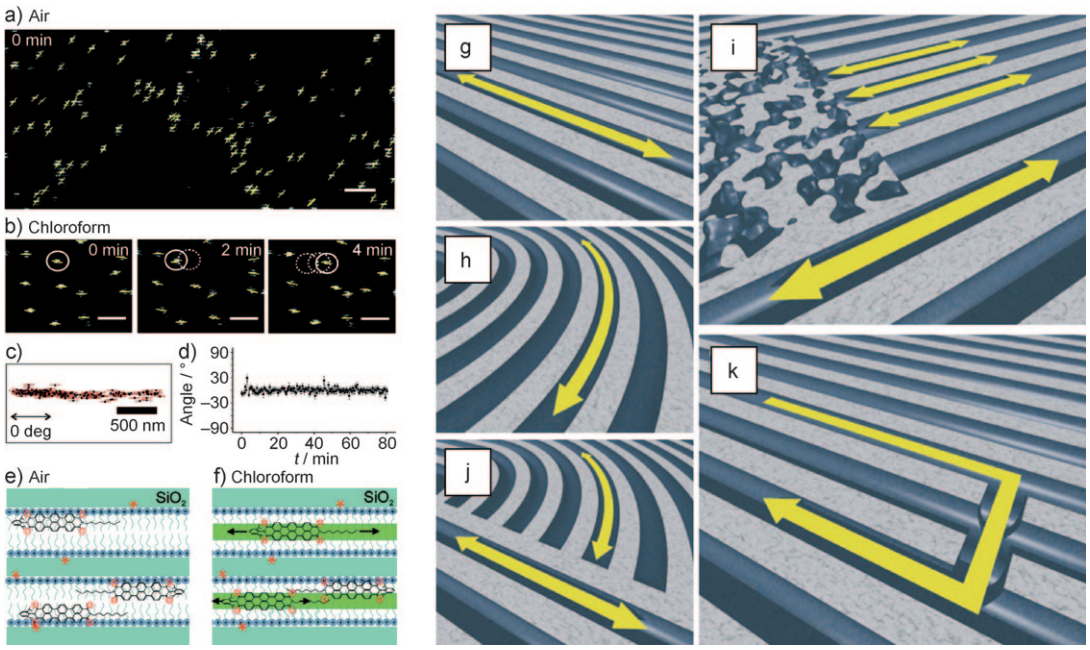

Figure 25. Orientation and diffusion of single terrylene diimide (TDI) molecules in highly structured domains of a mesoporous silica film: a) Single TDI molecules embedded in parallel pores in air atmosphere. The fluorescence image shows oriented TDI molecules (striped patterns). b) Sequence of fluorescence images showing linear diffusion of single TDI molecules in a chloroform atmosphere. c) The trajectory of the individual TDI molecule marked with a white circle in (b). d) Calculated angular time trajectory of the same TDI molecule. e) Schematic depiction of TDI molecules immobilized in the mesoporous material in air. f) View as in (e) but in chloroform atmosphere. The TDI molecules are solvated (green stripe) and diffuse along the channels; their walk is occasionally interrupted by adsorption events. g) Straight segment within mesoporous silica film. h) Curved segment. j) Domain boundary forcing molecules to turn back. i) Molecular travel stopped at less-ordered regions. k) Lateral motion between neighboring channels. Reproduced from references [56, 57], copyrights American Chemical Society, 2008, and Nature Publishing Group, 2007.

humidity). At higher humidity, the dye molecules diffuse very slowly.

High mobility of the TDI molecules could be achieved when the mesoporous film was exposed to a saturated chloroform atmosphere. The three fluorescence images in Figure 25 b were taken after 0, 2, and 4 min. Figure 25 c shows the trajectory of the single TDI molecule highlighted in Figure 25 b. Strikingly, when the chloroform atmosphere was replaced with air, the TDI molecules stopped moving. This finding clearly demonstrates that the diffusion of TDI molecules in the mesoporous film can be switched on and off reversibly by simply changing the environment surrounding the pore system. Figure 25 d shows the time evolution of the angle of the transition dipole moment of the TDI molecule. The angle was found to be nearly constant, and this remarkable alignment can only be the result of a tight fit of the TDI molecules within the mesoporous hexagonal channels with a diameter of 2–3 nm. Since the mesopores are still filled with template molecules, the effective volume available for the TDI molecules is even more restricted. Figure 25 e, f schematically illustrates the host environment of the TDI molecules in the presence of air and chloroform, respectively. The immobility of the TDI molecules in air is most probably caused by the interaction between TDI and the template molecules. Interactions also occur between TDI and active silanol groups and defect sites in the walls of the mesoporous channels. In contrast, when chloroform (a good solvent for TDI) is present, the small solvent molecules form a lubricant-like phase inside the pores. The TDI molecules are thus solvated within the mesopores, leading to rapid diffusion.

Following this experimental strategy, the trajectories of TDI molecules were measured with high spatial accuracy in various mesoporous environments, as shown schematically in Figure 25 g–k. More specifically, the diffusion of TDI molecules could be tracked within linear or strongly curved sections of the hexagonal film material (Figure 25 g, h). Figure 25 j illustrates how the TDI molecules slow down drastically or even bounce back at domain boundaries. Figure 25 i sketches the situation in which molecular transport of the TDI molecule stops when it reaches a region of less ordered material (dead ends), whereas Figure 25 k illustrates how a molecule can escape from its main channel through a bypass route to another main channel. In other words, the diffusion of a TDI molecule is an interrupted 1D random walk, owing to the presence of heterogeneities in mesoporous material and to the presence of adsorption sites in which the TDI molecules can be occasionally trapped.

In a related study, Kirstein et al.[58] demonstrated that the approach described above makes it possible to distinguish the diffusion of TDI molecules on the external surface from the diffusion of TDI molecules within the pore system. Diffusion in a lamellar mesoporous material appeared to be much slower than diffusion in a hexagonal mesoporous structure. It was even possible to track the transport of TDI molecules from one type of surroundings (the hexagonal channel system) to another (the lamellar channel system). Further-

more, Lebold et al. observed that the mobility of TDI molecules can increase or decrease depending on the functional groups attached to the mesoporous silica wall.[59] The authors explained their findings in terms of shielding of the hydroxy groups of the silica surface in combination with changes in the rigidity of the micellar packing in the silica film and directional interactions between the functional groups and the TDI molecules. In summary, single-molecule detection of dye molecules in porous structures reveals a wealth of information about the topology, nanoscale connectivity, and accessibility of the channels of a porous catalyst material.

2.4.2. *Monitoring Base-Catalyzed and Bromination Reactions with Single-Molecule Fluorescence Microscopy in an Individual Layered Double Hydroxide Catalyst Crystal*

Roeffaers et al. investigated base-catalyzed reactions over individual layered double hydroxide (LDH) crystals of size 10–20 μm using fluorescence microscopy.[60] They studied two distinct catalytic reactions, the hydrolysis and the transesterification of 5-carboxyfluorescein diacetate (C-FDA, Scheme 2), to distinguish different active-site populations in an LDH catalyst particle. Their approach is schematically illustrated in Figure 26a. C-FDA molecules become emissive only upon hydrolysis or transesterification, for example with 1-butanol. By exposing the LDH crystals to solutions of C-FDA, bright fluorescent spots are observed, which are due to the formation of individual product molecules. Photobleaching causes rapid disappearance of the fluorescent spots, allowing the continuous detection of catalytic activity in different region of the LDH crystals and yielding space-resolved information on their reactivity.

Previous characterization studies indicated that the activity of LDH catalysts is not uniform and that most active sites are probably located at the edges and corners of the crystals. Figure 26a schematically illustrates the catalytic sites located at the {0001} basal surface of an LDH crystal and OH^- ions at the $\{10\bar{1}0\}$ faces, which appear in the microscopic images at the edge of the LDH crystal. For the transesterification reaction of C-FDA with 1-butanol, the spots appear all over the basal surface without any preference for the crystal edges (Figure 26b,c). Since no fluorescence signal was observed in the solution surrounding the LDH crystal, it can be concluded that the transesterification reaction is catalyzed by the LDH material only. Instead, when the alcohol solvent in the ester hydrolysis reaction was replaced by aqueous solution, the fluorescent spots primarily occurred at the crystal edges, and there were fewer at the basal surface (Figure 26d,e). By carefully analyzing their set of data, Roeffaers et al.[60] concluded that the catalytic activity of LDH materials is not always associated with the same type of active sites; that is, the transesterification reaction primarily occurs at the {0001} plane, whereas the hydrolysis reaction requires the $\{10\bar{1}0\}$ faces, where exchanged OH^- ions at the entrance of the LDH galleries may be the active sites.

Furthermore, time-dependent experiments allowed determination of the reaction rate for both catalytic reactions. In the case of the transesterification reaction of C-FDA with 1-butanol, a typical rate of 7.2×10^{-13} mol m^{-2} s^{-1} was found, in agreement with transesterification rates measured for bulk LDH samples. For the hydrolysis reaction of C-FDA in water on an LDH catalyst particle, two active-site populations could be discerned. Fluorescent spots formed on the {1010} faces of the crystals correspond to at least 85% of the overall activity, with an average rate of about 4.7×10^{-12} mol m^{-2} s^{-1}. The remaining hydrolysis activity, originating from the {0001} plane of the LDH crystals, has a rate of only 1.7×10^{-13} mol m^{-2} s^{-1}. In other words, this single-molecule study illustrates that the counting of single reaction turnovers allows quantification of the heterogeneity of reaction kinetics at the level of individual crystal faces.

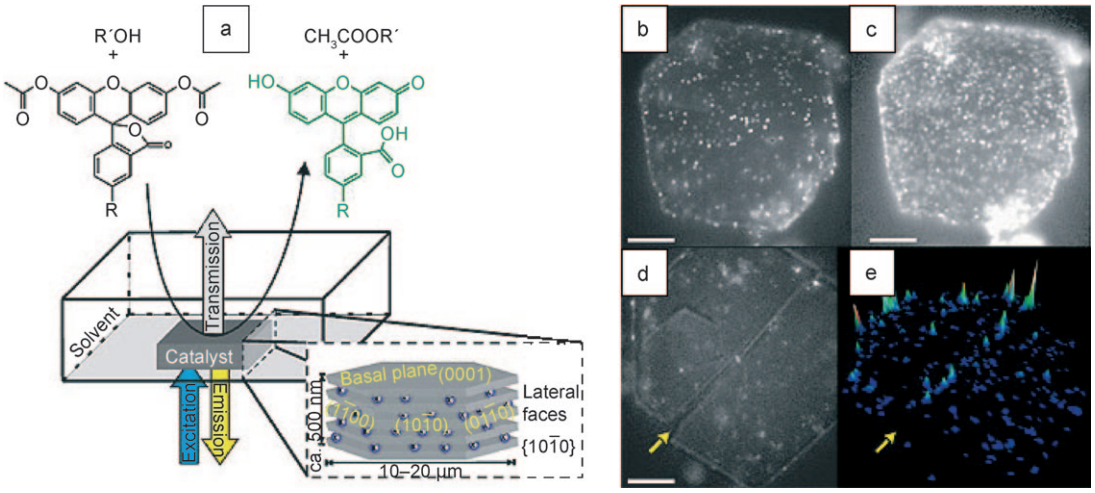

Figure 26. a) Schematic drawing of the experimental setup used to measure single catalytic turnovers during the transformation of fluorescein ester over an individual layered double hydroxide (LDH) particle using fluorescence microscopy. R = H for FDA and R = COOH for C-FDA. b,c) 2D fluorescence images of the transesterification of C-FDA with 1-butanol at 40 and 700 nM ester concentration, respectively, on the same LDH particle. d) 2D fluorescence image of the hydrolysis of 600 nM C-FDA on an LDH crystal, showing the formation of single product molecules mainly at the crystal edges. e) Accumulated spot intensity on the same crystal over 256 consecutive images. Reproduced from reference [60], copyright Nature Publishing Group, 2006.

In a related study, Martinez et al. explored single-molecule events in an individual LDH crystal ion-exchanged with WO_4^{2-}, which can be considered as an inorganic haloperoxidase mimic.[61] The catalytic material was evaluated for the generation of hypobromite (HOBr) from bromide and H_2O_2, which can brominate organic compounds or decomposes H_2O_2 into singlet O_2 and water. HOBr is expected to migrate into the reaction medium, where it performs the bromination reaction. By introducing the nonfluorescent fluorescein derivative aminophenyl fluorescein (APF, Scheme 2), it was possible to localize the bromination of APF. APF reacts with high rate and specificity with HOBr to form the strongly emissive fluorescein (Scheme 2), which can then be readily detected with fluorescence microscopy. By applying this approach, the authors were able to provide experimental evidence that HOBr performs reactions in the bulk solution surrounding an individual WO_4^{2-}–LDH crystal, as fluorescein formation could be observed at distances more than 800 nm from the edge of the individual LDH crystal.

2.4.3. *Single-Molecule Visualization of Redox Catalysis and Photocatalysis with Fluorescence Microscopy*

Xu et al.[62] studied the single-molecule turnovers of nonfluorescent resazurin to its fluorescent derivative resorufin (Scheme 2) by the addition of NH_2OH over spherical colloidal gold nanoparticles. For this purpose, individual Au nanoparticles about 6 nm in size were immobilized on an amine-functionalized glass surface and studied with total internal reflection fluorescence microscopy (TIRFM). Their experimental approach and some of the results obtained are shown in Figure 27. Movies of stochastic fluorescence bursts were measured at many localized spots on the coated glass surface (see single frame in Figure 27b); a typical time trajectory of the fluorescence intensity from one of these spots is given in Figure 27c. It can be concluded that the fluorescent spots display stochastic off–on signals that span the entire movie. The digital nature of the trajectory and the consistent height of the on level indicate that each fluorescent burst originates from a single resorufin molecule, which results from catalytic turnover by a single Au nanoparticle.

Although the actual events of catalytic product formation or product dissociation appear as instantaneous intensity jumps in the fluorescence trajectories with the millisecond time resolution used, the time needed for substrate diffusion, binding, or thermal activation before such an event (the "waiting time") is much longer. This phenomenon is illustrated in Figure 27c.The τ_{off} and τ_{on} are the two waiting times in these single-turnover fluorescence trajectories. Resolving them could allow the kinetic mechanism of the catalysis process to be probed in two parts; that is, τ_{off} is the waiting time before each instance of resorufin formation, while τ_{on} is the waiting time for resorufin dissociation after its formation. Their individual values are stochastic, but their statistical properties, such as average values and distributions, are well defined by the underlying reaction kinetics. Statistically, $\langle\tau_{off}\rangle^{-1}$ and $\langle\tau_{on}\rangle^{-1}$ represent the time-averaged single-particle rates of product formation and product dissociation, respectively. When averaged over the turnover trajectories from many Au nanoparticles, $\langle\tau_{off}\rangle^{-1}$ (the catalytic product formation rate) is expectedly dependent on the resazurin concentration (denoted [S] below) and exhibits saturation kinetics. Interestingly, a different behavior is observed for $\langle\tau_{on}\rangle^{-1}$ (the production dissociation rate), which also shows [S]-dependent kinetics, thus indicating that the substrate participates in production dissociation.

The [S] dependence of the production formation rate $\langle\tau_{off}\rangle^{-1}$ can be described by a Langmuir–Hinshelwood mech-

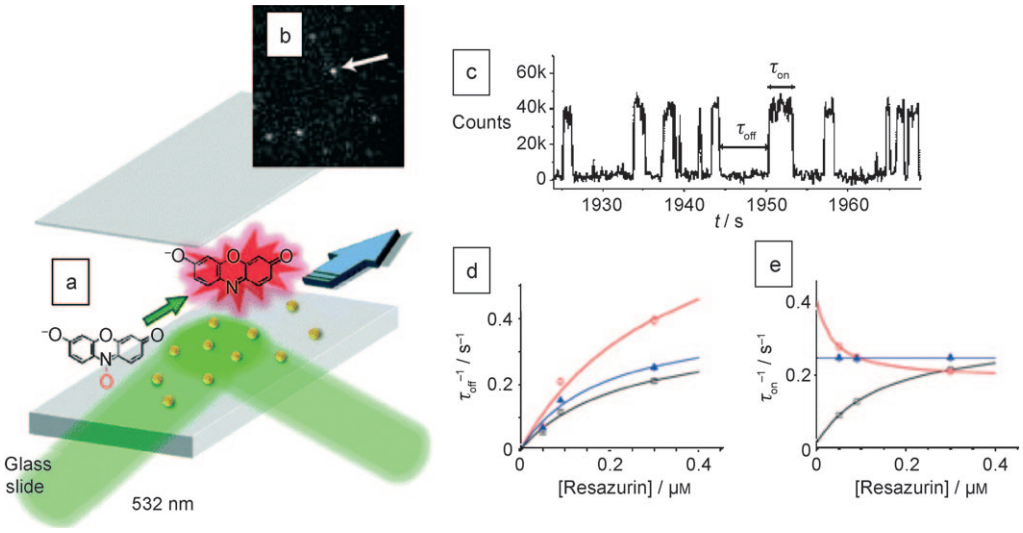

Figure 27. Single-turnover detection of single Au nanoparticle catalysis: a) Schematic drawing of the experimental setup based on total internal reflection fluorescence microscopy. b) Typical image of fluorescent products during catalysis taken at 100 ms per frame. The pixel size is about 270 nm, which results in the pixilated fluorescence spots. c) A segment of the fluorescence trajectory from the fluorescence spot marked by the arrow in (b) at 0.05 M resazurin and 1 mM NH_2OH. d) Dependence of $\langle\tau_{off}\rangle^{-1}$ on resazurin concentration. e) Dependence of $\langle\tau_{on}\rangle^{-1}$ on resazurin concentration. The red, blue, and black curves correspond to three exemplary Au nanoparticles. Reproduced from reference [62], copyright Nature Publishing Group, 2008 and Royal Society of Chemistry, 2009.

anism, in which the nanoparticle catalyzes the substrate conversion to the product while maintaining a fast substrate adsorption equilibrium. However, the catalytic product formation rates $\langle\tau_{off}\rangle^{-1}$ from individual nanoparticles reveal distinct saturation levels and initial slopes with increasing [S] (Figure 27d). Furthermore, the product dissociation rates $\langle\tau_{on}\rangle^{-1}$ from individual nanoparticles show three types of [S] dependence (Figure 27e). More specifically, 66% of the Au nanoparticles showed asymptotic increase in $\langle\tau_{on}\rangle^{-1}$ with increasing [S], which indicates that the nanoparticles prefer the substrate-assisted dissociation pathway. In addition, 19% of the Au nanoparticles show asymptotic decrease in $\langle\tau_{on}\rangle^{-1}$ with increasing [S], which indicates that the nanoparticles prefer the direct dissociation pathway. Finally, the remaining 15% of the nanoparticles have constant $\langle\tau_{on}\rangle^{-1}$ at any [S] concentration under study. These three different subpopulations fully reflect the heterogeneous nature of the catalytic process and more specifically the multiple dissociation reaction pathways with distinct kinetics.

In another study, Naito et al. investigated the photocatalytic activity of individual porous TiO_2 nanotubes by the single-molecule counting of OH radicals using a specific fluorescent probe.[63] For this purpose, a special setup was built making use of TIRFM. The TiO_2 nanotubes under study contained straight macropores with mesopores between the anatase nanoparticles. The photocatalytic activity of the porous structure was evaluated by the single-molecule counting of hydroxyl radicals (•OH) using APF (Scheme 2). The •OH in the photocatalytic reaction can be generated by the reduction or photodecomposition of H_2O_2, which is formed by reduction of O_2 by the conduction band or trapped electrons in TiO_2. The TiO_2 nanotube placed in the sample chamber is completely irradiated with UV light, and 488 nm evanescent light produced by a CW Ar^+ laser is used to excite fluorescein (Scheme 2), which is catalytically generated from APF. Time- and space-resolved observation of the photocatalytically generated fluorescein molecules clearly revealed that the transport of reagents inherent in the porous structures is closely related to the photocatalytic activity. Furthermore, the researchers were able to reveal spatial heterogeneity of reactive sites in an isolated TiO_2 nanotube.

2.4.4. Chemical Mapping of the Fischer–Tropsch Catalytic Process at the Nanoscale with Scanning Transmission X-ray Microscopy

De Smit et al. used STXM to monitor phase changes in an iron-based Fischer–Tropsch catalyst as well as to reveal details of the nature and location of carbon species produced during catalytic reaction.[64] In Fischer–Tropsch synthesis (FTS), synthesis gas (a mixture of CO and H_2) is converted into hydrocarbon chains through a surface polymerization reaction. The iron-based catalyst in question consists of iron oxide dispersed on SiO_2, with copper oxide and potassium oxide to improve its performance. The main experimental challenge in using in situ STXM is to overcome the strong attenuation of soft X-rays by matter. For this purpose, a special nanoreactor originally developed for in situ TEM experiments was used.[65] The experimental setup is illustrated in Figure 28a. The reactor consists of a chamber connected to micrometer-size gas-flow channels. Two SiN_x windows separate the reactor from the outer environment. The windows are etched down to a thickness of 10 nm in certain areas to maximize X-ray transmission. Heating is provided by a Pt spiral embedded in one of the windows. The reactor is supported on an adapter mounted on a controlled stage that can translate the sample in the X-ray beam with nanometer precision. By doing so, it was possible to take STXM images with a $35 \times 35\ nm^2$ step size.

Figure 28b–e shows 2D STXM contour plots of the Fe-based FTS catalyst after calcination, after reduction in H_2 at 350°C, and during CO hydrogenation at 250°C obtained by monitoring the C K edge, O K edge, and the Fe L_2 and L_3 edges. This measurement procedure enabled the researchers to precisely identify which Fe and C phases are present at the nanometer scale in a gas atmosphere. From Figure 28b it was concluded that the starting FTS catalyst material contains the Fe phase mainly as α-Fe_2O_3, which is dispersed on SiO_2. After 2 h in H_2 at 350°C, the catalyst material shows significant compositional changes. The 2D contour plot in Figure 28c indicates that Fe_2O_3 is completely converted into a mixture of other iron oxides. More specifically, it was found that regions initially containing Fe_2O_3 were transformed into regions containing various amounts of Fe_3O_4, Fe_2SiO_4, and Fe^0. During the subsequent FTS reaction in synthesis gas, the Fe_3O_4 phase is further converted to Fe^0 and Fe_2SiO_4. Figure 28d shows the chemical composite contour map of the selected region after 4 h of reaction. Quantitative analysis of the Fe L_2 and L_3 edge spectra originating from region 1 suggests a catalyst phase composition of 20% Fe^0, 75% Fe_2SiO_4, and 5% Fe_3O_4. Region 2 in Figure 28d instead has a chemical composition of approximately 40% Fe^0, 50% Fe_2SiO_4, and 10% Fe_3O_4. Interestingly, the developed method also allows the carbon species to be characterized at the nanoscale using the C K edge. Figure 28e shows that the Fe phase is converted into an iron carbide phase. Interestingly, in the region where less Fe is present (region 1), deposits with sp^3-hybridized carbon centers can be observed, indicative of FTS reaction products. The presence of reactant carbon species in Fe-deficient areas indicates that the support might have some role in the spillover of hydrocarbon species from the active metal to the support, thereby preventing blocking of the active site of the catalyst material.

In a related study, De Smit et al.[66] compared the reduction behavior of an iron-based FTS catalyst as probed with STXM with average oxidation-state values obtained with the bulk measuring method temperature-programmed reduction (TPR). Figure 29 shows the 2D STXM contour plots of a Fe FTS catalyst particle measured in situ at increasing reduction temperatures in a flow of H_2. The average oxidation state of iron can be determined by summing up the individual contributions of all $35 \times 35\ nm^2$ pixels in each contour plot. These numbers can be directly compared with values for the bulk average iron oxidation state as determined with the TPR method, which are included in Figure 29. A remarkable correspondence was found, thus indicating that in situ STXM reveals nanoscale differences in the redox behavior of a

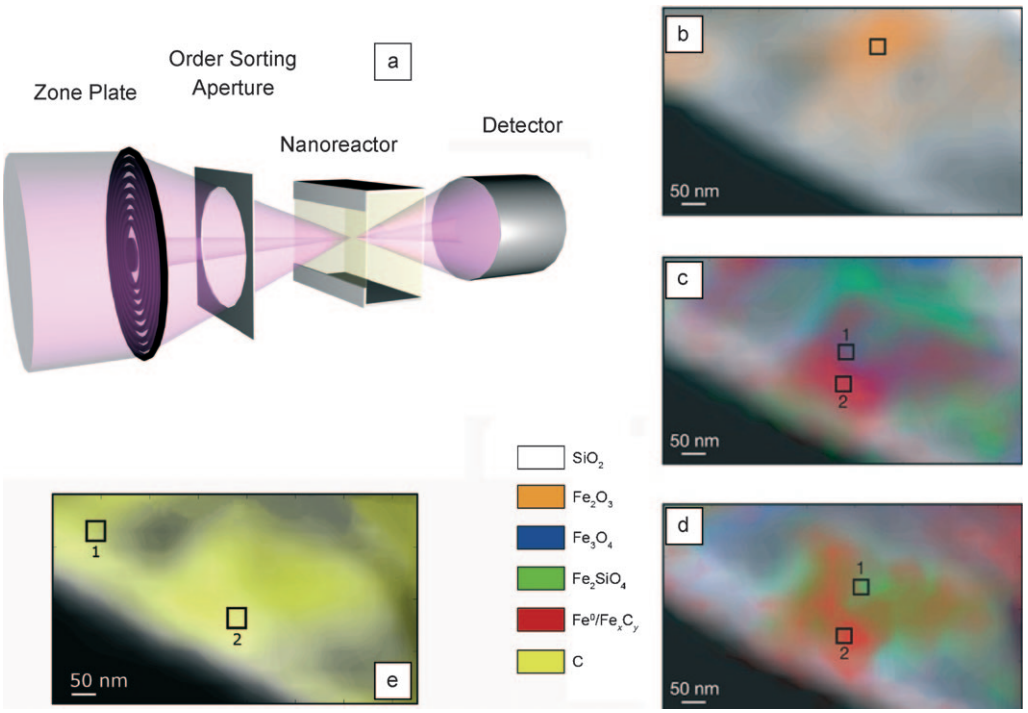

Figure 28. a) Experimental layout of scanning transmission X-ray microscopy (STXM) for measuring an iron-based Fischer–Tropsch catalyst particle under reaction conditions. b–e) 2D STXM contour maps of a 400×750 nm^2 region: b) before treatment at room temperature in He, c) after 2 h in H_2 at 350 °C, d) after 4 h in synthesis gas at 250 °C, e) after 4 h in synthesis gas at 250 °C showing the distribution of C species overlaid on the Fe species map. Reproduced from reference [64], copyright Nature Publishing Group, 2008.

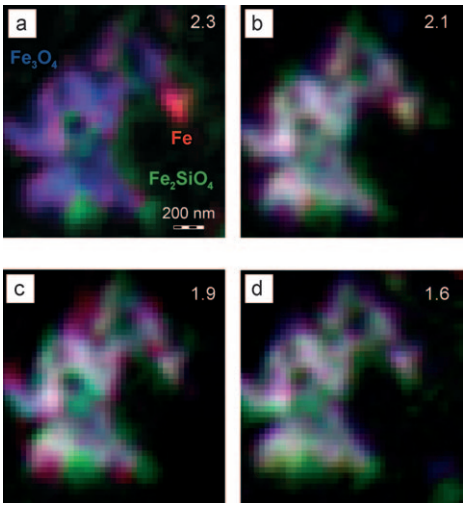

Figure 29. 2D Scanning transmission X-ray microscopy (STXM) images of an iron-based Fischer–Tropsch catalyst particle, showing the spatial distribution of the different Fe species in 1 bar H_2 at a) 250, b) 300, c) 350, and d) 450 °C. The pixel dimensions are 35×35 nm^2. The average valence of the whole catalyst particle is indicated in the top right corner of each image. Reproduced from reference [66].

catalyst material, but that these intricate differences still can be explained, as they should be, in terms of the macroscopic behavior of the catalyst material.

3. Future Prospects

The examples discussed above illustrate the enormous potential for studying the dynamics and spatial heterogeneities of catalytic solids in great detail at different length scales. As this research field is still in its infancy many more breakthroughs are to be expected. It is my personal belief that future breakthroughs can be made in at least the following three areas of research.

3.1. Microscopy of Labeled Samples and Label-Free Microscopy

One of the goals of heterogeneous catalysis research is the elucidation of reaction pathways, which requires the reliable identification of reactant, potential intermediates, and product molecules during a catalytic transformation process. It has been shown in analytical sciences that molecular identification and quantification can be done most reliably by using electronic (UV/Vis and fluorescence), vibrational (IR and Raman), and NMR spectroscopy as well as combinations of these three methods. Each of these techniques, as discussed in this Review, can be applied in a microscopic fashion, but chemical information density and time resolution are of equal importance. The most sensitive methods are based on electronic spectroscopy. However, their use requires specific probe reactions and marker molecules. These probe molecules can be made visible by either UV/Vis or fluorescence microscopy within a catalytic solid, preferably in 3D. This is

the field of label microscopy, and important developments in biology and the life sciences have led to the advanced use of many different fluorescent probes and molecular tags. As shown by several examples in this Review, label microscopy is slowly but surely making its way into the chemical imaging of heterogeneous catalysts. A clear advantage is the strong optical behavior of specific probe reactions, even allowing single-molecule detection in specific cases. As a consequence, the further development and use of a wider range of fluorescent probes, their 3D detection, for example by confocal microscopy, and their single-molecule detection will make fluorescence microscopy a powerful and widely useful imaging method for various forms of heterogeneous catalysis.[67] Unfortunately, most probe reactions to date have been developed for acid–base reactions, and clearly there is a need for a broader variety of optical labels. More specifically, by changing the size of the optical label, certain micro- and mesopores can be selectively assessed, whereas pores that are too small remain inaccessible for the markers. By connecting reactivity and selectivity to these labels of different sizes, it becomes possible to spatially resolve acid–base and redox properties within a catalytic solid.

Although the use of optical labels clearly has its advantages, it would be beneficial to monitor the reactants and reaction products of relevance in a realistic chemical process in 2D or 3D, a field which is coined label-free microscopy. Infrared absorption and Raman scattering are ideally suited for such developments, as the characteristic vibrations of various chemical bonds and functional groups can be directly probed. Another advantage is that well-known molecular probes, such as CO, NO, and pyridine, have already been used in combination with IR spectroscopy for assessing the properties of acid sites and supported metal nanoparticles, for example. Unfortunately, infrared microscopy has limited spatial resolution, although by using synchrotron IR radiation in combination with advanced focal plane array detection its capabilities for catalysis research can be greatly improved.[68] Spontaneous Raman scattering microscopy, on the other hand, while having a spatial resolution comparable to that of fluorescence microscopy, is rather insensitive and therefore has a limited imaging speed. Surface-enhanced Raman scattering (SERS) may significantly improve the sensitivity of the Raman method. It has even been possible to achieve single-molecule SERS for dye molecules on Ag colloids.[69] An example on the application of in situ SERS to study the citrate oxidation on silica-supported Ag nanoparticles was reported by Tada et al.[70] An alternative way of measuring Raman spectra is by applying the coherent anti-Stokes Raman scattering (CARS) process to microscopy.[71] In CARS microscopy, the temporally and spatially overlapped pump and Stokes laser pulses are tightly focused into a sample to generate a signal in a small volume. This procedure leads to a much higher sensitivity than spontaneous Raman microscopy. A first promising example of CARS microscopy close to an application in catalysis was achieved by Schäfer et al.[72] This group has recently shown that concentration profiles for the proton transfer reaction between pyrrolidine and acetic acid could be quantitatively determined with 3D sub-micrometer spatial resolution. It is clear that this method has a lot of potential for catalysis research. However, a CARS spectrum differs from its corresponding Raman spectrum by its nonresonant background, which complicates spectral assignments, limits detection sensitivity, and causes difficulties in interpretation of the images obtained. A promising alternative to CARS microscopy is stimulated Raman scattering (SRS), which is a 3D multiphoton vibrational imaging technique. The strength of this method has been recently illustrated by Freudiger et al. for biomedical imaging applications.[73]

3.2. Towards In Situ Optical Tomography at the Nanoscale

The above-mentioned developments for making assays of optical labels to visualize pore architecture and catalytic reactivity will go hand in hand with technical developments for further improving the spatial resolution below the diffraction limit of light (about 250 nm for UV/Vis light in the lateral dimensions, Table 1) and the potential use of such labels for single-molecule imaging. For example, to distinguish the signals from two identical fluorescent molecules that are only a few tens of nanometers apart, the experimental setup must ensure that the molecules do not emit simultaneously at all times with the same emission properties. In the last 10 years we have seen the discovery of several appropriate experimental approaches, particularly developed for life sciences, that allow lateral imaging resolutions of 20–50 nm. The first involves active control through stimulated emission depletion (STED), as developed by Hell and coworkers,[74] while a second approach makes use of stochastic readouts based on photophysical and photochemical effects of the emitting source, such as photoinduced blinking, bleaching, or switching. The latter approaches are termed fluorescence photoactivated localization microscopy (FPALM)[75] and stochastic optical reconstruction microscopy (STORM).[76] Although these techniques provide 2D image "superresolution", it would be advantageous to have high resolution in the third dimension as well. Confocal microscopy leads to axial resolutions of about 500 nm,[77] although it can be improved to about 100 nm using 4Pi and I^5M microscopy.[78] With STED using the 4Pi illumination geometry, an axial resolution of 30–50 nm can be reached,[79] while more recently 3D STORM imaging has been developed using optical astigmatism to determine both axial and lateral positions of individual fluorescent molecules with nanometer accuracy.[80] It is expected that the introduction of these advanced FF fluorescence microscopy methods, when applied in the field of heterogeneous catalysis, will further increase our understanding of the pore architecture of complex catalytic solids as well as their reaction mechanisms.

A similar trend towards increasing 2D and 3D imaging capabilities can be found in the field of X-ray microscopy, which fills the spatial resolution gap between optical microscopy and electron microscopy. Although the manufacture of high-resolution X-ray lenses is very challenging owing to strong light absorption, it is clear that catalysis scientists will benefit from expected advances in X-ray microscopy instrumentation. X-rays have very short wavelengths and are

therefore ideally suited for achieving high spatial resolution. For example, the FF spatial resolution for X-ray imaging at the C1s edge is 4 nm.[81] Furthermore, X-ray-based tomography allows for the nondestructive, label-free chemical imaging of catalytic solids. A first encouraging example of computed microtomography and micro-X-ray fluorescence for studying catalytic solids was reported by Jones et al.[82] Current instrumentation for X-ray tomography at the nanoscale falls into two categories:[83] microscopes that require optics such as zone plates and microscopes that don't require any focusing optical elements. An optics-based microscope can be either a full-field transmission X-ray microscope (TXM) or scanning transmission X-ray microscope (STXM). Microscopes that don't require focusing optics are classified as lensless projection imaging microscopes (PIMs) or diffraction imaging microscopes (DIMs). Tomographic measurements can be carried out most easily with TXM, as the time needed for a single image is much shorter, although beam damage may then become a problem. Current spatial resolutions are better than 15 nm,[84] and in the near future the achievable resolution can be extended by further improving the X-ray optics.[85] Another way to achieve higher spatial resolution is by combining diffraction imaging with STXM, as recently illustrated by Thibault et al.[86] The developed high-resolution scanning X-ray diffraction microscope may achieve a spatial resolution below 10 nm by using the angularly resolved transmitted diffraction patterns instead of total transmission patterns when building up the STXM images.

3.3. Development of Correlative Microscopy Approaches

It is advantageous to look at catalysts from different perspectives by making use of multiple techniques. In the last decade many attempts have been made to combine multiple spectroscopic techniques into one setup to perform correlative spectroscopy on the same catalyst material under identical conditions without the need for sample transfer.[87] This approach has lead to the development of different combined in situ setups, such as XRD/XAFS,[88] ESR/UV/Vis,[89] Raman/UV/Vis,[90] NMR/UV/Vis,[91] Raman/IR,[92] XAFS/IR,[93] IR/UV/Vis,[94] XAFS/Raman/UV/Vis,[95] ESR/UV/Vis/Raman,[96] and XAFS/SAXS/WAXS/UV/Vis/Raman (XAFS = X-ray absorption fine structure, SAXS = small-angle X-ray scattering, WAXS = wide-angle X-ray scattering).[97] Besides gathering complementary structural, electronic, and kinetic information on a catalytic process, these methods also allow evaluation of the reliability of the measurements by cross-checking two or more sets of spectroscopic data. This last aspect is of prime importance when working with lasers or synchrotron radiation. For example, in the case of high-flux third-generation synchrotron sources, X-ray-induced local heating or sample degradation and reduction phenomena can seriously undermine the reliability of the conclusions drawn.[98]

It is anticipated that the same experimental approach can be used for the application of different microscopy methods to the same catalyst material. The most evident combinations are then based on optical methods, such as IR/Raman, UV/Vis/Raman, and UV/Vis/fluorescence microscopy combinations, some of which are already commercially available or in their final development phase. Combinations of other microscopic techniques, already available for other fields of application, could also find their way into the field of heterogeneous catalysis. One such setup has been developed by Majors et al. and involves the combination of confocal fluorescence microscopy with NMR microscopy.[99] Another possibility includes the combination of fluorescence microscopy and transmission electron microscopy (TEM). Detailed structural studies of catalyst materials with nanometer or Ångström resolution can be performed with TEM. However, its high spatial resolution makes scanning of complete TEM grids at such high resolution extremely time-consuming. This limitation has motivated researchers to pursue imaging methods that combine TEM with either fluorescence[100] or Raman microscopy.[101] In the case of fluorescence microscopy most correlative microscopy has been carried out in two separate setups.[104] Fluorescence microscopy is first employed to identify and locate features of interest, while TEM is used to map the ultrastructure within a specimen. Carrying out such experiments using two separate instruments is, however, cumbersome. The main problem is the pin-pointing in the TEM image the region of interest identified by fluorescence microscopy. This is time-consuming and error-prone, even when the labeling is done with markers that are visible with both techniques. Furthermore, the transfer of the specimen from the fluorescence microscope to the TEM instrument involves additional handling steps that may compromise the integrity of the specimen. Detailed protocols have been proposed for improving the success rate of recording correlative microscopy images. A recent development has been the integration of a laser scanning fluorescence microscope in a TEM microscope.[102] Using this approach the search for features in the specimen is greatly simplified, and the time necessary to carry out the experiment is significantly reduced. It is anticipated that these correlative methods and their extension with other optical methods will bring new insights to the field of heterogeneous catalysts.

A final promising area of correlative microscopy is the combination of atomic force microscopy (AFM) methods[103] with optical techniques, such as fluorescence, IR, and Raman spectroscopy. This is the area of scanning near-field optical microscopy (SNOM), which allows for spatial resolutions below 100 nm and can therefore be considered as a true nanoscopy method.[104] AFM methods have already been successfully applied in the field of heterogeneous catalysis. For example, AFM has been used to study the surface topography of microporous materials, such as zeolites, and for the characterization of fluid catalytic cracking (FCC) catalysts.[105] Since commercial instrumentation that couples SNOM with Raman and/or fluorescence microscopy exists, it is expected that these methods will soon be applied to catalytic solids under in situ conditions. A first attempt in this direction has been made by Fokas and Deckert, showing SERS effects under nonreactive conditions for benzene deposited onto a Ag/Pd substrate.[106] Another related approach is tip-enhanced Raman spectroscopy (TERS), which has shown 15 nm spatial resolution and allows for

single-molecule detection at well-defined surfaces.[107] Other interesting avenues based on near-field spectroscopy concepts include the use of scanning near field infrared microscopy (SNIM)[108] and terahertz near-field microscopy.[109] The former method allows label-free spectroscopy by measuring local infrared spectra with a spatial resolution down to 30 nm.

B.M.W. acknowledges financial support from the Netherlands Organization for Scientific Research (NWO-CW: Van der Leeuw, VICI, and TOP grants), the Advanced Chemical Technology for Sustainability program (ACTS-ASPECT grants), Top Research School Combination Catalysis (NRSC-Catalysis), Albemarle Catalysts, Toyota, Dow Chemicals, BASF, Total, SK Energy and Shell. This Review is dedicated to the many PhD students, postdoctoral fellows, and scientific and technical staff at Utrecht University for their contributions to the field of space- and time-resolved in situ spectroscopy.

Received: January 19, 2009

[1] *Handbook of Heterogeneous Catalysis*, 2nd ed. (Eds.: G. Ertl, H. Knozinger, F. Schuth, J. Weitkamp), Wiley-VCH, Weinheim, **2008**.

[2] J. Hagen, *Industrial Catalysis: A Practical Approach*, Wiley-VCH, Weinheim, **1999**.

[3] H. F. Rase, *Handbook of Commercial Catalysts*, CRC, New York, **2000**.

[4] *Supported Metals in Catalysis* (Eds.: J. A. Anderson, M. Fernandez Garcia), Imperial College Press, London, **2005**.

[5] J. M. Thomas, W. J. Thomas, *Principles and Practice of Heterogeneous Catalysis*, VCH, Weinheim, **1997**.

[6] J. W. Niemantsverdriet, *Spectroscopy in Catalysis, An Introduction*, 3rd ed., VCH, Weinheim, **2007**.

[7] A typical example of a heterogeneous catalyst that contains a wide variety of active sites, each with their own reactivity, is the Cr/SiO_2 Phillips catalyst. This material is responsible for about 40% of the worldwide production of high-density and linear low-density polyethylene (HDPE and LLDPE). Different Cr^{2+} and Cr^{3+} species can coexist, each with their own degree of coordinative unsaturation and related ethylene polymerization activity. The relative population of these species can be interchanged by applying specific chemical or thermal treatments. For more details, see: B. M. Weckhuysen, I. E. Wachs, R. A. Schoonheydt, *Chem. Rev.* **1996**, *96*, 3327; B. M. Weckhuysen, R. A. Schoonheydt, *Catal. Today* **1999**, *51*, 215; E. Groppo, C. Lamberti, S. Bordiga, G. Spoto, A. Zecchina, *Chem. Rev.* **2005**, *105*, 115; C. N. Nenu, E. Groppo, C. Lamberti, A. M. Beale, T. Visser, A. Zecchina, B. M. Weckhuysen, *Angew. Chem.* **2007**, *119*, 1487; *Angew. Chem. Int. Ed.* **2007**, *46*, 1465.

[8] To date, two books cover the field of in situ spectroscopy of catalytic solids: *In-Situ Spectroscopy in Heterogeneous Catalysis* (Ed.: J. F. Haw), Wiley-VCH, Weinheim, **2002**; *In-Situ Spectroscopy of Catalysts* (Ed.: B. M. Weckhuysen), American Scientific Publishers, **2004**.

[9] Several reviews cover the field of in situ spectroscopy of catalytic solids dealing with 0D measurements: B. M. Weckhuysen, *Chem. Commun.* **2002**, 97; B. M. Weckhuysen, *Phys. Chem. Chem. Phys.* **2003**, *5*, 4351; M. Hunger, J. Weitkamp, *Angew. Chem.* **2001**, *113*, 3040; *Angew. Chem. Int. Ed.* **2001**, *40*, 2954; M. A. Banares, *Catal. Today* **2005**, *100*, 71; C. Lamberti, E. Groppo, G. Spoto, S. Bordiga, A. Zecchina, *Adv. Catal.* **2007**, *51*, 1; P. C. Stair, *Adv. Catal.* **2007**, *51*, 75; J. M. Thomas, C. R. A. Catlow, G. Sankar, *Chem. Commun.* **2002**, 2921; J. M. Thomas, *Angew. Chem.* **1999**, *111*, 3800; *Angew. Chem. Int. Ed.* **1999**, *38*, 3588; H. Topsøe, *J. Catal.* **2003**, *216*, 155.

[10] Examples of the development of structure–activity relationships in the field of metal catalysis: M. Tada, Y. Akatsuka, Y. Yang, T. Sasaki, M. Kinoshita, K. Motokura, Y. Iwasawa, *Angew. Chem.* **2008**, *120*, 9392; *Angew. Chem. Int. Ed.* **2008**, *47*, 9252; M. Tada, Y. Iwasawa, *Coord. Chem. Rev.* **2007**, *251*, 2702; T. Yamamoto, A. Suzuki, Y. Nagai, T. Tanabe, F. Dong, Y. Inada, M. Nomura, M. Tada, Y. Iwasawa, *Angew. Chem.* **2007**, *119*, 9413; *Angew. Chem. Int. Ed.* **2007**, *46*, 9253; M. Tada, R. Coquet, J. Yoshida, M. Kinoshita, Y. Iwasawa, *Angew. Chem.* **2007**, *119*, 7358; *Angew. Chem. Int. Ed.* **2007**, *46*, 7220; J. Singh, E. M. C. Alayon, M. Tromp, O. V. Safonova, P. Glatzel, M. Nachtegaal, R. Frahm, J. A. van Bokhoven, *Angew. Chem.* **2008**, *120*, 9400; *Angew. Chem. Int. Ed.* **2008**, *47*, 9260; E. Bus, D. E. Ramaker, J. A. van Bokhoven, *J. Am. Chem. Soc.* **2007**, *129*, 8094; J. A. van Bokhoven, C. Louis, J. T. Miller, M. Tromp, O. V. Safonova, P. Glatzel, *Angew. Chem.* **2006**, *118*, 4767; *Angew. Chem. Int. Ed.* **2006**, *45*, 4651; F. C. Meunier, A. Goguet, S. Shekhtman, D. Rooney, H. Daly, *Appl. Catal. A* **2008**, *340*, 196; F. C. Meunier, A. Goguet, C. Hardacre, R. Burch, D. Thompsett, *J. Catal.* **2007**, *252*, 18; F. C. Meunier, D. Reid, A. Goguet, S. Shekhtman, C. Hardacre, R. Burch, W. Deng, M. Flytzani-Stephanopoulos, *J. Catal.* **2007**, *247*, 277; J. M. Thomas, R. Raja, *Acc. Chem. Res.* **2008**, *41*, 708; J. M. Thomas, R. Raja, D. W. Lewis, *Angew. Chem.* **2005**, *117*, 6614; *Angew. Chem. Int. Ed.* **2005**, *44*, 6456.

[11] Examples of the development of structure–activity relationships in the field of metal oxide catalysis: M. V. Martinez-Huerta, G. Deo, J. L. G. Fierro, M. A. Banares, *J. Phys. Chem. C* **2008**, *112*, 11441; H. Si-Ahmed, M. Calatayud, C. Minot, E. L. Diz, A. E. Lewandowska, M. A. Banares, *Catal. Today* **2007**, *126*, 96; M. V. Martinez-Huerta, X. Gao, H. Tian, I. E. Wachs, J. L. G. Fierro, M. A. Banares, *Catal. Today* **2006**, *118*, 279; M. A. Banares, S. J. Khatib, *Catal. Today* **2004**, *96*, 251; C. L. Zhao, I. E. Wachs, *J. Phys. Chem. C* **2008**, *112*, 11363; T. Kim, A. Burrows, C. J. Kiely, I. E. Wachs, *J. Catal.* **2007**, *246*, 370; H. J. Tian, E. I. Ross, I. E. Wachs, *J. Phys. Chem. B* **2006**, *110*, 9593; I. E. Wachs, *Catal. Today* **2005**, *100*, 79; I. E. Wachs, Y. Chen, J. M. Jehng, L. E. Briand, T. Tanaka, *Catal. Today* **2003**, *78*, 13; S. W. Yang, E. Iglesia, A. T. Bell, *J. Phys. Chem. B* **2005**, *109*, 8987; M. D. Argyle, K. D. Chen, C. Resini, C. Krebs, A. T. Bell, E. Iglesia, *J. Phys. Chem. B* **2004**, *108*, 2345; M. D. Argyle, K. D. Chen, C. Resini, C. Krebs, A. T. Bell, E. Iglesia, *Chem. Commun.* **2003**, 2082; E. Groppo, C. Lamberti, F. Cesano, A. Zecchina, *Phys. Chem. Chem. Phys.* **2006**, *8*, 2453; S. Bordiga, S. Bertarione, A. Damn, C. Prestipino, G. Spoto, C. Lamberti, A. Zecchina, *J. Mol. Catal. A* **2003**, *204*, 527; Z. L. Wu, P. C. Stair, *J. Catal.* **2006**, *237*, 220; Y. Zhang, A. T. Bell, *J. Catal.* **2008**, *255*, 153; M. H. Groothaert, J. A. van Bokhoven, A. A. Battiston, B. M. Weckhuysen, R. A. Schoonheydt, *J. Am. Chem. Soc.* **2003**, *125*, 7629; S. Bordiga, F. Bonino, A. Damin, C. Lamberti, *Phys. Chem. Chem. Phys.* **2007**, *9*, 4854; G. Ertl, *Angew. Chem.* **2008**, *120*, 3578; *Angew. Chem. Int. Ed.* **2008**, *47*, 3524; S. O. Lee, R. Raja, K. D. M. Harris, J. M. Thomas, B. F. G. Johnson, G. Sankar, *Angew. Chem.* **2003**, *115*, 1558; *Angew. Chem. Int. Ed.* **2003**, *42*, 1520.

[12] G. Ertl, *Angew. Chem.* **2008**, *120*, 3578; *Angew. Chem. Int. Ed.* **2008**, *47*, 3524; J. Wolff, A. G. Papathanasiou, Y. Kevrekidis, H. H. Rotermund, G. Ertl, *Science* **2001**, *294*, 134; C. Sachs, M. Hildebrand, S. Volkening, J. Wintterlin, G. Ertl, *Science* **2001**, *293*, 1635; M. Kim, M. Bertram, M. Pollmann, A. van Oertzen, A. S. Mikhailov, H. H. Rotermund, G. Ertl, *Science* **2001**, *292*, 1357.

[13] It is important to realize that the movie does not completely reflect reality. More specifically, the visualized industrial plant

does not make use of Pt–Sn nanoparticles occluded in the supercages of zeolite Y, as suggested in the movie, but is based on a Cr/Al_2O_3 catalyst. For details on the Houdry alkane dehydrogenation process, see: B. M. Weckhuysen, R. A. Schoonheydt, *Catal. Today* **1999**, *51*, 223. Furthermore, the movie has proven to be very instructive for catalysis courses for bachelor and master students. When using this movie for educational purposes, please make reference to this Review.

[14] R. Narayanan, M. A. El-Sayed, *J. Phys. Chem. B* **2005**, *109*, 12663; A. Zecchina, E. Groppo, S. Bordiga, *Chem. Eur. J.* **2007**, *13*, 2440.

[15] N. Tian, Z. Y. Zhou, S. G. Sun, Y. Ding, Z. L. Wang, *Science* **2007**, *316*, 732; D. Feldheim, *Science* **2007**, *316*, 699; Y. Xiong, B. J. Wiley, Y. Xia, *Angew. Chem.* **2007**, *119*, 7291; *Angew. Chem. Int. Ed.* **2007**, *46*, 7157.

[16] H. Su, E. S. Yeung, *J. Am. Chem. Soc.* **2000**, *122*, 7422; H. Su, Y. Hou, R. S. Houk, G. L. Schrader, E. S. Yeung, *Anal. Chem.* **2001**, *73*, 4434; H. Su, E. S. Yeung, *Appl. Spectrosc.* **2002**, *56*, 1044; R. A. Potyrailo, J. P. Lemmon, T. K. Leib, *Anal. Chem.* **2003**, *75*, 4676; G. Li, D. Hu, G. Xia, J. M. White, C. Zhang, *Rev. Sci. Instrum.* **2008**, *79*, 074101; F. Aiouache, H. Oyama, K. Kitagawa, *AIChE J.* **2006**, *52*, 1516; C. M. Snively, G. Oskarsdottir, J. Lauterbach, *Catal. Today* **2001**, *67*, 357; P. Kubanek, O. Busch, S. Thomson, H. W. Schmidt, F. Schuth, *J. Comb. Chem.* **2004**, *6*, 420; O. M. Busch, W. Brijoux, S. Thomson, F. Schuth, *J. Catal.* **2004**, *222*, 174; R. J. Hendershot, R. Vijay, B. J. Feist, C. M. Snively, J. Lauterbach, *Meas. Sci. Technol.* **2005**, *16*, 302.

[17] E. H. L. Yuen, A. J. Sederman, L. F. Gladden, *Appl. Catal. A* **2002**, *232*, 29; L. F. Gladden, M. D. Mantle, A. J. Sederman, *Adv. Catal.* **2006**, *50*, 1.

[18] I. V. Koptyug, A. A. Lysova, R. Z. Sagdeev, V. N. Parmon, *Catal. Today* **2007**, *126*, 37; A. A. Lysova, I. V. Koptyug, A. V. Kulikov, V. A. Kirilov, R. Z. Sagdeev, V. N. Parmon, *Chem. Eng. J.* **2007**, *130*, 101; I. V. Koptyug, A. A. Lysova, A. V. Kulikov, V. A. Kirilov, V. N. Parmon, R. Z. Sagdeev, *Appl. Catal. A* **2004**, *267*, 143.

[19] B. S. Akpa, M. D. Mantle, A. J. Sederman, L. F. Gladden, *Chem. Commun.* **2005**, 2741.

[20] A. J. Sederman, M. D. Mantle, C. P. Dunckley, Z. Huang, L. F. Gladden, *Catal. Lett.* **2005**, *103*, 1.

[21] L. S. Bouchard, K. V. Kovtunov, S. R. Burt, M. S. Anwar, I. V. Koptyug, R. Z. Sagdeev, A. Pines, *Angew. Chem.* **2007**, *119*, 4142; *Angew. Chem. Int. Ed.* **2007**, *46*, 4064.

[22] L. S. Bouchard, S. R. Burt, M. S. Anwar, K. V. Kovtunov, I. V. Koptyug, A. Pines, *Science* **2008**, *319*, 442.

[23] J. D. Grunwaldt, S. Hannemann, C. G. Schroer, A. Baiker, *J. Phys. Chem. B* **2006**, *110*, 8674.

[24] S. Hannemann, J. D. Grunwaldt, N. van Vegten, A. Baiker, P. Boye, C. G. Schroer, *Catal. Today* **2007**, *126*, 54.

[25] J. D. Grunwaldt, B. Kimmerle, A. Baiker, P. Boye, C. G. Schroer, P. Glatzel, C. N. Borca, F. Beckmann, *Catal. Today* **2009**, DOI: 10.1016/j.cattod.2008.11.002.

[26] A. Urakawa, N. Maeda, A. Baiker, *Angew. Chem.* **2008**, *120*, 9396; *Angew. Chem. Int. Ed.* **2008**, *47*, 9256.

[27] T. A. Nijhuis, S. J. Tinnemans, T. Visser, B. M. Weckhuysen, *Chem. Eng. Sci.* **2004**, *59*, 5487.

[28] R. Morschl, J. Bolten, A. Bonnefont, K. Krischer, *J. Phys. Chem. C* **2008**, *112*, 9548.

[29] J. A. Bergwerff, L. G. A. van de Water, T. Visser, P. de Peinder, B. R. G. Leliveld, K. P. de Jong, B. M. Weckhuysen, *Chem. Eur. J.* **2005**, *11*, 4591.

[30] T. Mang, B. Breitscheidel, P. Polanek, H. Knozinger, *Appl. Catal. A* **1993**, *106*, 239.

[31] J. A. Bergwerff, T. Visser, B. R. G. Leliveld, B. A. Rossenaar, K. P. de Jong, B. M. Weckhuysen, *J. Am. Chem. Soc.* **2004**, *126*, 14548; J. A. Bergwerff, L. G. A. van de Water, A. A. Lysova, I. V. Koptyug, T. Visser, K. P. de Jong, B. M. Weckhuysen, *Stud. Surf. Sci. Catal.* **2006**, *162*, 175; J. A. Bergwerff, T. Visser, B. M. Weckhuysen, *Catal. Today* **2008**, *130*, 117.

[32] L. G. A. van de Water, J. A. Bergwerff, T. A. Nijhuis, K. P. de Jong, B. M. Weckhuysen, *J. Am. Chem. Soc.* **2005**, *127*, 5024; L. G. A. van de Water, J. A. Bergwerff, B. R. G. Leliveld, B. M. Weckhuysen, K. P. de Jong, *J. Phys. Chem. B* **2005**, *109*, 14513.

[33] L. Espinosa Alonso, K. P. de Jong, B. M. Weckhuysen, *J. Phys. Chem. C* **2008**, *112*, 7201.

[34] A. A. Lysova, I. V. Koptyug, R. Z. Sagdeev, V. N. Parmon, J. A. Bergwerff, B. M. Weckhuysen, *J. Am. Chem. Soc.* **2005**, *127*, 11916.

[35] J. A. Bergwerff, A. A. Lysova, L. Espinosa Alonso, I. V. Koptyug, B. M. Weckhuysen, *Angew. Chem.* **2007**, *119*, 7362; *Angew. Chem. Int. Ed.* **2007**, *46*, 7224.

[36] J. A. Bergwerff, A. A. Lysova, L. Espinosa Alonso, I. V. Koptyug, B. M. Weckhuysen, *Chem. Eur. J.* **2008**, *14*, 2363.

[37] The indirect ^1H MRI method can be further refined by making use of the different relaxation times of distinct transition-metal ion complexes occluded in the pores of catalyst bodies. For a recent example on Ni^{2+} complexes, see: L. Espinosa-Alonso, A. A. Lysova, P. de Peinder, K. P. de Jong, I. V. Koptyug, B. M. Weckhuysen, *J. Am. Chem. Soc.* **2009**, *131*, 6525. Futhermore, transition-metal ions can also be directly probed by EPR microscopy. This technique was first applied in the field of heterogeneous catalysis by Zu et al. for spatially probing V^{4+} and Mo^{5+} in SiO_2-based catalyst bodies: Y. Zu, M. Furusawa, M. Ikeya, Y. Kera, K. Kuwata, *Chem. Lett.* **1991**, 293. There are two other reports on the application of EPR microscopy on catalytic solids: O. E. Yakimchenko, E. N. Degtyarev, V. N. Parmon, Y. S. Lebedev, *J. Phys. Chem.* **1995**, *99*, 2038; Z. Xiang, Y. Xu, *Appl. Magn. Reson.* **1997**, *12*, 68.

[38] L. G. A. van de Water, G. L. Bezemer, J. A. Bergwerff, M. Versluijs-Helder, B. M. Weckhuysen, K. P. de Jong, *J. Catal.* **2006**, *242*, 287.

[39] J. A. Bergwerff, M. Jansen, B. R. G. Leliveld, T. Visser, K. P. de Jong, B. M. Weckhuysen, *J. Catal.* **2006**, *243*, 292.

[40] A. M. Beale, S. D. M. Jacques, J. A. Bergwerff, P. Barnes, B. M. Weckhuysen, *Angew. Chem.* **2007**, *119*, 8988; *Angew. Chem. Int. Ed.* **2007**, *46*, 8832.

[41] J. Kärger, P. Kortunov, S. Vasenkov, L. Heinke, D. B. Shah, R. A. Rakoczy, Y. Traa, J. Weitkamp, *Angew. Chem.* **2006**, *118*, 8010; *Angew. Chem. Int. Ed.* **2006**, *45*, 7846.

[42] D. Tzoulaki, L. Heinke, W. Schmidt, U. Wilczok, J. Kärger, *Angew. Chem.* **2008**, *120*, 4018; *Angew. Chem. Int. Ed.* **2008**, *47*, 3954.

[43] P. Kortunov, S. Vasenkov, C. Chmelik, J. Kärger, D. M. Ruthven, J. Wloch, *Chem. Mater.* **2004**, *16*, 3552.

[44] O. Geier, S. Vasenkov, E. Lehmann, J. Kärger, U. Schemmert, R. A. Rakoczy, J. Weitkamp, *J. Phys. Chem. B* **2001**, *105*, 10217.

[45] M. B. J. Roeffaers, B. F. Sels, H. Uji-i, B. Blanpain, P. L'hoest, P. A. Jacobs, F. C. De Schryver, J. Hofkens, D. E. De Vos, *Angew. Chem.* **2007**, *119*, 1736; *Angew. Chem. Int. Ed.* **2007**, *46*, 1706;.

[46] M. B. J. Roeffaers, R. Ameloot, A. J. Bons, W. Mortier, G. De Cremer, R. De Kloe, J. Hofkens, D. E. De Vos, B. F. Sels, *J. Am. Chem. Soc.* **2008**, *130*, 13516.

[47] L. Karwacki, E. Stavitski, M. H. F. Kox, J. Kornatowski, B. M. Weckhuysen, *Angew. Chem.* **2007**, *119*, 7366; *Angew. Chem. Int. Ed.* **2007**, *46*, 7228.

[48] C. Seebacher, J. Rau, F. W. Deeg, C. Bräuchle, S. Altmaier, R. Jager, P. Behrens, *Adv. Mater.* **2001**, *13*, 1374.

[49] M. B. J. Roeffaers, R. Ameloot, M. Baruah, H. Uji-i, M. Bulut, G. De Cremer, U. Muller, P. A. Jacobs, J. Hofkens, B. F. Sels, D. E. De Vos, *J. Am. Chem. Soc.* **2008**, *130*, 5763.

[50] M. H. F. Kox, E. Stavitski, B. M. Weckhuysen, *Angew. Chem.* **2007**, *119*, 3726; *Angew. Chem. Int. Ed.* **2007**, *46*, 3652.

[51] E. Stavitski, M. H. F. Kox, B. M. Weckhuysen, *Chem. Eur. J.* **2007**, *13*, 7057.
[52] E. Stavitski, M. H. F. Kox, I. Swart, F. M. F. de Groot, B. M. Weckhuysen, *Angew. Chem.* **2008**, *120*, 3599; *Angew. Chem. Int. Ed.* **2008**, *47*, 3543; R. A. Schoonheydt, *Angew. Chem.* **2008**, *120*, 9328; *Angew. Chem. Int. Ed.* **2008**, *47*, 9188.
[53] E. Stavitski, M. R. Drury, D. A. M. de Winter, M. H. F. Kox, B. M. Weckhuysen, *Angew. Chem.* **2008**, *120*, 5719; *Angew. Chem. Int. Ed.* **2008**, *47*, 5637.
[54] M. H. F. Kox, E. Stavitski, J. C. Groen, J. Perez-Ramirez, F. Kapteijn, B. M. Weckhuysen, *Chem. Eur. J.* **2008**, *14*, 1718.
[55] D. Mores, E. Stavitski, M. H. F. Kox, J. Kornatowski, U. Olsbye, B. M. Weckhuysen, *Chem. Eur. J.* **2008**, *14*, 11320.
[56] A. Zürner, J. Kirstein, M. Doblinger, C. Bräuchle, T. Bein, *Nature* **2007**, *450*, 705.
[57] C. Jung, J. Kirstein, B. Platschek, T. Bein, M. Budde, I. Frank, K. Müllen, J. Michaelis, C. Bräuchle, *J. Am. Chem. Soc.* **2008**, *130*, 1638.
[58] J. Kirstein, B. Platschek, C. Jung, R. Brown, T. Bein, C. Bräuchle, *Nat. Mater.* **2007**, *6*, 303.
[59] T. Lebold, L. A. Mühlstein, J. Blechinger, M. Riederer, H. Amenitsch, R. Kohn, K. Peneva, K. Müllen, J. Michaelis, C. Bräuchle, T. Bein, *Chem. Eur. J.* **2009**, *15*, 1661.
[60] M. B. J. Roeffaers, B. F. Sels, H. Uji-i, F. C. De Schryver, P. A. Jacobs, D. E. De Vos, J. Hofkens, *Nature* **2006**, *439*, 572; B. M. Weckhuysen, *Nature* **2006**, *439*, 548.
[61] V. Martinez Martinez, G. De Cremer, M. B. J. Roeffaers, M. Sliwa, M. Baruah, D. E. De Vos, J. Hofkens, B. F. Sels, *J. Am. Chem. Soc.* **2008**, *130*, 13192.
[62] W. Xu, J. S. Kong, Y. T. E. Yeh, P. Chen, *Nat. Mater.* **2008**, *7*, 992; W. Xu, J. S. Kong, P. Chen, *Phys. Chem. Chem. Phys.* **2009**, *11*, 2767.
[63] K. Naito, T. Tachikawa, M. Fujitsuka, T. Majima, *J. Am. Chem. Soc.* **2009**, *131*, 934.
[64] E. De Smit, I. Swart, J. F. Creemer, G. H. Hoveling, M. K. Gilles, T. Tyliszczak, P. J. Kooyman, H. W. Zandbergen, C. Morin, B. M. Weckhuysen, F. M. F. De Groot, *Nature* **2008**, *456*, 222; A. T. Bell, *Nature* **2008**, *456*, 185; J. M. Thomas, J. C. Hernandez-Garrido, *Angew. Chem.* **2009**, *121*, 3962; *Angew. Chem. Int. Ed.* **2009**, *48*, 3904..
[65] J. F. Creemer, S. Helveg, G. H. Hoveling, S. Ullmann, A. M. Molenbroek, P. M. Sarro, H. W. Zandbergen, *Ultramicroscopy* **2008**, *108*, 993.
[66] E. De Smit, I. Swart, J. F. Creemer, C. Karunakaran, D. Bertwistle, H. W. Zandbergen, F. M. F. de Groot, B. M. Weckhuysen, *Angew. Chem.* **2009**, *121*, 3686; *Angew. Chem. Int. Ed.* **2009**, *48*, 3632.
[67] M. B. J. Roeffaers, G. De Cremer, H. Uji-I, B. Muls, B. F. Sels, P. A. Jacobs, F. C. De Schryver, D. E. De Vos, J. Hofkens, *Proc. Natl. Acad. Sci. USA* **2007**, *104*, 12603; M. B. J. Roeffaers, J. Hofkens, G. De Cremer, F. C. De Schryver, P. A. Jacobs, D. E. De Vos, B. F. Sels, *Catal. Today* **2007**, *126*, 44.
[68] J. Susini, M. Cotte, K. Scheidt, O. Chubar, F. Polack, P. Dumas, *Synchrotron Radiat. News* **2007**, *20*, 13; L. M. Miller, R. J. Smith, G. L. Carr, *Synchrotron Radiat. News* **2007**, *20*, 25; P. Lasch, D. Naumann, *Biochim. Biophys. Acta Biomembr.* **2006**, *1758*, 814; L. H. Kidder, I. W. Levin, E. N. Lewis, V. D. Kleiman, E. J. Heilweil, *Opt. Lett.* **1997**, *22*, 742; L. H. Kidder, V. F. Kalasinsky, J. L. Luke, I. W. Levin, E. N. Lewis, *Nat. Med.* **1997**, *3*, 235.
[69] L. Brus, *Acc. Chem. Res.* **2008**, *41*, 1742; S. M. Nie, S. R. Emery, *Science* **1997**, *275*, 1102; K. Kneipp, Y. Wang, H. Kneipp, L. T. Perelman, I. Itzkan, R. Dasari, M. S. Feld, *Phys. Rev. Lett.* **1997**, *78*, 1667.
[70] H. Tada, J. Bronkema, A. T. Bell, *Catal. Lett.* **2003**, *92*, 93. Most examples of SERS in the field of catalysis can be found for electrochemical reactions in the liquid phase, whereas the use of SERS for gas-phase reactions on solid surfaces is quite limited.
[71] A. Zumbusch, G. R. Holtom, X. S. Xie, *Phys. Rev. Lett.* **1999**, *82*, 4142; J. X. Cheng, X. S. Xie, *J. Phys. Chem. B* **2004**, *108*, 827; L. Li, J. X. Cheng, *J. Phys. Chem. B* **2008**, *112*, 1576; C. L. Evans, X. S. Xie, *Annu. Rev. Anal. Chem.* **2008**, *1*, 883; M. Müller, A. Zumbusch, *ChemPhysChem* **2007**, *8*, 2156..
[72] D. Schäfer, J. A. Squier, J. Van Maarseveen, D. Bonn, M. Bonn, M. Müller, *J. Am. Chem. Soc.* **2008**, *130*, 11592.
[73] C. W. Freudiger, W. Min, B. G. Saar, S. Lu, G. R. Holtom, C. He, J. C. Tsai, J. X. Kang, X. S. Xie, *Science* **2008**, *322*, 1857.
[74] S. W. Hell, *Opt. Lett.* **1994**, *19*, 780; T. A. Klar, S. W. Hell, *Opt. Lett.* **1999**, *24*, 954; T. A. Klar, S. Jakobs, M. Dyba, A. Egner, S. W. Hell, *Proc. Natl. Acad. Sci. USA* **2000**, *97*, 8206; S. W. Hell, *Science* **2007**, *316*, 1153.
[75] S. T. Hess, T. K. P. Giriajan, M. D. Mason, *Biophys. J.* **2006**, *91*, 4258; S. T. Hess, T. J. Gould, M. V. Gudheti, S. A. Maas, K. D. Mills, J. Wichmann, *Proc. Natl. Acad. Sci. USA* **2007**, *104*, 17370.
[76] M. J. Rust, M. Bates, X. Zhuang, *Nat. Methods* **2006**, *3*, 793; M. Bates, B. Huang, G. T. Dempsey, X. Zhuang, *Science* **2007**, *317*, 1749.
[77] P. Torok, T. Wilson, *Opt. Commun.* **1997**, *137*, 127; W. R. Zipfel, R. M. Williams, W. W. Webb, *Nat. Biotechnol.* **2003**, *21*, 1369.
[78] M. Nagorni, S. W. Hell, *J. Struct. Biol.* **1998**, *123*, 236; A. Egner, S. W. Hell, *Trends Cell Biol.* **2005**, *15*, 207.
[79] S. W. Hell, *Nat. Biotechnol.* **2003**, *21*, 1347.
[80] B. Huang, W. Wang, M. Bates, X. Zhuang, *Science* **2008**, *319*, 810.
[81] A. P. Hitchcock, J. J. Dynes, G. Johansson, J. Wang, G. Botton, *Micron* **2008**, *39*, 741.
[82] K. W. Jones, H. Feng, A. Lanzirotti, D. Mahajan, *Nucl. Instrum. Methods Phys. Res. Sect. B* **2005**, *241*, 331; K. W. Jones, H. Feng, A. Lanzirotti, D. Mahajan, *Top. Catal.* **2005**, *32*, 263.
[83] M. A. Le Gros, G. McDermott, C. A. Larabell, *Curr. Opin. Struct. Biol.* **2005**, *15*, 593; D. Y. Parkinson, G. McDermott, L. D. Etkin, M. A. Le Gros, C. A. Larabell, *J. Struct. Biol.* **2008**, *162*, 380; C. A. Larabell, M. A. Le Gros, *Mol. Biol. Cell* **2004**, *15*, 957; G. Mitrea, J. Thieme, P. Guttmann, S. Heim, S. Gleber, *J. Synchrotron Radiat.* **2008**, *15*, 26.
[84] K. V. Kaznatcheev, C. Karunankaran, U. D. Lanke, S. G. Urquhart, M. Obst, A. P. Hitchcock, *Nucl. Instrum. Methods Phys. Res. Sect. A* **2007**, *582*, 96; W. Chao, B. Harteneck, J. A. Liddle, E. H. Anderson, D. Attwood, *Nature* **2005**, *435*, 1210; H. C. Kang, H. Yan, R. P. Winarski, M. V. Holt, J. Maser, C. Liu, R. Conley, S. Vogt, A. T. Macrander, G. B. Stephenson, *Appl. Phys. Lett.* **2008**, *92*, 221114; T. Koyama, S. Ichimaru, T. Tsjuji, H. Takano, Y. Kagoshima, T. Ohchi, H. Takenaka, *Appl. Phys. Express* **2008**, *1*, 117003.
[85] The spatial resolution for hard X-rays (about 30 nm) is still less developed than for soft X-rays, as the latter also allow element-specific analysis. In the case of soft X-rays, current test zone plates can bring the spatial resolution down to 10 nm.
[86] P. Thibault, M. Direolf, A. Menzel, O. Bunk, C. David, F. Pfeiffer, *Science* **2008**, *321*, 379; H. N. Chapman, *Science* **2008**, *321*, 352.
[87] A. Brückner, *Catal. Rev. Sci. Eng.* **2003**, *45*, 97; S. J. Tinnemans, J. G. Mesu, K. Kervinen, T. Visser, T. A. Nijhuis, A. M. Beale, D. E. Keller, A. M. J. van der Eerden, B. M. Weckhuysen, *Catal. Today* **2006**, *113*, 3; A. Iglesias-Juez, A. M. Beale, M. G. O'Brien, M. A. Newton, W. Bras, B. M. Weckhuysen, *Synchrotron Radiat. News* **2009**, *22*, 22.
[88] I. J. Shannon, T. Maschmeyer, G. Sankar, J. M. Thomas, R. D. Oldroyd, M. Sheehy, D. Madill, A. M. Waller, R. P. Townsed, *Catal. Lett.* **1997**, *44*, 23; J. W. Couves, J. M. Thomas, D. Waller, R. H. Jones, A. J. Dent, G. E. Derbyshire, G. N. Greaves, *Nature* **1991**, *354*, 465; B. S. Clausen, L. Grabaek, G. Steffensen,

P. L. Hansen, H. Topsoe, *Catal. Lett.* **1993**, *20*, 23; J. D. Grunwaldt, A. M. Molenbroek, N. Y. Topsoe, H. Topsoe, B. S. Clausen, *J. Catal.* **2000**, *194*, 452.

[89] A. Brückner, *Chem. Commun.* **2001**, 2122; M. S. Kumar, M. Schwidder, W. Grünert, A. Brückner, *J. Catal.* **2004**, *227*, 384.

[90] T. A. Nijhuis, S. J. Tinnemans, T. Visser, B. M. Weckhuysen, *Phys. Chem. Chem. Phys.* **2003**, *5*, 4361; S. J. Tinnemans, M. H. F. Kox, T. A. Nijhuis, T. Visser, B. M. Weckhuysen, *Phys. Chem. Chem. Phys.* **2005**, *7*, 211; S. J. Tinnemans, M. H. F. Kox, M. W. Sietering, T. A. Nijhuis, T. Visser, B. M. Weckhuysen, *Phys. Chem. Chem. Phys.* **2006**, *8*, 2413.

[91] M. Hunger, W. Wang, *Chem. Commun.* **2004**, 584; W. Wang, Y. J. Jiang, M. Hunger, *Catal. Today* **2006**, *113*, 102; J. Jiang, J. Huang, V. R. Reddy, O. Y. Sang, M. Hunger, *Microporous Mesoporous Mater.* **2007**, *105*, 132; J. Huang, Y. J. Jiang, M. V. R. Reddy, O. Y. Sang, M. Hunger, *ChemPhysChem* **2008**, *9*, 1107.

[92] G. Le Bourdon, F. Adar, M. Moreau, S. Morel, J. Reffner, A. S. Mamede, C. Dujardin, E. Payen, *Phys. Chem. Chem. Phys.* **2003**, *5*, 4441.

[93] M. A. Newton, B. Jyoti, A. J. Dent, S. G. Fiddy, J. Evans, *Chem. Commun.* **2004**, 2382; M. A. Newton, A. J. Dent, S. G. Fiddy, B. Jyoti, J. Evans, *Catal. Today* **2007**, *126*, 64; M. A. Newton, C. Belver-Coldeira, A. Martinez-Arias, M. Fernandez-Garcia, *Nat. Mater.* **2007**, *6*, 528; A. J. Dent, J. Evans, S. G. Fiddy, B. Jyoti, M. A. Newton, M. Tromp, *Angew. Chem.* **2007**, *119*, 5452; *Angew. Chem. Int. Ed.* **2007**, *46*, 5356; J. Evans, A. Puig-Molina, M. Tromp, *MRS Bull.* **2007**, *32*, 1038; M. A. Newton, *Chem. Soc. Rev.* **2008**, *37*, 2644; A. J. Dent, J. Evans, S. G. Fiddy, B. Jyoti, M. A. Newton, M. Tromp, *Faraday Discuss.* **2008**, *138*, 287.

[94] T. Bürgi, *J. Catal.* **2005**, *229*, 55; T. Bürgi, A. Baiker, *Adv. Catal.* **2006**, *50*, 227.

[95] A. M. Beale, A. M. J. van der Eerden, K. Kervinen, M. A. Newton, B. M. Weckhuysen, *Chem. Commun.* **2005**, 3015.

[96] A. Brückner, *Chem. Commun.* **2005**, 1761; A. Brückner, E. Kondratenko, *Catal. Today* **2006**, *113*, 16; A. Brückner, *Adv. Catal.* **2007**, *51*, 265.

[97] A. M. Beale, A. M. J. van der Eerden, S. D. M. Jacques, O. Leynaud, M. G. O'Brien, F. Meneau, S. Nikitenko, W. Bras, B. M. Weckhuysen, *J. Am. Chem. Soc.* **2006**, *128*, 12386; S. Nikitenko, A. M. Beale, A. M. J. van der Eerden, S. D. M. Jacques, O. Leynaud, M. G. O'Brien, D. Detollenaere, R. Kapteijn, B. M. Weckhuysen, W. Bras, *J. Synchrotron Radiat.* **2008**, *15*, 632; M. G. O'Brien, A. M. Beale, S. D. M. Jacques, B. M. Weckhuysen, *Top. Catal.* **2009**, in press; M. G. O'Brien, A. M. Beale, S. D. M. Jacques, T. Buslaps, V. Honkimaki, B. M. Weckhuysen, *J. Phys. Chem. C* **2009**, *113*, 4890.

[98] J. G. Mesu, A. M. J. van der Eerden, F. M. F. de Groot, B. M. Weckhuysen, *J. Phys. Chem. B* **2005**, *109*, 4042; J. G. Mesu, A. M. Beale, F. M. F. de Groot, B. M. Weckhuysen, *J. Phys. Chem. B* **2006**, *110*, 17671.

[99] P. D. Majors, K. R. Minard, E. J. Ackerman, G. R. Holtom, D. F. Hopkins, C. I. Parkinson, T. J. Weber, R. A. Wind, *Rev. Sci. Instrum.* **2002**, *73*, 4329; R. A. Wind, K. R. Minard, G. R. Holtom, P. D. Majors, E. J. Ackerman, S. D. Colson, D. G. Cory, D. S. Daly, P. D. Ellis, N. F. Metting, C. I. Parkinson, J. M. Price, X. W. Tang, *J. Magn. Reson.* **2000**, *147*, 371.

[100] A. Sartori, R. Gatz, F. Beck, A. Rigort, W. Baumeister, J. M. Plitzko, *J. Struct. Biol.* **2007**, *160*, 135; H. Schwarz, B. Humbel in *Electron Microscopy: Methods and Protocols* (Ed.: J. Kuo), Humana Press, Totowa, **2007**, p. 229; T. Takizawa, J. M. Robinson, *Methods Mol. Med.* **2006**, *121*, 351.

[101] Y. Tian, D. Chassaing, A. G. Nasibulin, P. Ayala, H. Jiang, A. S. Anisimov, E. I. Kauppinen, *J. Am. Chem. Soc.* **2008**, *130*, 7188.

[102] A. V. Agronskaia, J. A. Valentijn, L. F. van Driel, C. T. W. M. Schneijdenberg, B. M. Humbel, P. M. P. van Bergen en Henegouwen, A. J. Verkleij, A. J. Koster, H. C. Gerritsen, *J. Struct. Biol.* **2008**, *164*, 183.

[103] D. J. Müller, Y. F. Dufrene, *Nat. Nanotechnol.* **2008**, *3*, 261.

[104] For example: G. Kaupp, *Atomic Force Microscopy, Scanning Near-Field Optical Microscopy and Nanoscratching*, Springer, Berlin, **2006**; *Handbook of Microscopy for Nanotechology* (Eds.: N. Yao, Z. L. Wang), Kluwer Academic Publishers, Boston, **2005**. The first idea to overcome the diffraction limit of optical microscopy was introduced by Synge in 1928 and is commonly known as the optical near-field concept. Optical near field is defined as the region of space less than one wavelength away from the light source, in which diffraction does not occur. In this case, the resolution is only a function of the size and the distance between the light source and the sample. This idea to fabricate a light source much smaller than the wavelength of light and to bring it very close to the object only became reality in 1984 with the introduction of the first near-field optical microscope.

[105] For example: M. L. Occelli, S. A. C. Gould, G. D. Stucky, *Stud. Surf. Sci. Catal.* **1994**, *84*, 485; M. L. Occelli, J. P. Olivier, A. Auroux, *J. Catal.* **2002**, *209*, 385; S. Sugiyama, S. Yamamoto, O. Matsuoka, T. Honda, H. Nozoye, S. Qiu, J. Yu, O. Terasaki, *Surf. Sci.* **1997**, *377–379*, 140; M. W. Anderson, T. Ohsuna, Y. Sakamoto, Z. Liu, A. Carlsson, O. Terasaki, *Chem. Commun.* **2004**, 907; L. I. Meza, M. W. Anderson, J. R. Agger, C. S. Cundy, C. B. Chong, R. J. Blaisted, *J. Am. Chem. Soc.* **2007**, *129*, 15192; R. Brent, M. W. Anderson, *Angew. Chem.* **2008**, *120*, 5407; *Angew. Chem. Int. Ed.* **2008**, *47*, 5327.

[106] C. Fokas, V. Deckert, *Appl. Spectrosc.* **2002**, *56*, 192.

[107] B. Pettinger, G. Picardi, R. Schuster, G. Ertl, *J. Electroanal. Chem.* **2003**, *554–555*, 293; B. Pettinger, G. Picardi, R. Schuster, G. Ertl, *Single Mol.* **2002**, *3*, 285; A. Hartschuh, *Angew. Chem.* **2008**, *120*, 8298; *Angew. Chem. Int. Ed.* **2008**, *47*, 8178; B. Pettinger, B. Ren, G. Picardi, R. Schuster, G. Ertl, *Phys. Rev. Lett.* **2004**, *92*, 096101; T. Kodama, T. Umezawa, S. Watanabe, H. Ohtani, *J. Microsc.* **2008**, *229*, 240.

[108] J. S. Samson, G. Wollny, E. Burndermann, A. Bergner, A. Hecker, G. Schwaab, A. D. Wieck, M. Havenith, *Phys. Chem. Chem. Phys.* **2006**, *8*, 753; M. M. Qazilbash, M. Brehm, B. G. Chae, P. C. Ho, G. O. Andreev, B. J. Kim, S. J. Yun, A. V. Balatsky, M. B. Maple, F. Keilmann, H. T. Kim, D. N. Basov, *Science* **2007**, *318*, 1750; K. Mueller, X. Yang, M. Paulite, Z. Fakhraai, N. Gunari, G. C. Walker, *Langmuir* **2008**, *24*, 6946; A. J. Huber, A. Ziegler, T. Köck, R. Hillenbrand, *Nat. Nanotechnol.* **2009**, *4*, 153.

[109] A. J. Huber, F. Keilmann, J. Wittborn, J. Aizpurua, R. Hillenbrand, *Nano Lett.* **2008**, *8*, 3766; P. Planken, *Nature* **2008**, *456*, 454.

[110] I. I. Smolyaninov, C. C. Davis, *ChemPhysChem* **2009**, *10*, 625.

[111] C. L. Degen, M. Poggio, H. J. Mamin, C. T. Rettner, D. Rugar, *Proc. Nat. Acad. Sci.* **2009**, *106*, 1313; P. C. Hammel, *Nature*, **2009**, *458*, 844.